Alignment and Orientation of Complex Molecules

Dissertation

zur Erlangung des Doktorgrades an der Fakultät für
Mathematik, Informatik und Naturwissenschaften
Fachbereich Physik
der Universität Hamburg

vorgelegt von

Linda Vanessa Thesing

Hamburg
2019

Gutachter/innen der Dissertation: Prof. Dr. Jochen Küpper
Dr. habil. Rosario González-Férez

Zusammensetzung der Prüfungskommission: Prof. Dr. Jochen Küpper
Dr. habil. Rosario González-Férez
Prof. Dr. Peter Schmelcher
Prof. Dr. Markus Drescher
Prof. Dr. Daniela Pfannkuche

Datum der Disputation: 21.02.2020

Vorsitzende der Prüfungskommission: Prof. Dr. Daniela Pfannkuche

Vorsitzender Fach-Promotionsausschusses PHYSIK: Prof. Dr. Günter Hans Walter Sigl

Leiter des Fachbereichs PHYSIK: Prof. Dr. Wolfgang Hansen

Dekan der Fakultät MIN: Prof. Dr. Heinrich Graener

Eidesstattliche Versicherung

Hiermit versichere ich an Eides statt, die vorliegende Dissertationsschrift selbst verfasst und keine anderen als die angegebenen Hilfsmittel und Quellen benutzt zu haben. Die eingereichte schriftliche Fassung entspricht der auf dem elektronischen Speichermedium. Die Dissertation wurde in der vorgelegten oder einer ähnlichen Form nicht schon einmal in einem früheren Promotionsverfahren angenommen oder als ungenügend beurteilt.

Hamburg, den 20.03.2020

Linda Vanessa Thesing

Zusammenfassung

Moleküle mit Hilfe von externen elektrischen Feldern auszurichten und zu orientieren, ist von großem Interesse in der physikalischen Chemie. Zu den grundlegenden Anwendungen zählen verschiedene experimentelle Abbildungstechniken, die mit dem Ziel eingesetzt werden, zeitabhängige Strukturen isolierter Moleküle in dynamischen Prozessen zu bestimmen. Kontrolle über die Rotation der Moleküle mindert hierbei den Informationsverlust durch die Mittelung über zufällige Orientierungen und erlaubt es, Information direkt im Molekülsystem zu erhalten. Eine genaue theoretische Beschreibung der Rotationsdynamik in elektrischen Feldern ist äußerst wichtig für die Analyse der Experimente und um starke Ausrichtung und Orientierung zu erreichen. Viele bisherige Studien verwendeten die starre Rotor Näherung und vernachlässigten Schwingungsfreiheitsgrade und Kernspinwechselwirkungen oder waren auf Systeme hoher Symmetrie beschränkt. Aufgrund der Komplexität vieler Biomoleküle ist eine verallgemeinerte Beschreibung, die interne Rotationen und deren Kopplung zu der Gesamtrotation sowie Kernspineffekte einbezieht, erforderlich. In dieser Arbeit werden Schritte zu einer derartigen allgemeinen Beschreibung der Rotationsdynamik komplexer Moleküle hin vorgestellt.

Zunächst wird eine zeitabhängige Analyse der Orientierung durch Laserfelder in Kombination mit statischen elektrischen Feldern präsentiert. Hierfür wird das Molekül 6-chloropyridazine-3-carbonitrile verwendet, bei dem das elektrische Dipolmoment zu keiner der Hauptträgheitsachsen parallel ist. Das im Experiment beobachtete Orientierungsverhalten wird reproduziert und es wird gezeigt, dass es von einer hochgradig nicht-adiabatischen Dynamik verursacht wird, was in der vorherigen Beschreibung nicht erfasst wurde. Als Nächstes wird der Einfluss der internen Rotation des Wassermoleküls in Indol(H_2O)-Komplexen analysiert. Hier wird gezeigt, dass die Kopplung der internen und der gesamte Rotation unter normalen experimentellen Bedingungen für Orientierung mit kombinierten elektrischen Feldern vernachlässigt werden kann und dass die Indol(H_2O)-Komplexe wie starre Moleküle behandelt werden können. Die nachfolgenden Studien befassen sich mit der Auswirkung von Kernquadrupolwechselwirkungen auf die laserinduzierte Ausrichtung von Molekülen. Zunächst wird unsere theoretische Vorgehensweise vorgestellt, welche es prinzipiell zulässt, eine beliebige Anzahl von Kernspins einzubeziehen. Die Anwendung von diesem Ansatz wird anhand des Moleküls CFClBrI, das mehrere schwere Kerne mit großen Quadrupolmomenten hat, demonstriert. Hierbei wurde eine deutliche Auswirkung der Quadrupolkopplung auf die feldfreie Ausrichtung, induziert durch kurze Laserpulse, beobachtet. Im Anschluss wird er Einfluss der Laserpulsdauer und der Eigenschaften verschiedener linearer und asymmetrischer Moleküle untersucht. Adiabatische Ausrichtung wird von der Kernquadrupolkopplung nicht beeinflusst, aber es wird ein deutlicher Einfluss auf die feldfreie Dynamik nach Wechselwirkung mit verschiedenen Laserfeldern beobachtet. Dieser Effekt kann auf eine Dephasierung der Wellenpakete durch die Hyperfeinenergieaufspaltungen der Rotationsniveaus zurückgeführt werden. Diese Dephasierung ist allgemein am größten für Rotationszustände niedriger Energie und der Einfluss der Quadrupolkopplung ist am geringsten für starke Laserfelder durch die hoch angeregte Rotationszustände besetzt werden. Des Weiteren

ist die Größe der Hyperfeinenergieaufspaltungen im Vergleich zu den Energieabständen der Rotationsniveaus von großer Bedeutung für den Einfluss auf die Rotationsdynamik.

Abstract

Aligning and orienting molecules with external electric fields has long been of great interest in physical chemistry. Among the principle applications are various single molecule imaging techniques employed with the goal to determine transient molecular structures during dynamical processes. Here, rotational control mitigates the loss of information from averaging over random orientations of molecules and allows one to obtain information directly in a molecular frame. An accurate theoretical description of the field-dressed rotational dynamics is crucial for the analysis of the experiments as well as guiding them to achieve optimal degrees of alignment and orientation. Many previous studies relied on the rigid-rotor approximation and neglected large amplitude vibrations and nuclear spin interactions or focused on highly symmetric systems. Since most biomolecules are very complex, a generalized description including internal motions and their coupling to the rotations as well as nuclear spin effects is needed. This thesis takes steps towards such a generalized description of the rotational dynamics of complex molecules.

First, a time-dependent analysis of the mixed-field orientation of a rigid molecule without rotational symmetry, i. e., 6-chloropyridazine-3-carbonitrile, which has an electric dipole moment not parallel to any principle axis of inertia, is presented. The experimentally observed behavior of the orientation of this molecule is reproduced and shown to originate from a highly non-adiabatic dynamics, which was not captured by the previous adiabatic description. Next, the impact of the internal rotation of the water molecule in indole(H_2O) clusters is analyzed. It is shown that the coupling of the internal and overall rotations can be neglected under typical conditions in mixed-field orientation experiments, and the clusters effectively behave like rigid-rotor molecules. The following studies focus on the impact of nuclear-quadrupole interactions on the laser alignment of molecules. First, our theoretical approach, which allows, in principle, to include an arbitrary number of nuclear spins, is presented. Its application is demonstrated using the molecule CFClBrI, which has several heavy nuclei with large quadrupole moments. A significant impact of the quadrupole coupling on the impulsive alignment of this molecule was observed. Then, the influence of the laser pulse shape and chemical properties of different linear and asymmetric top molecules is studied. While adiabatic alignment is not affected by nuclear-quadrupole interactions, a significant impact on the post-pulse dynamics following short or truncated laser pulses is observed. This effect can be attributed to a dephasing of the wave packets caused by the hyperfine energy shifts of the rotational levels. This dephasing is generally the largest for low-lying rotational states and the impact of the quadrupole coupling is minimized for strong laser fields populating highly excited rotational states. Furthermore, the magnitude of the hyperfine energy shifts in relation to rotational energy gaps plays a crucial for the extent to which the rotational dynamics is modified.

Contents

1 Introduction

1.1. Motivation

Understanding and controlling nature at the level of molecules and atoms down to elementary particles is an important endeavor of contemporary physical sciences. For instance, the analysis of molecular structures plays a crucial role in studies of chemical reactions which are of high interest due to their importance in biological function, medicine, industrial processes, astrochemistry and so on. In these dynamical processes, determining intermediate configurations of molecules is necessary to understand different pathways of the reactions. This requires a spatial resolution on the order of picometers and a temporal resolution on the order of femtoseconds to follow the motions of the nuclei. Sufficient spatio-temporal resolution can be achieved by experimental techniques including photoelectron imaging [1–7], high-harmonic generation [8–10], electron diffraction [11–13] and x-ray diffraction. For the latter method, x-ray free electron lasers such as the LINAC Coherent Light Source (LCLS) in the United States and the European XFEL are particularly useful as they supply intense ultrashort x-ray pulses [14]. Most experiments are performed in a pump-probe fashion. A pump pulse induces the dynamics in a single molecule and diffracted x-ray probe photons generate a pattern that reveals the structure of the molecule [14–17]. To gain high contrast, it is necessary to collect diffraction patterns from thousands of identical molecules as each individual molecule is destroyed by the x-ray pulse [18]. The prime goal is to record molecular movies of chemical reactions with high spatio-temporal resolution by measuring diffraction patterns for different delays between the pump and the x-ray probe pulses [14, 19].

To build clear diffraction patterns, single molecule diffraction experiments rely on the imaging of a large number of identical molecules [20]. Averaging over random orientations of molecules in the gas phase, however, leads to a blurring of the diffraction images. Alignment and orientation of molecules in space, i. e., angular confinement and preferred directions of molecular axes, prevent this loss of information and are therefore crucial in the quest for the recording of molecular movies. For example, laser alignment of 2,5-diiodobenzonitrile molecules enabled accurate measurement of the iodine-iodine internuclear distance in an x-ray diffraction experiment at the LCLS [17]. In another experiment, the suppression of electron emission in the molecular plane was only observed for oriented benzonitrile molecules [4]. The relative orientations of molecules often have direct influence on the rates of chemical reactions as, for example, it was observed in the reactions K + CH_3I [21] and Rb + CH_3I [22–24]. Oriented samples of molecules can enable such observations of steric effects [21–25] and aid in their control [26, 27].

1.2. Rotational control of molecules by external electric fields

Many experimental and theoretical efforts have been undertaken to align and orient molecules using external electric fields. For instance, electrostatic hexapole fields can be used to prepare molecules in single rotational states [21, 28–30]. Due to their quantum nature, the spatial anisotropy of these states is, however, not very large. Another method utilizes strong static electric fields to induce "brute-force" orientation of the molecules [31–33]. To achieve strong degrees of orientation (and alignment), this technique relies on rotationally cold molecules with large permanent electric-dipole moments and its applicability is thus limited. A more general way to align molecules was proposed by Friedrich and Herschbach [34–36] as well as Seideman [37]. It makes use of strong nonresonant laser fields to confine the most polarizable axis (MPA) along the polarization axis of the optical field [38–40]. This method also entails the possibility of 3D alignment, e. g., by using elliptically polarized fields [41–46]. Depending on the duration and shape of the laser field, the temporal behavior of the alignment can be controlled in a variety of ways [47, 48]. Laser pulses with durations much larger than the molecule's rotational period adiabatically transfer the initial quantum state to an aligned pendular state [35]. In combination with weak static fields, the molecules can additionally be strongly oriented [49–51]. This so-called mixed-field orientation was demonstrated experimentally [52–55], however, the adiabatic picture employed in the theoretical calculations proved to be insufficient to reproduce the observed degrees of orientation [54]. Instead, a time-dependent description of the field-dressed dynamics is required [56, 57].

While adiabatic alignment allows one to obtain strong degrees of spatial confinement, its drawback is that the alignment is only maintained as long as the laser field is present. In chemical reaction studies, external electric fields can cause unwanted perturbations and laser field-free alignment is necessary. This can be achieved by the creation of field-free rotational wave packets, e. g., by subjecting molecules to one or more laser pulses with durations much shorter than their rotational periods [37]. For linear and symmetric top molecules, these wave packets rephase periodically and exhibit revivals of the initial alignment during or shortly after the pulse [47, 58–61]. In this impulsive regime, unprecedented degrees of field-free alignment were, for instance, obtained for carbonyl sulfide (OCS) molecules using an optimized two-pulse sequence [62]. Asymmetric top molecules show more complex revival patterns due to their rich energy level structures and the peak alignment decreases over time [63–65]. Here, the ability to produce shaped laser pulses has opened the door to further improve field-free alignment techniques, e. g., by using truncated laser fields [42, 66–69]. The long rising and short falling edges of these pulses combine the "best of both worlds" of adiabatic and impulsive alignment. All of the methods described here benefit from rotationally cold samples of molecules since excited rotational states typically show smaller degrees of alignment and orientation. In addition, deflection of molecular beams allows for the spatial separation of low-lying rotational states [70, 71] further improving the alignment [72].

1.3. Molecules are complex

To accurately describe the rotational dynamics of different molecules, it is essential to include all additional degrees of freedom that couple to rotations in a significant way. A full description encompasses all electronic, vibrational and nuclear spin degrees of freedom in addition to the rotations. However, such an extensive treatment of the molecular dynamics is generally not required for isolated, rotationally cold molecules in the gas phase. For the applications in this thesis, the electronic and nuclear degrees of freedom can be decoupled within the Born-Oppenheimer approximation. In a similar manner, vibrational and rotational motion can often be separated in the framework of the rigid-rotor approximation. This approximation is, however, in general not applicable for molecules showing large amplitude vibrations, e. g., internal rotations. Since many molecules are floppy [73–80], it is of high importance to understand how internal motions and overall rotations interact to accurately predict their coupled dynamics [81–85].

Nuclear spin interactions cause the splitting of rovibrational energy levels into different hyperfine components. Such energy shifts are, for instance, produced by nuclear quadrupole couplings in molecules substituted with heavy elements like iodine and bromine. These heavy nuclei are frequently utilized to increase the diffraction signal in imaging experiments [11, 17]. The coupling of the rotational and nuclear spin angular momenta can cause a depolarization of molecules prepared in single rotational states [86–94]. Additionally, a significant influence of hyperfine interactions on the revival patterns of field-free aligned molecules was recently observed [95]. Knowledge of the nuclear spin states of molecules is furthermore needed to determine spin statistical weights of rovibrational levels.

In biological processes, the local environment of a molecule strongly impacts its function [96]. Understanding solvent-solute interactions is thus highly relevant for the investigation of the chemical dynamics of (bio)molecules. Solvent effects have, for instance, been shown for indole, the chromphore of the amino acid tryptophan [97, 98]. Studying dynamics in, e. g., aqueous solutions adds more complexity to the experimental process. To bridge the gap between isolated and solvated molecules, molecular solvent-solute clusters are of high interest [99–101] as they can be brought into the gas phase and subjected to single molecule imaging techniques [102–104]. They also serve as good candidates for the study of hydrogen bonded systems, which are ubiquitous in biochemistry. These clusters are generally floppy and display large amplitude internal motions that are coupled to the rotational dynamics of the cluster.

1.4. Outline of this thesis

This thesis is organized as follows. In chapter 2, the fundamental concepts and numerical methods used throughout this work are summarized. In chapter 3, a time-dependent analysis of the mixed-field orientation of a molecule without rotational symmetry is presented. Chapter 4 focuses on the influence of the internal rotation of the water moiety in indole(H_2O) clusters on its mixed-field-orientation dynamics. In the following three chapters, the influence of nuclear-quadrupole interactions on the laser alignment of linear and asymmetric top molecules is investigated. First, the theoretical model used to describe these interactions is presented in chapter 5. Its application is demonstrated using the molecule CFClBrI, for which the effect of the quadrupole coupling is studied in the impulsive alignment regime. In chapter 6, the impact of the nuclear-quadrupole coupling is systematically analyzed for different laser intensities and pulse shapes including long and short pulse durations as well as truncated laser fields. Here, the linear molecule I_2 and the asymmetric top molecule 1,4-diiodobenzene are used as prototypical examples. Chapter 7 is focused on the quadrupole interactions in molecules with different chemical properties such as their rotational constants, polarizability and electric field gradient tensors and number of nuclei with large quadrupole moments. The post-pulse rotational dynamics, induced by short laser pulses, is analyzed for the molecules iodobenzene, 2,5-diiodobenzonitrile, 1,3-diiodobenzene and 1,2-diiodobenzene. Finally, in chapter 8, the results are summarized and an outlook for future studies is given.

2 Fundamental concepts

This chapter provides a brief overview over the theoretical and numerical methods used throughout this thesis. It provides the equations and concepts that are needed to calculate the rotational dynamics of complex molecules in external electric fields. These are implemented in a software package, described in section 2.6, to the development of which I contributed as a part of my thesis project. For more details on the concepts illustrated here, I recommend the textbooks [105–108].

2.1. Molecular symmetries

A transformation that leaves the Hamiltonian of a system invariant is called a symmetry operation of this system. In the case of molecules in free space, such symmetry operations include permutations of electrons and identical nuclei, spatial inversion, translations along space-fixed directions and rotations about space-fixed axes. The eigenfunctions of the molecular Hamiltonian can be classified according to the irreducible representations of groups formed by these symmetry operations. A particularly useful group for the symmetry classification of internal molecular wave functions is the so called molecular symmetry (MS) group, which consists of all feasible nuclear permutation and inversion operations that commute with the Hamiltonian [107]. Each element $\hat{O}$ of the MS group can be written as

$$\hat{O} = \hat{O}_{vibronic}\hat{O}_{rot}\hat{O}_{ns}, \tag{2.1}$$

where $\hat{O}_{vibronic}$, $\hat{O}_{rot}$ and $\hat{O}_{ns}$ act on the vibrational and electronic (vibronic), rotational and nuclear spin coordinates, respectively. Vibronic, rotational and nuclear spin states of the molecule can thus be classified separately in the MS group. When only the rotational states of asymmetric top molecules are of interest, it is useful to label them according to the irreducible representations of the rotation group D_2 (*four-group*) [106, 107]. Its elements are the identity E and the two-fold rotations R_{2a}, R_{2b}, R_{2c} about the molecule's principle axes of inertia a, b, c ($\hat{O}_{rot}$ in Equation 2.1). The character table of the D_2 group [107] is shown in Table 2.1. For a more detailed discussion of the MS groups and their relation to rotation and point groups of molecules, the reader is referred to [107].

	E	R_{2a}	R_{2b}	R_{2c}
A	1	1	1	1
B_a	1	1	-1	-1
B_b	1	-1	1	-1
B_c	1	-1	-1	1

Table 2.1.: Character table of the D_2 rotation group.

Molecular symmetries have important advantages for the applications in this thesis. Wave functions of different symmetries are not coupled by the molecular Hamiltonian. By choosing symmetry adapted basis sets, matrix representations of the Hamiltonian can thus be factorized into different blocks corresponding to each symmetry species, which reduces the computational cost in numerical calculations. Symmetry considerations also aid in determining which levels are connected by external perturbations such as electric fields and thus allows one to distinguish real and avoided crossings. Furthermore, the symmetries of the nuclear spin wave functions are important for determining nuclear spin statistical weights [107].

2.2. Rotational energy levels of molecules

In this work, the rotational energy levels and eigenstates of molecules are calculated within the Born-Oppenheimer approximation. While the structure of the molecules is in general not rigid, effects related to the nonrigidity are not considered here, with the exception of internal rotations which are treated in section 2.3 and chapter 4. Using the rigid-rotor approximation, the rotational Hamiltonian of a molecule is given by

$$H_{\text{rot}} = A\hat{J}_a^2 + B\hat{J}_b^2 + C\hat{J}_c^2, \tag{2.2}$$

where $\hat{J}_i$ are the components of the rotational angular momentum $\hat{\boldsymbol{J}}$ in the molecule-fixed frame (MFF) (abc) defined by the principle axes of inertia. Here,

$$A = \frac{\hbar^2}{2I_a},\ B = \frac{\hbar^2}{2I_b},\ C = \frac{\hbar^2}{2I_c} \tag{2.3}$$

are the rotational constants and $I_a \leq I_b \leq I_c$ are the moments of inertia with respect to the a, b and c axis.

2.2.1. Linear molecules

Linear molecules are characterized by only one rotational constant B_0 and the rotational Hamiltonian reduces to

$$H_{\text{rot}} = B_0\hat{\boldsymbol{J}}^2. \tag{2.4}$$

The eigenfunctions of this Hamiltonian are spherical harmonics $Y_{JM}(\theta, \phi)$, where $M = -J, ..., J$ is the eigenvalue (in units of $\hbar$) of the projection $\hat{J}_Z$ of the angular momentum onto the laboratory-fixed Z axis. The energy levels of the linear rotor are given by $E_J = B_0J(J+1)$, $J = 0, 1, ...$, and are $(2J+1)$-fold degenerate in M.

2.2.2. Symmetric top molecules

For a symmetric top molecule, two of the rotational constants are equal, i. e., $A = B > C$ (oblate symmetric top) or $A > B = C$ (prolate symmetric top). The eigenfunctions of the rigid-rotor Hamiltonian (2.2) can be expressed in terms of Wigner matrices [105]

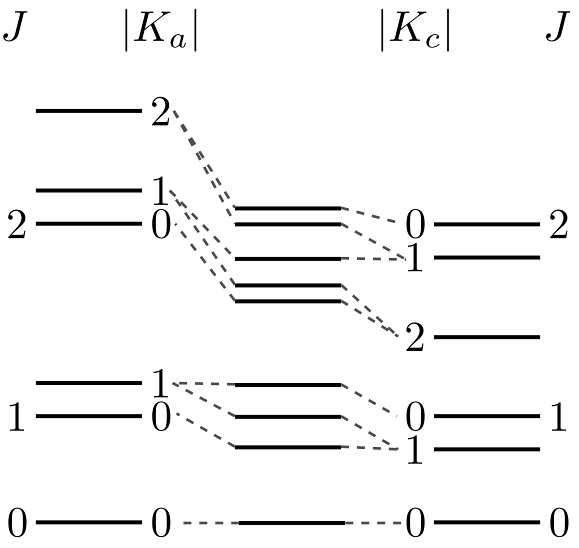

Figure 2.1.: Schematic energy level structure of an asymmetric top molecule (center). Each energy level can be linked to an energy level in the prolate (left) and oblate (right) symmetric top limit giving rise to the labeling using the quantum numbers K_a and K_c.

$D^J_{MK}(\phi, \theta, \chi)$ as

$$\langle \Omega | JKM \rangle = \sqrt{\frac{2J+1}{8\pi^2}} D^J_{MK}\left(\phi, \theta, \chi\right)^*, \tag{2.5}$$

where $\Omega = (\phi, \theta, \chi)$ are the Euler angles [105]. Analogous to M, $K = -J, ..., J$ is the eigenvalue of the projection of the angular momentum onto the molecule-fixed z axis. For an oblate and prolate top, the z axis is defined by the c and a axis, respectively. The energy levels of the oblate top are $E_{JK} = AJ(J+1) + (C-A)K^2$ and for the prolate top they are $E_{JK} = CJ(J+1) + (A-C)K^2$. Each level is doubly degenerate for $|K| > 0$ and $(2J+1)$-fold degenerate in M.

2.2.3. Asymmetric top molecules

For an asymmetric top molecule ($A \neq B \neq C$), J and M are good quantum numbers while K is not. The eigenfunctions of the Hamiltonian (2.2) can be written as linear combinations of symmetric-top functions

$$|J\omega M\rangle = \sum_K C_{\omega K} \, |JKM\rangle \, , \tag{2.6}$$

where ω labels different states with the same value of J. To determine the coefficients $C_{\omega K}$, it is advantageous to apply the Wang transformation [109]. It yields a matrix representation of the Hamiltonian in a block-diagonal form, where each block corresponds to a different symmetry species of the D_2 group [105, 106]. The associated time-independent Schrödinger equation (TISE) can then be solved by diagonalizing each of the resulting submatrices separately. In addition to J, the energy levels can be labeled by the quantum

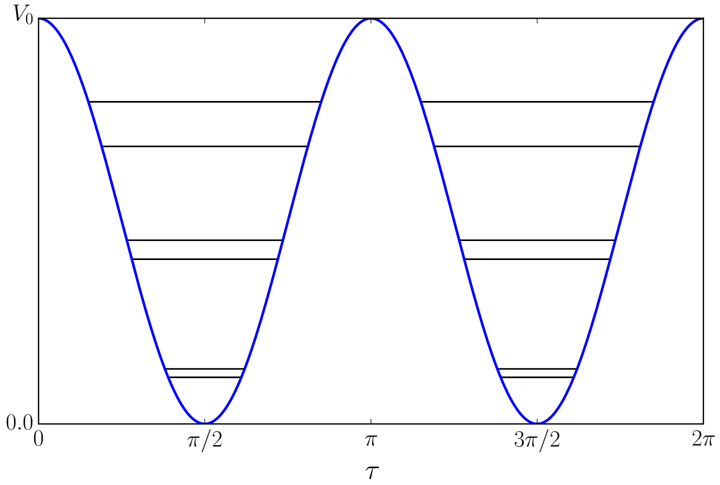

Figure 2.2.: Example for a torsional potential with a two-fold barrier. The depicted potential has a cosine shape with minima at $\tau = \pi/2$ and $\tau = 3\pi/2$ and a barrier height of V_0. The three lowest torsional energy levels are schematically shown. For a two-fold barrier ($N = 2$), each level splits into two nondegenerate sublevels.

numbers K_a and K_c, which correspond to the absolute value of the quantum number K in the limit of a prolate and oblate symmetric top, respectively, see Figure 2.1. The K_a and K_c quantum numbers contain useful information about the symmetry of a given rotational state, i. e., if K_a and K_c are both even (ee) the state is of A symmetry, for K_a and K_c both odd (oo) it is of B_b symmetry and for the cases eo and oe it belongs to the B_a and B_c species, respectively.

2.3. Internal rotations

The rigid-rotor Hamiltonian (2.2) is not sufficient to describe the rotational behavior of nonrigid molecules. A molecule is considered nonrigid if it has two or more potential energy minima in a given electronic state that are separated by permeable barriers so that tunneling between the different conformers can be observed. Examples for such large amplitude motions are internal rotations, which are found in a variety of molecules [73–80]. To describe the coupled internal and overall rotations, we use an angle τ for the internal torsion and the three Euler angles (ϕ, θ, χ) describing the overall rotation. The coupled rotation-torsional Hamiltonian reads

$$
\begin{aligned}
H_{\text{rot-tor}} =& \frac{1}{2} \sum_{\alpha,\beta=x,y,z} \hat{J}_\alpha G^{\text{rot}}_{\alpha\beta}(\tau) \hat{J}_\beta && (2.7\text{a}) \\
&+ \frac{1}{2} p_\tau G^{\text{tor}}_{\tau}(\tau) p_\tau + V(\tau) && (2.7\text{b}) \\
&+ \frac{1}{2} \sum_{\alpha=x,y,z} \left[p_\tau G^{\text{cor}}_{\tau\alpha}(\tau) \hat{J}_\alpha + \hat{J}_\alpha G^{\text{cor}}_{\alpha\tau}(\tau) p_\tau \right] . && (2.7\text{c})
\end{aligned}
$$

The first term (2.7a) is the rotational Hamiltonian where $\hat{J}_\alpha$ are the components of the overall angular momentum in the molecule-fixed frame and $G^{\text{rot}}_{\alpha\beta}(\tau)$ is the kinetic-energy matrix associated with the overall rotation. If the principle axes of inertia are independent of the torsion and are chosen as the molecule-fixed frame, the term (2.7a) reduces to Equation 2.2 with rotational constants that depend on the torsional angle τ. In the second term (2.7b), $G^{\text{tor}}_{\tau}(\tau)$ is the kinetic-energy matrix of the torsional motion, $p_\tau = -i\hbar\partial/\partial\tau$ is the momentum operator of the torsion and $V(\tau)$ is the torsional potential. The last term (2.7c) describes the coupling of the internal and overall rotations. The torsional energy-level structure, i. e., the eigenvalues of the purely torsional part of the Hamiltonian (2.7b), depends on the symmetry of the molecule and the barrier height between the equivalent configurations. For an N-fold finite barrier, tunneling leads to a splitting of each torsional level into $(N+2)/2$ ($(N+1)/2$) distinct sublevels for N even (odd), $(N-2)/2$ ($(N-1)/2$) of which are doubly degenerate [73]. An example of a two-fold torsional potential and corresponding energy levels is depicted in Figure 2.2. The rotation-torsional energy levels are obtained by solving the TISE for the full Hamiltonian (2.7). If the coupling of the internal and overall rotations is small, these energy levels are approximately given by the sum of pure rotational and torsional energies. The Hamiltonian in the form (2.7) can also be used to describe other types of large amplitude vibrations by replacing the angle τ with a coordinate parametrizing the vibrational mode under consideration [110].

2.4. Nuclear-quadrupole coupling

The interactions of the magnetic-dipole moments and electric-quadrupole moments of individual nuclei with the internal magnetic fields and electric-field gradients at their instantaneous positions give rise to the splitting of the rotational levels into several hyperfine components [106, 107]. The hyperfine energy shifts due to magnetic-dipole interactions are typically several orders of magnitude smaller than rotational energy gaps. This thesis is focused on the much stronger electric-quadrupole interactions. Quadrupole interactions are present if both the nuclear charge distribution and the electronic charge distribution about the nucleus are nonspherical. Nuclei with spins 0 or 1/2 are spherically symmetric and thus have zero quadrupole moments.

The Hamiltonian, describing the rotational motion and nuclear-quadrupole coupling of N nuclei, is given by [106]

$$H_{\text{rot-qc}} = H_{\text{rot}} + \sum_{l=1}^{N} \boldsymbol{V}(l) \cdot \boldsymbol{Q}(l). \tag{2.8}$$

Here, H_{rot} is the rigid-rotor Hamiltonian, see section 2.2, $\boldsymbol{V}(l)$ is the electric-field-gradient tensor and $\boldsymbol{Q}(l)$ is the nuclear-quadrupole-moment tensor. Using coupled basis states, the matrix elements of the Hamiltonian can be calculated analytically for different coupling schemes of the nuclear spins and rotational angular momentum [111]. The hyperfine energy levels are obtained by solving the TISE associated with the Hamiltonian (2.8).

In the equal or nearly equal coupling representation, they are characterized by the quantum number F of the total angular momentum $\hat{\boldsymbol{F}} = \hat{\boldsymbol{J}} + \hat{\boldsymbol{I}}$, $\hat{\boldsymbol{I}}$ being the total spin, as well as rotational and nuclear-spin quantum numbers (if $N > 1$). For some molecules, hyperfine shifts can be as large as rotational energy gaps, in particular for molecules with heavy nuclei and small rotational constants such as 1,4-diiodobenzene. Strong hyperfine couplings can have a significant effect on laser-induced field-free alignment [95], which is sensitive even to small energy shifts of rotational states.

2.5. Molecules in external electric fields

The interaction potential of an external electric field $\vec{\boldsymbol{E}}$ with the molecule's permanent electric-dipole moment $\vec{\boldsymbol{\mu}}$ and polarizability tensor $\underline{\underline{\alpha}}$ is given by [106]

$$H_{\text{int}}(t) = -\vec{\boldsymbol{\mu}} \cdot \vec{\boldsymbol{E}}(t) - \frac{1}{2}\vec{\boldsymbol{E}}(t)\underline{\underline{\alpha}}\vec{\boldsymbol{E}}(t). \tag{2.9}$$

Higher order terms such as the interaction of the electric field with the hyperpolarizability of the molecule, have been neglected. In this thesis, only the interactions with static electric fields $\vec{\boldsymbol{E}}_{\text{stat}}$ and nonresonant laser fields of the form $\vec{\boldsymbol{E}}_{\text{las}}(t)\cos(\omega t)$ are taken into account. Equation 2.9 then reduces to

$$H_{\text{int}}(t) = -\vec{\boldsymbol{\mu}} \cdot \vec{\boldsymbol{E}}_{\text{stat}} - \frac{1}{4}\vec{\boldsymbol{E}}_{\text{las}}(t)\underline{\underline{\alpha}}\vec{\boldsymbol{E}}_{\text{las}}(t). \tag{2.10}$$

Here, we consider field strengths E_{stat} of the static field that are small enough so that its interaction with the static polarizability tensor can be neglected. Additionally, $2\pi/\omega$ is assumed to be much shorter than the pulse duration and rotational periods and average over the rapid oscillations of the laser electric field. The interaction of this field with the permanent electric-dipole moment then vanishes. For certain field configurations, e. g., linearly polarized laser fields with parallel static fields, the interaction Hamiltonian (2.10) can be simplified further, as shown in the following chapters. The symmetry operations, which commute with the Hamiltonian, depend on the field configuration and molecule. The relevant cases are illustrated in following chapters as well.

2.6. Numerical methods

We study the rotational dynamics of molecules in external electric fields. To this end, we numerically solve the time-dependent Schrödinger equation (TDSE)

$$i\hbar\frac{\partial}{\partial t}\left|\Psi(t)\right\rangle = H(t)\left|\Psi(t)\right\rangle \tag{2.11}$$

for the full Hamiltonian $H(t) = H_{\text{field-free}} + H_{\text{int}}(t)$. Here, $H_{\text{field-free}}$ is the field-free Hamiltonian of the system under consideration (see previous sections) and $H_{\text{int}}(t)$ is the interaction potential (2.9), for the chosen electric field configuration. The time-dependent wave function $\big|\Psi(t)\big\rangle$ is expanded in a basis set of the eigenstates of the respective field-free Hamiltonian, which are obtained by solving the associated time-independent Schrödinger equation. The alignment and orientation are quantified by expectation values such as $\big\langle\cos^2\theta\big\rangle$ and $\langle\cos\theta\rangle$, θ being the Euler angle between the molecular z axis and laboratory fixed Z axis.

The computation of the time-dependent alignment and orientation of molecules consists of four steps.

(i) Solving the TISE for $H_{\text{field-free}}$ to determine the field-free energies and eigenstates

(ii) Calculating the matrix elements of electric-dipole moment, polarizability and other tensors in the basis of the field-free eigenstates

(iii) Solving the TDSE using the field-free eigenstates as a basis set

(iv) Calculating observables as expectation values of tensor operators

The calculation of the field-free eigenstates (i) can be further divided into substeps depending on whether internal rotations or quadrupole-coupling effects are included. Examples for such calculations can be found in Appendix A.

2.6.1. Calculation of field-free energy levels

Rigid rotor

To numerically solve the TISE for the rigid-rotor Hamiltonian of an asymmetric top molecule, a symmetry adapted basis of Wang symmetric-top wave functions in the form given in [112] is used. The basis states are classified according to irreducible representations of either the MS group or the D_2 rotation group [113]. For a linear molecule, symmetry classification is unnecessary since there is only one energy level for each J (omitting the M-degeneracy). For each J, the matrix elements of the Hamiltonian (2.2) (or (2.4) for linear molecules) are constructed in this symmetry adapted basis and the eigenstates are obtained by diagonalizing each block of the resulting matrix separately. The rigid-rotor energy levels and eigenstates are computed using the python package Watie, see section A.1.

Internal rotations

Here, the field-free basis set we seek consists of the eigenstates of the rotation-torsion Hamiltonian (2.7). To solve the TISE, the torsional potential and structural parameters are required as analytical functions of the torsional angle τ. From the structural parameters the kinetic-energy matrices in Equation 2.7 can then be obtained as functions of τ as well [110, 114]. The construction of a matrix representation of $H_{\text{rot-tor}}$ is divided into several steps. The first step is the computation of rigid-rotor eigenfunctions for the equilibrium geometry of the molecule, i. e., solving the TISE for the Hamiltonian (2.7a) and $\tau = \tau_{eq}$. In the second step the torsional eigenfunctions of the Hamiltonian (2.7b) are determined using a suitable basis set, e. g., sine and cosine functions or plane waves. The matrix elements of $H_{\text{rot-tor}}$ are then constructed in the basis set given by the product states of pure rotational and torsional eigenfunctions. Finally, the field-free eigenstates and energy levels are computed by diagonalizing the resulting Hamiltonian matrix. The calculation of rotation-torsional energy levels and eigenstates is carried out using the program libtrove, see section A.2.

Hyperfine energy levels

The computation of the spin-rotational states forming the field-free basis builds on the previous calculation of rigid-rotor states, see above. To numerically solve the TISE, the matrix elements of $H_{\text{rot-qc}}$ are build in a basis of coupled states $|F, \mathcal{I}, J, u\rangle$ [111, 112], where $\mathcal{I}$ is a collection of spin quantum numbers and u represents additional rotational quantum numbers. The construction of the Hamiltonian matrix requires the matrix elements of the electric-field-gradient tensor in the rigid-rotor basis, see subsection 2.6.2. Analogous to the cases above, the hyperfine energy levels and eigenfunctions are obtained from the diagonalization of the Hamiltonian matrix. Hyperfine energy levels are computed using the Python package HyPy, see section A.3.

2.6.2. Calculation of Cartesian tensor matrix elements

Numerically solving the TDSE for a molecule in external electric fields or calculating energy levels including nuclear-quadrupole coupling requires a matrix representation of the Cartesian tensor operators in Equation 2.10 and Equation 2.8. Additionally, the numerical calculation of expectation values requires the matrix elements of the operator in question. Here, each Cartesian tensor of rank Ω is represented in the form [115]

$$\left\langle J'v'M_J' \middle| T_A^{(\Omega)} \middle| JvM_J \right\rangle = \sum_{\omega=0}^{\Omega} \mathcal{M}_{A,\omega}^{(J',M_J',J,M_J)} \mathcal{K}_{\omega}^{(J',v',J,v)}, \tag{2.12}$$

where J and M_J are replaced by F and M_F in the case of hyperfine energy levels, v labels different eigenstates with the same J or F and A is a multi-index for the laboratory-frame Cartesian coordinates X, Y and Z. The $\mathcal{M}$ and $\mathcal{K}$ matrices decouple laboratory-frame quantum numbers M_J and M_J' from the molecule-frame quantum numbers v and v'.

The calculation of the elements of the $\mathcal{M}$ and $\mathcal{K}$ matrices is carried out in a manner analogous to determining the field-free eigenstates. The matrix elements

$$\left\langle \phi_{n'}^{J',M_J'} \middle| T_A^{(\Omega)} \middle| \phi_n^{J,M_J} \right\rangle = \sum_{\omega=0}^{\Omega} \mathcal{M}_{A,\omega}^{(J',M_J',J,M_J)} \mathcal{K}_{\omega}^{(J',n',J,n)} \tag{2.13}$$

are first computed in the basis sets $\left|\phi_n^{J,M_J}\right\rangle$ utilized to construct the respective Hamiltonian matrices. For the rigid-rotor case, the elements of $\mathcal{M}_{A,\omega}$ and $\mathcal{K}_\omega$ are calculated analytically in the basis of Wang states [115]. If internal rotations are included, the matrix elements are set up in the rotation-torsional product basis following the calculation of the purely rotational and torsional matrix elements of the tensors in question. For hyperfine states, the matrix elements of the electric-dipole moment and polarizability tensors as well as other Cartesian tensors can easily be constructed in the coupled basis [111] $|F, I, J, u\rangle$, since these tensors do not act on the nuclear-spin coordinates. After solving the TISE, the elements of $\mathcal{K}_\omega$ are transformed to the field-free eigenbasis $|JvM_J\rangle = \sum_n C_n^{J,v} \left|\phi_n^{J,M_J}\right\rangle$ of the system under consideration

$$\mathcal{K}_\omega^{(J',v',J,v)} = \sum_{n',n} \left[C_{n'}^{J',v'}\right]^* C_n^{J,v} \mathcal{K}_\omega^{(J',n',J,n)}. \tag{2.14}$$

The computations of matrix elements are carried out with the programs used for the respective calculations of energy levels and field-free wavefunctions, see above.

2.6.3. Solving the time-dependent Schrödinger equation

The numerical procedure to solve the TDSE has been described in detail in [115]. The time-dependent wave function $\left|\Psi(t)\right\rangle$ is expanded in the basis given by the eigenstates $|JvM_J\rangle$ of the field-free Hamiltonian

$$\left|\Psi(t)\right\rangle = \sum_{J,v,M_J} C_{J,v,M_J}(t) \left|JvM_J\right\rangle. \tag{2.15}$$

The time-dependent coefficients $C_{J,v,M_J}(t)$ are obtained by numerical solution of the TDSE employing the split operator method [116]. The basis states $|JvM_J\rangle$ yield a diagonal matrix representation of $H_{\text{field-free}}$. For the interaction Hamiltonian $H_{\text{int}}(t)$, the matrix elements are constructed from those of the electric-dipole moment or polarizability tensor, see subsection 2.6.2. Representing the Cartesian tensor operators in the form (2.12) is advantageous as it reduces the dimensionality of the matrix-vector products needed to solve the TDSE speeding up the calculations. The present approach is compatible with any level of theory used for the field-free basis as long as the operators like electric-dipole moment and polarizability are provided in the form (2.12). Finally, expectation values $\left\langle \Psi(t) \middle| \hat{O} \middle| \Psi(t) \right\rangle$ can be computed for any operator $\hat{O}$ expressed in the form Equation 2.12. The TDSE is solved using the computer program RichMol [115], see section A.4.

RichMol was applied to perform the calculations for which the results are presented in chapters 4–7. The results discussed in chapter 3 were obtained using a previously developed program [117] where the TDSE was solved by applying the short iterative Lanczos method [118, 119].

3 Time-dependent analysis of the mixed-field orientation of molecules without rotational symmetry[1]

3.1. Introduction

Directional control over complex molecules, i. e., their alignment and orientation in laboratory space, is strongly sought after for many applications, not the least in the quest for the recording of so-called molecular movies of (bio)chemical dynamics [14, 19, 20]. A detailed understanding of the underlying control mechanisms and the related rotational dynamics is necessary to guide experiments as well as to support the analysis of the actual imaging experiments, especially when no good experimental observables of the degree of alignment and orientation are available anymore.

Even for present day experiments with moderately small molecules the angular control strongly improves or simply enables the observation of steric effects in chemical reactions [27, 28] or in imaging experiments utilizing photoelectron angular distributions [2–4], high-order-harmonic-generation spectroscopy [8–10], and X-ray and electron diffractive imaging [11, 13, 17]. While these experiments typically have been performed for simpler molecules so far, molecules of the complexity of 6-chloropyridazine-3-carbonitrile (CPC) are within reach.

The generation as well as the basic concepts of alignment and orientation have been described before [31, 48, 49]. Here, we focus on mixed-field orientation, which utilizes the combined action of a strong laser field with a dc electric field [49, 55, 57, 61, 72]. This approach was experimentally shown to allow for three-dimensional (3D) alignment and one-dimensional (1D) orientation of the prototypical complex molecule CPC [54], but the employed adiabatic analysis of the quantum dynamics could not reproduce the experimental findings [54, 56].

Here, we set out to accurately theoretically describe the rotational dynamics of a thermal ensemble of CPC under the combined action of laser pulses and dc electric fields. We investigate the influence of the dc field strength as well as the angle between the fields as the ac field strength changes during the turn-on of the linearly and elliptically polarized laser fields. Our findings demonstrate that the rotational dynamics is very complex, and can be quantitatively described as a solution of the time-dependent Schrödinger equation.

---

[1] This chapter is based on the publication: *Time-dependent analysis of the mixed-field orientation of molecules without rotational symmetry*, Linda V. Thesing, Jochen Küpper and Rosario González-Férez, J. Chem. Phys. **146**, 244304 (2017), arXiv:1705.03225 [physics.chem-ph]. I optimized the computational code, performed the calculations, analyzed the data and contributed to writing the manuscript

3.2. Theoretical Description

We consider a planar, polar, asymmetric top molecule with a polarizability tensor that is diagonal in the principle-axes-of-inertia system and an electric dipole moment (EDM) that is not parallel to any principle axis of inertia. We investigate the rotational dynamics of such a molecule in combined non-resonant laser and dc electric fields where the laser field is either linearly or elliptically polarized. The (major) polarization axis of the laser defines the Z-axis of the laboratory-fixed frame (LFF) (X, Y, Z) and for an elliptically polarized laser, the LFF Y-axis is defined by the minor polarization axis. The static field lies in the YZ-plane forming an angle β with the Z-axis. The molecule-fixed frame (MFF) (x, y, z) is defined by the principle axes of inertia in such a way that the rotational constants satisfy $B_z > B_y > B_x$. The MFF is related to the LFF by the Euler angles (ϕ, θ, χ).

Within the rigid rotor approximation, the Hamiltonian of the system is

$$H(t) = J_x^2 B_x + J_y^2 B_y + J_z^2 B_z + H_{\text{stat}} + H_{\text{laser}}(t) \tag{3.1}$$

where J_i are the components of the angular momentum with respect to the i-axis, $i \in \{x, y, z\}$. The interaction of the molecule with the static electric field reads

$$H_{\text{stat}} = -\mathbf{E}_{\text{stat}} \cdot \boldsymbol{\mu} = -\mathbf{E}_{\text{stat}} \mu_z \cos\theta_{sz} - \mathbf{E}_{\text{stat}} \mu_y \cos\theta_{sy} \tag{3.2}$$

with the dc field strength $\mathbf{E}_{\text{stat}}$, the components μ_y and μ_z of the EDM $\boldsymbol{\mu}$ and the angles θ_{sz} and θ_{sy} between the static electric field and the MFF z- and y-axes, respectively (see ref. 54 for their relations to the Euler angles). The interaction of the molecule with the non-resonant laser field reads

$$\begin{aligned} H_{\text{laser}}(t) = &-\frac{I_{ZZ}(t)}{2c\varepsilon_0}\left(\alpha^{zx}\cos^2\theta_{Zz} + \alpha^{yx}\cos^2\theta_{Zy}\right) \\ &-\frac{I_{YY}(t)}{2c\varepsilon_0}\left(\alpha^{zx}\cos^2\theta_{Yz} + \alpha^{yx}\cos^2\theta_{Yy}\right) \end{aligned} \tag{3.3}$$

where $I_{ZZ}(t)$ and $I_{YY}(t)$ are the time-dependent intensities along the major and minor laser-field polarization axes, respectively. For linear polarization, $I_{YY}(t) = 0$ and the total intensity is given by $I(t) = I_{ZZ}(t)$; for elliptical polarization $I(t) = I_{ZZ}(t) + I_{YY}(t)$ and we assume $I_{ZZ}(t) = 3I_{YY}(t)$. In (3.3), $\alpha^{ij} = \alpha_{ii} - \alpha_{jj}$, where α_{ii} are the diagonal elements of the polarizability tensor with $i, j \in \{x, y, z\}$. θ_{Pq} is the angle between the LFF P-axis and the MFF q-axis [54].

To investigate the rotational dynamics of the CPC molecule in combined ac and dc fields, we solve the time-dependent Schrödinger equation (TDSE) associated with the Hamiltonian (3.1). For the angular coordinates, we employ a basis set expansion of the wave function using linear combinations of field-free symmetric rotor states, i. e., Wigner functions [105], which respect the symmetries of the Hamiltonian. In the case of tilted fields with $\beta \neq 90\,^\circ$, the remaining symmetry operations of the Hamiltonian (3.1) are the identity E and the reflection σ_{YZ} on the YZ-plane, which contains the dc and

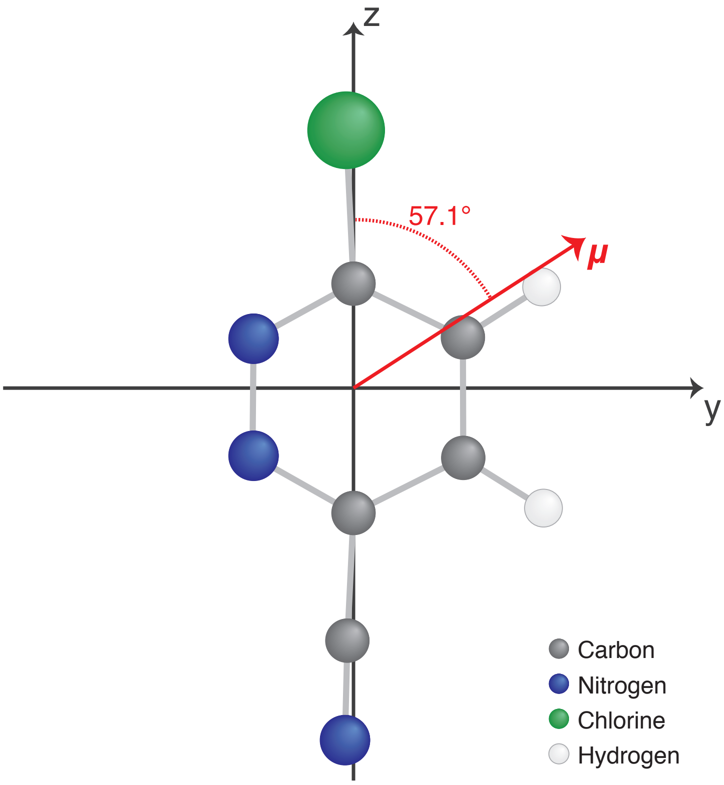

Figure 3.1.: Sketch of the structure of the CPC molecule. The x-axis is perpendicular to the figure plane.

i	B_i (MHz)	α_{ii} (10^{-3} nm^3)	μ_i (D)
x	639.708	7.88	0
y	717.422	11.98	4.37
z	5905.0	22.24	2.83

Table 3.1.: Rotational constants, polarizability components and components of the EDM of the CPC molecule [54]. In the calculation of the rotational constants, the ^{35}Cl isotope was considered.

ac electric fields, implying two irreducible representations. The basis used for each irreducible representation has been described elsewhere [120]. The time propagation is carried out using the short iterative Lanczos method [118, 119]. In our calculations, the dynamics during the turn-on of the static electric field is assumed to be adiabatic and the dc field-dressed states are taken as the initial states of the time-propagation. For the adiabatic labeling of the time-dependent states, the static electric field is first turned on parallel to the LFF Z-axis and, thereafter, rotated by an angle β.

This work focuses on the CPC molecule [54], which has an EDM of $\mu = 5.21$ D that forms an angle of 57.1° with the most polarizable axis (MPA) of the molecule, see Figure 3.1. The components of the EDM as well as the rotational constants and polarizability components of CPC are listed in Table 3.1. We use a field configuration equivalent to the experimental one [54], i. e., a Gaussian laser pulse with a peak intensity of $I_{\text{control}} = 8.0 \times 10^{11}$ W/cm^2 and a full-width at half maximum (FWHM) of 10 ns, and a tilted dc electric field with a field strength of 571 V/cm.

In the experiment [54], an inhomogeneous electric field was used to deflect the molecules according to the effective dipole moments of their rotational states [71, 121]. The dispersed molecular beam then entered a velocity map imaging (VMI) spectrometer where it was crossed by the alignment and probe laser pulses. A state-selection of the sample was carried out by focusing the laser beams on the most deflected molecules, which are the ones in the lowest-energy rotational states [71]. The alignment and orientation of the CPC molecules was measured by Coulomb explosion imaging of ionic fragments onto a screen perpendicular to the dc electric field. The measured orientation corresponds to the average orientation of the molecules occupying different rotational states in the state-selected molecular ensemble.

The degree of orientation is experimentally quantified by the ratio $\mathrm{N}_{\mathrm{up}}/\mathrm{N}_{\mathrm{tot}}$ of Cl^{+} ions that are detected in the upper half of the screen to the total number of detected ions. In our calculations, we determine this orientation ratio by projecting the 3D probability density onto a 2D screen perpendicular to the dc electric field [56]. Here, we take into account the probe selectivity for a probe pulse that is linearly polarized parallel to the screen. The volume effect due to the spatial intensity profiles of the alignment and probe lasers is not included in this work. We mimic the state-selection, which results in a non-thermal population distribution, by using a thermal ensemble at a temperature of 200 mK, which is lower than the (1 K) rotational temperature of the non-deflected molecular sample and was found to describe the non-thermal experimental ensemble well. We solve the TDSE for each state $|\psi_\gamma\rangle$ in the thermal ensemble and determine the thermal orientation ratio as

$$\frac{\mathrm{N}_{\mathrm{up}}}{\mathrm{N}_{\mathrm{tot}}} = \sum_\gamma w_\gamma^T \frac{\mathrm{N}_{\mathrm{up}}^\gamma}{\mathrm{N}_{\mathrm{tot}}^\gamma} \tag{3.4}$$

with the thermal weights according to a Boltzmann distribution

$$w_\gamma^T = \frac{e^{-E_\gamma/k_B T}}{\sum_\gamma e^{-E_\gamma/k_B T}} \tag{3.5}$$

with the field-free energy E_γ of the state $|\psi_\gamma\rangle$. For the thermal ensemble at 200 mK, we take into account the 50 lowest lying rotational states of each irreducible representation, i. e., 100 rotational states are included in the sums (3.4) and (3.5).

3.3. Orientation of a thermal ensemble and comparison to experimental results

Figure 3.2 shows the theoretical orientation for a thermal ensemble at $T = 200$ mK at the control laser peak as a function of the angle β between the dc field and the LFF Z-axis for linearly and elliptically polarized laser fields. These results are in very good agreement with the experimental orientation ratios for the state-selected molecular sample, which are reproduced from ref. 54. We observe similar results for the linearly and elliptically

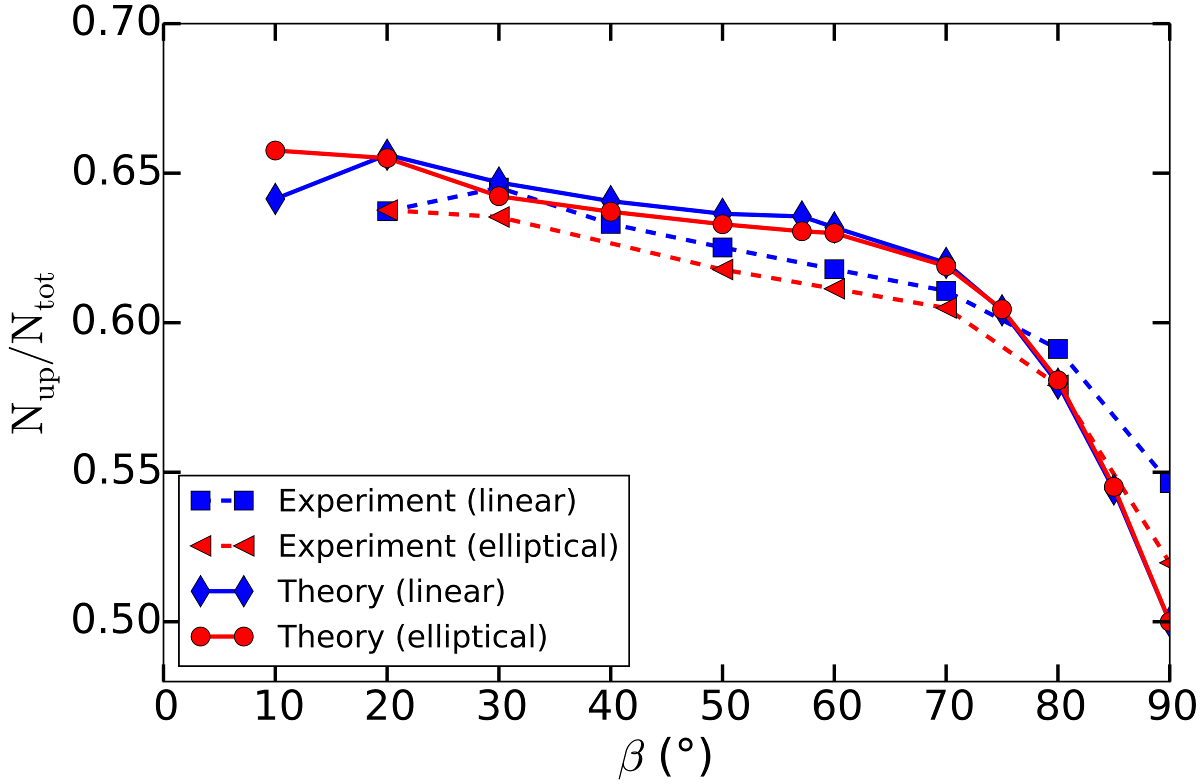

Figure 3.2.: The orientation ratio N_{up}/N_{tot} at the peak of the laser pulse, $I_{control} = 8.0 \times 10^{11}$ W/cm^2, as a function of β for linearly and elliptically polarized pulses, computed for a thermal ensemble at $T = 200$ mK (red diamonds and blue circles, respectively) and experimental results for a state-selected sample (red squares and blue triangles), see Fig. 5 from ref. 54. The dc field strength is 571 V/cm.

polarized laser fields: The orientation of the thermal ensemble increases smoothly as the static field is rotated towards the (major) polarization axis of the laser, and reaches values of $\mathrm{N_{up}/N_{tot}} \sim 0.65$ for small β. For linear polarization, $\mathrm{N_{up}/N_{tot}}$ decreases for $\beta = 10\,^\circ$ due to the employed geometry of the experimental setup, which cannot correctly measure the orientation for parallel fields [57]. Overall, our time-dependent description of the mixed-field orientation of state-selected CPC reproduces the features of the experimentally observed behavior well. In particular, we find a good agreement between the experimental and theoretical orientation ratio for $\beta \lesssim 70\,^\circ$. For $\beta = 90\,^\circ$, the experimental ensemble shows a small orientation which contradicts the theoretical prediction of no orientation for perpendicular fields. This could be due to experimental imperfections such as misalignment of the dc field, the polarization axis and detector screen or due to the influence of the probe laser. We point out that the smooth behavior of $\mathrm{N_{up}/N_{tot}}$ is a consequence of the ensemble average. The orientation of an individual state might strongly depend on β due to highly non-adiabatic effects appearing in the rotational dynamics, see section 3.4 below. These non-adiabatic effects are masked by the ensemble average.

Figure 3.3 shows the calculated expectation values of the orientation cosines along the LFF Z and Y-axes as well as the dc field direction for the same thermal sample and field configurations. The ratio $\mathrm{N_{up}/N_{tot}}$ plotted in Figure 3.2 quantifies the orientation of the MFF z-axis along the major polarization axis of the laser, providing information about 1D orientation, which is also characterized by $\langle\cos\theta_{Zz}\rangle_T$ shown in Figure 3.3 (a). To investigate the 3D orientation, we additionally consider the expectation value $\langle\cos\theta_{Yy}\rangle_T$, shown in Figure 3.3 (b), which measures the orientation of the MFF y-axis along the LFF Y-axis. The orientation of the EDM along the dc field direction is quantified by $\langle\cos\theta_{s\mu}\rangle_T$, presented in Figure 3.3 (c).

For the linearly polarized laser field, the thermal sample is strongly aligned along the Z-axis, but not aligned along the Y-axis, as presented in Figure 3.4. Strong 3D alignment is obtained with the elliptically polarized laser field, yielding $\langle\cos^2\theta_{Zz}\rangle_T \approx 0.95$ and $\langle\cos^2\theta_{Yy}\rangle_T \approx 0.83$ for all β. The alignment cosine $\langle\cos^2\theta_{Yy}\rangle_T$ shows a weak dependence on dc field and on the angle β.

The orientation of the thermal ensemble, Figure 3.3 (a), shows a smooth behavior, with $\langle\cos\theta_{Zz}\rangle_T$ increasing from 0.09 to 0.29 for $\beta = 85\,^\circ$ and $\beta = 10\,^\circ$, respectively. This increase is not reproduced within the adiabatic picture, which predicts a β-independent orientation for a weak static electric field [54]. The small orientation for β close to $90\,^\circ$ in Figure 3.3, obtained from the time-dependent results, can be explained by population transfer within pendular doublets formed as the laser intensity rises [55, 57, 122, 123]. At this field configuration, the oriented and antioriented adiabatic states within these near-degenerate pairs have similar contributions to the field-dressed dynamics reducing the orientation of the ensemble.

We now turn to the influence of a strong dc electric field on the orientation. For a dc field of 20 kV/cm, the thermal orientation $\langle\cos\theta_{Zz}\rangle_T$ rapidly increases as the angle between the fields decreases. For $\beta = 10\,^\circ$, we find a strong orientation with $\langle\cos\theta_{Zz}\rangle_T = 0.94$ and $\langle\cos\theta_{Zz}\rangle_T = 0.90$ for linearly and elliptically polarized pulses, respectively. The

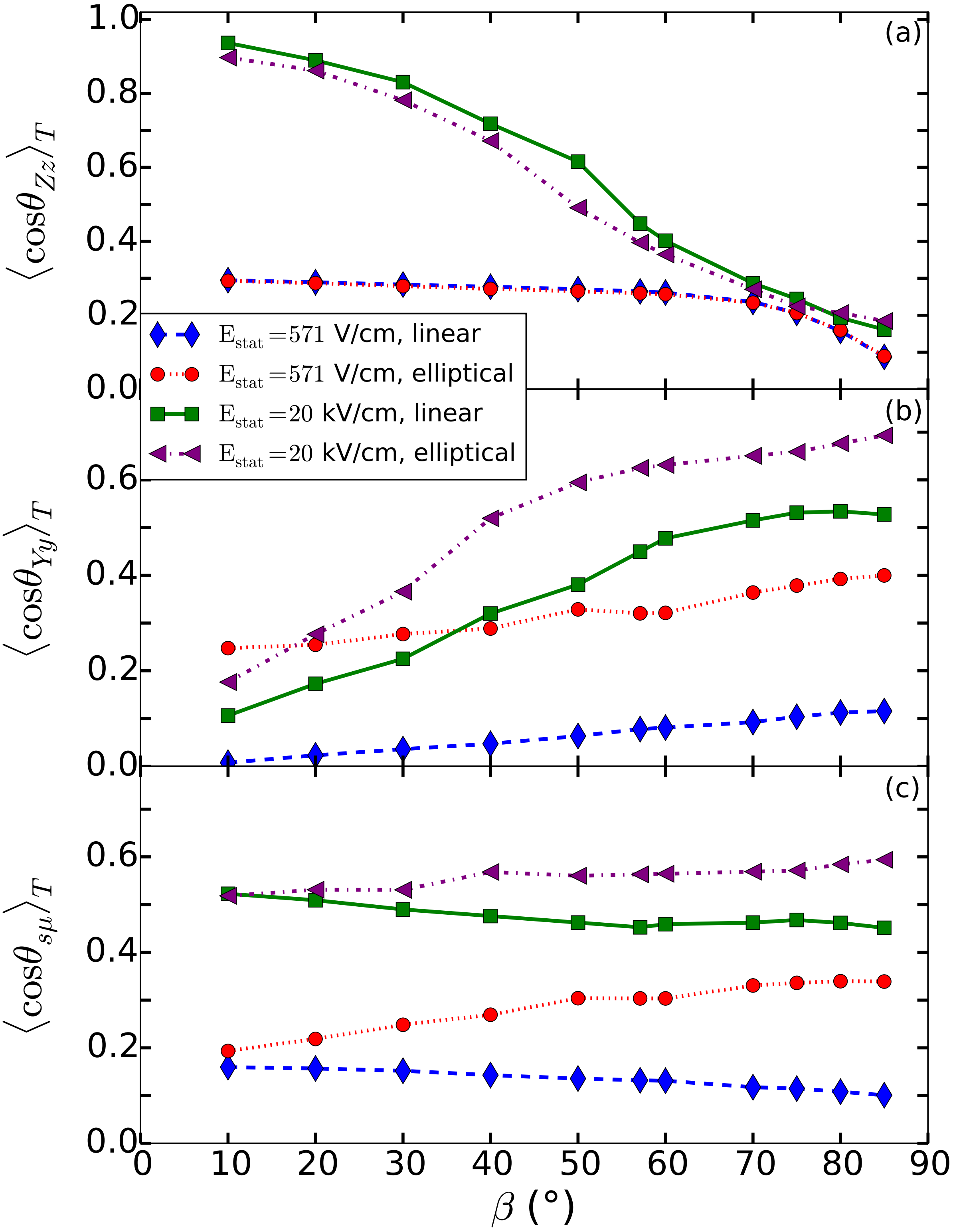

Figure 3.3.: For a thermal ensemble at $T = 200$ mK, the expectation values (a) $\langle\cos\theta_{Zz}\rangle_T$, (b) $\langle\cos\theta_{Yy}\rangle_T$ and (c) $\langle\cos\theta_{s\mu}\rangle_T$ at the laser peak intensity as a function of β for a linearly polarized ac field and with $\mathbf{E}_{\text{stat}} = 571$ V/cm (blue diamonds) and $\mathbf{E}_{\text{stat}} = 20$ kV/cm (green squares) as well as for an elliptically polarized ac field with $\mathbf{E}_{\text{stat}} = 571$ V/cm (red circles) and $\mathbf{E}_{\text{stat}} = 20$ kV/cm (purple triangles).

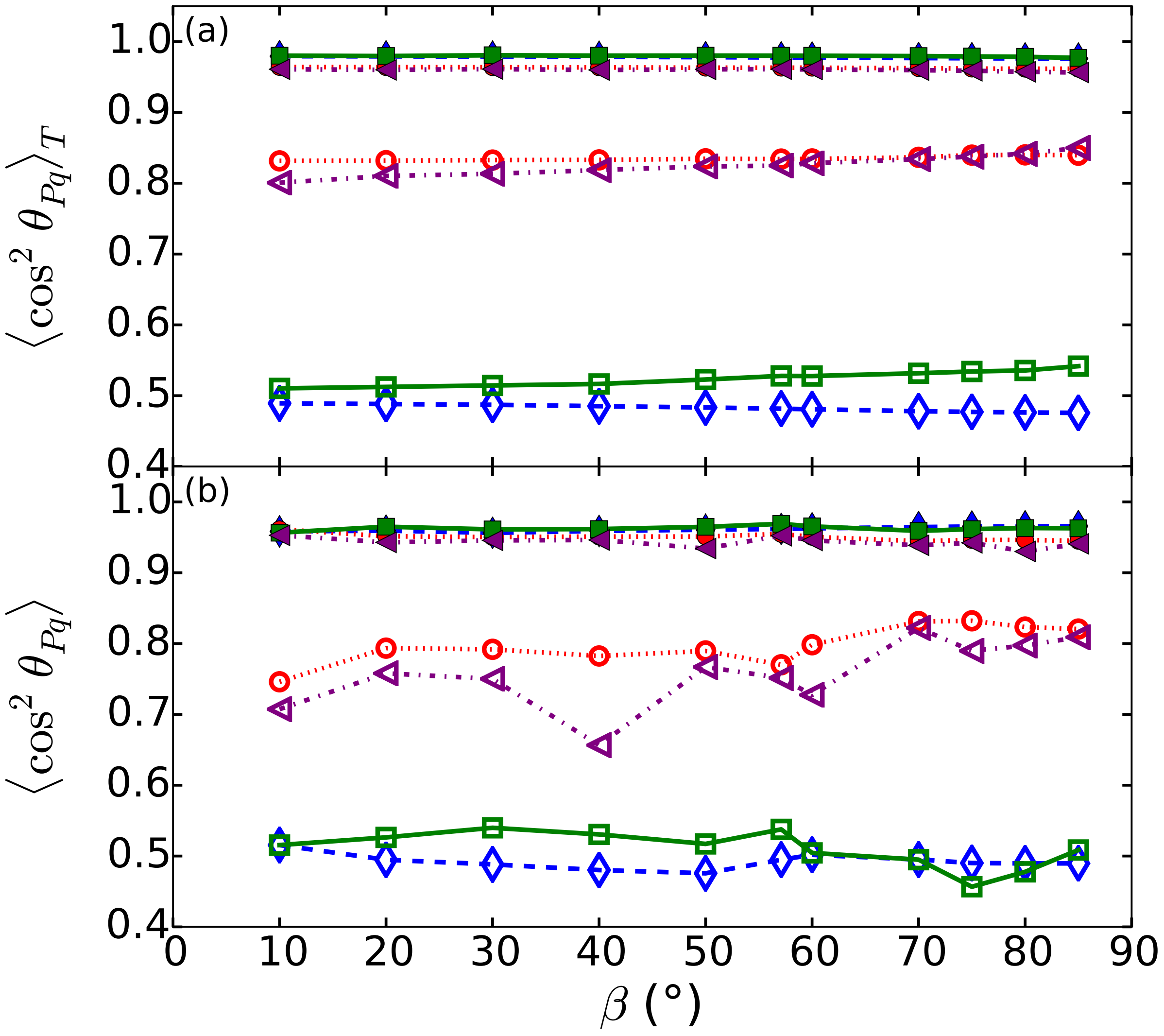

Figure 3.4.: For (a) a thermal ensemble at $T = 200$ mK, and (b) the state $|2_{12}1\rangle_\mathrm{t}$, the expectation values $\langle\cos^2\theta_{Zz}\rangle$ (filled symbols) and $\langle\cos^2\theta_{Yy}\rangle$ (empty symbols) at the laser peak intensity as a function of β for a linearly polarized ac field and with $\mathbf{E}_\mathrm{stat} = 571$ V/cm (blue diamonds) and $\mathbf{E}_\mathrm{stat} = 20$ kV/cm (green squares) as well as for an elliptically polarized ac field with $\mathbf{E}_\mathrm{stat} = 571$ V/cm (red circles) and $\mathbf{E}_\mathrm{stat} = 20$ kV/cm (purple triangles). The alignment along the LFF Z-axis is practically independent of all parameters with values of $\langle\cos^2\theta_{Zz}\rangle_T \approx 0.97$ and $\langle\cos^2\theta_{Zz}\rangle \approx 0.95$ for the thermal ensemble and the $|2_{12}1\rangle_\mathrm{t}$ state, respectively.

enhancement of the orientation can be rationalized in terms of the rotational dynamics of each state in the thermal ensemble, i. e., the contributions of different instantaneous eigenstates of the Hamiltoninan (3.1) to the time-dependent wave function, see section 3.4. For low laser intensities, the interaction with the dc field is dominant, inducing a brute-force orientation of the EDM along the dc field direction. If β is small, this brute-force orientation implies a moderate orientation of the MFF z-axis along the LFF Z-axis, due to the angle between the EDM and the MFF z-axis. As the laser intensity increases and becomes the dominant interaction, the strong dc field leads to preferred contributions of oriented pendular states to the time-dependent wave functions, which results in an enhancement of the orientation of the thermal ensemble.

Considering the orientation of the MFF y-axis along the LFF Y-axis, shown in Figure 3.3 (b), the thermal ensemble is very weakly oriented for a linearly polarized pulse and $\mathbf{E}_{\text{stat}} = 571$ V/cm, reaching a maximum value of $\langle\cos\theta_{Yy}\rangle_T = 0.12$ at $\beta = 85\,^\circ$. However, a strong dc electric field induces a brute-force orientation of the EDM, and thus, a moderate orientation of the molecular y-axis, along the dc field direction before the laser pulse is turned on. This orientation of the MFF y-axis is maintained to some extend even in the presence of the laser field with $\langle\cos\theta_{Yy}\rangle_T$ increasing from 0.11 to 0.53 for $\beta = 10\,^\circ$ and $\beta = 85\,^\circ$, respectively, at the peak of the linearly-polarized laser pulse. Thus, a strong dc field combined with a linearly polarized ac field induces a significant 3D orientation for intermediate β. In contrast, even a weak dc field induces a moderate 3D orientation when combined with an elliptically polarized laser field. Here, the orientation along the Y-axis monotonically increases from $\langle\cos\theta_{Yy}\rangle_T = 0.25$ to $\langle\cos\theta_{Yy}\rangle_T = 0.40$ for $\beta = 10\,^\circ$ to $\beta = 85\,^\circ$, respectively. For $\mathbf{E}_{\text{stat}} = 20$ kV/cm, we find an enhancement of $\langle\cos\theta_{Yy}\rangle_T$, similar to the behavior of $\langle\cos\theta_{Zz}\rangle_T$ for strong dc fields, but for increasing β. If β is small, the influence of the static field along the Y-axis is not strong enough to, in general, achieve preferred contributions of oriented pendular states to the rotational dynamics of excited states in the thermal ensemble. As a result, for $\beta = 10\,^\circ$ we encounter a few low-lying excited states in the molecular ensemble that are not oriented or even strongly antioriented along the Y-axis at the peak intensity. Compared to the weak dc field, $\langle\cos\theta_{Yy}\rangle_T$ is reduced at this angle. This effect disappears if the temperature is increased and more excited states contribute to the thermal ensemble.

Regarding the behavior of $\langle\cos\theta_{s\mu}\rangle_T$ in Figure 3.3 (c),[2] the orientation of the EDM along the dc field direction shows a weak dependence on β. For small angles between the ac and dc fields, $\langle\cos\theta_{s\mu}\rangle_T$ is approximately given by $\cos(57.1\,^\circ)\langle\cos\theta_{Zz}\rangle_T$, since for these small angles it holds $\langle\cos\theta_{sz}\rangle_T \approx \langle\cos\theta_{Zz}\rangle_T$. Thus, for both polarizations we find similar values of $\langle\cos\theta_{s\mu}\rangle_T \approx 0.18$ and $\langle\cos\theta_{s\mu}\rangle_T \approx 0.5$ for the weak and strong dc fields, respectively. For $\beta = 85\,^\circ$, the orientation of the EDM along the dc field direction is dominated by the behavior of $\langle\cos\theta_{Yy}\rangle_T$, and as a consequence, $\langle\cos\theta_{s\mu}\rangle_T$ is larger for the elliptically polarized laser field than for the linearly polarized laser field. The decreasing (increasing) behavior of $\langle\cos\theta_{s\mu}\rangle_T$ versus β for linear (elliptical) polarization is due to the larger contribution of $\langle\cos\theta_{sy}\rangle_T$, since $\cos(57.1\,^\circ) < \sin(57.1\,^\circ)$. In addition, for the linear polarized case we find that $\langle\cos\theta_{Yy}\rangle_T$ for $\beta = 85\,^\circ$ is smaller than $\langle\cos\theta_{Zz}\rangle_T$ for

---

[2] This expectation value is given by $\langle\cos\theta_{s\mu}\rangle = \cos(57.1\,^\circ)\langle\cos\theta_{sz}\rangle + \sin(57.1\,^\circ)\langle\cos\theta_{sy}\rangle$.

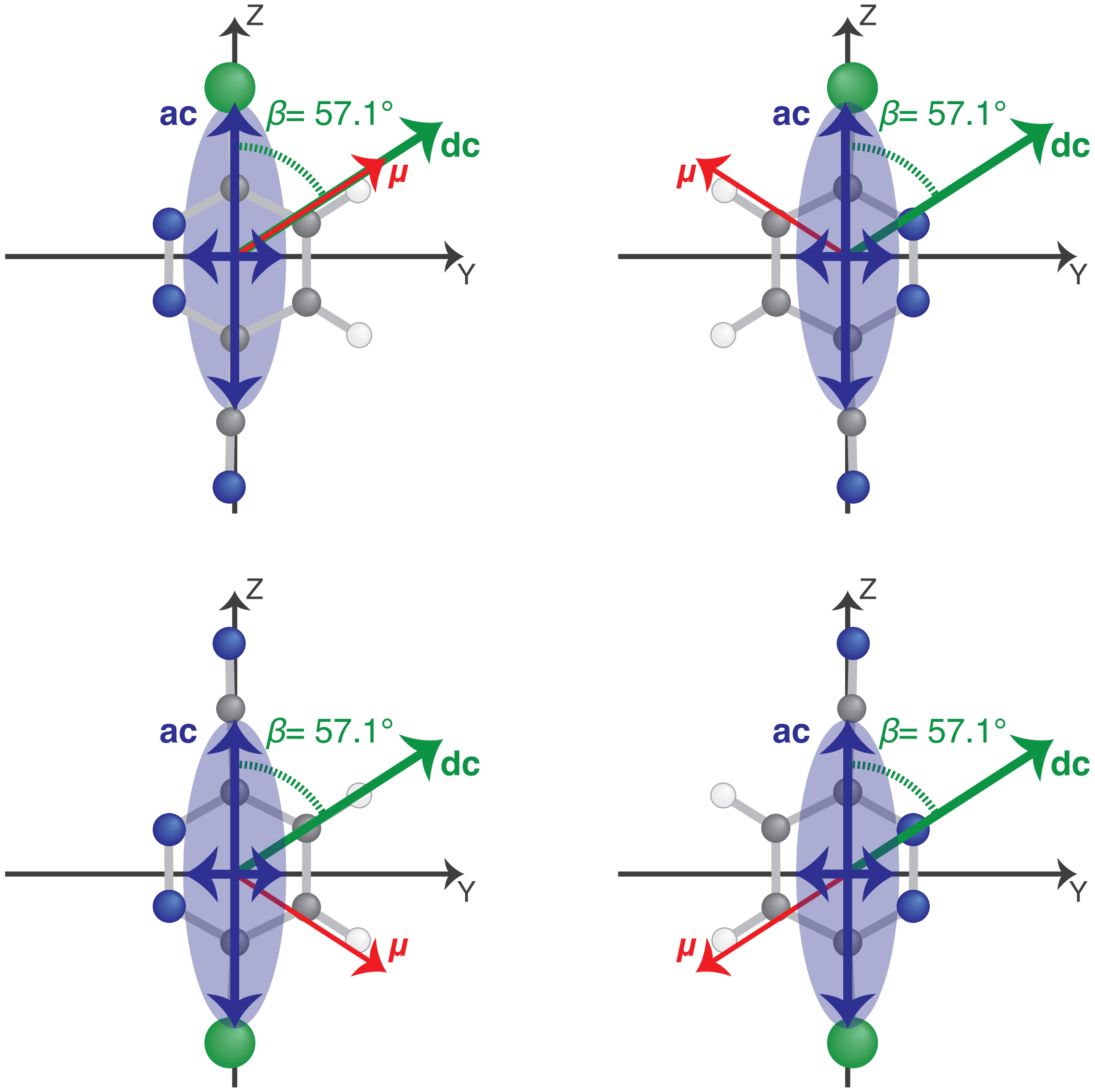

Figure 3.5.: For an elliptically polarized laser field, the four possible orientations of the 3D aligned pendular states in the adiabatic picture.

$\beta = 10\,^\circ$ for both dc field strengths. For $\beta = 57.1\,^\circ$, the angles between the ac and dc fields and between the EDM and the MPA coincide, and a maximum of $\langle\cos\theta_{s\mu}\rangle_T$ could be expected for the 3D aligned sample in an elliptically polarized laser field. However, this is not the case since the orientation of the EDM is obtained from the average over the four possible orientations of the adiabatic pendular states, shown in Figure 3.5, which contribute to the time-dependent wave function of each state in the thermal ensemble.

To summarize, a significant 3D orientation is obtained for intermediate angles β, a strong dc field and both, linear and elliptical, laser polarizations. The degree of orientation of the MFF y-axis along the LFF Y-axis is larger for an elliptically polarized pulse than for a linearly polarized one, whereas the orientation of the MFF z-axis along the LFF Z-axis is similar in both cases. This implies that to achieve a large 3D orientation an elliptically polarized laser is recommended. Nevertheless, we point out that the naive picture of achieving 3D orientation by fixing one molecular axis, namely the MPA, with a linearly polarized laser field and a second axis, the EDM, with a dc electric field does (only) work in the limit of strong laser and strong dc electric fields.

3.4. Field-dressed dynamics

To analyze the dynamics of individual excited states[3] for the different field configurations in detail, we choose the state $|2_{12}1\rangle_\mathrm{t}$ as a prototypical example. Energetically, it is the 14th and 19th excited state of the representation with even parity under the reflection σ_{YZ} for $\mathbf{E}_\mathrm{stat} = 571$ V/cm and $\mathbf{E}_\mathrm{stat} = 20$ kV/cm, respectively. In Figure 3.6 the orientation cosines $\langle\cos\theta_{Zz}\rangle$, $\langle\cos\theta_{Yy}\rangle$ and $\langle\cos\theta_{s\mu}\rangle$ at the peak intensity are presented as a function of β. The smooth β-dependence found for the orientation of the thermal ensemble is not reflected in the final orientation of the state $|2_{12}1\rangle_\mathrm{t}$. For instance, depending on the angle β, this state can be strongly 1D or 3D oriented, antioriented, or not oriented. However, certain features of the orientation of the thermal average can also be observed for the state $|2_{12}1\rangle_\mathrm{t}$ as well as for most other states contributing to the ensemble average at 200 mK. In particular, the significant orientation along the Z-axis for a strong dc field and small β and the decreasing orientation along the Z-axis for a weak dc field in the region $75\,^\circ \lesssim \beta < 90\,^\circ$. However, the exact orientation for a specific field configuration can only be determined from time-dependent calculations. In contrast, the alignment along the the Z-axis of the state $|2_{12}1\rangle_\mathrm{t}$, shown in Figure 3.4 (b), does not depend on β and resembles the alignment of the thermal sample. The alignment cosine $\langle\cos^2\theta_{Yy}\rangle$ shows a weak dependence on the angle between the ac and dc fields due to contributions of highly excited pendular states that are weakly aligned along the Y-axis.

The rotational dynamics shows highly non-adiabatic effects due to M-manifold splitting, avoided crossings and the formation of pendular doublets and quadruplets [123, 124]. The importance of each of these effects depends strongly on the field configuration, i. e., the ac and dc field strengths, the angle β between the fields, and the polarization

---

[3] We use the notations $|J_{K_aK_c}M\rangle_\mathrm{t}$ and $|J_{K_aK_c}M\rangle_\mathrm{p}$ for the time-dependent wave function and the adiabatic pendular states, respectively. Here, we only analyze the dynamics for states with even parity under reflection on the plane containing the ac and dc fields.

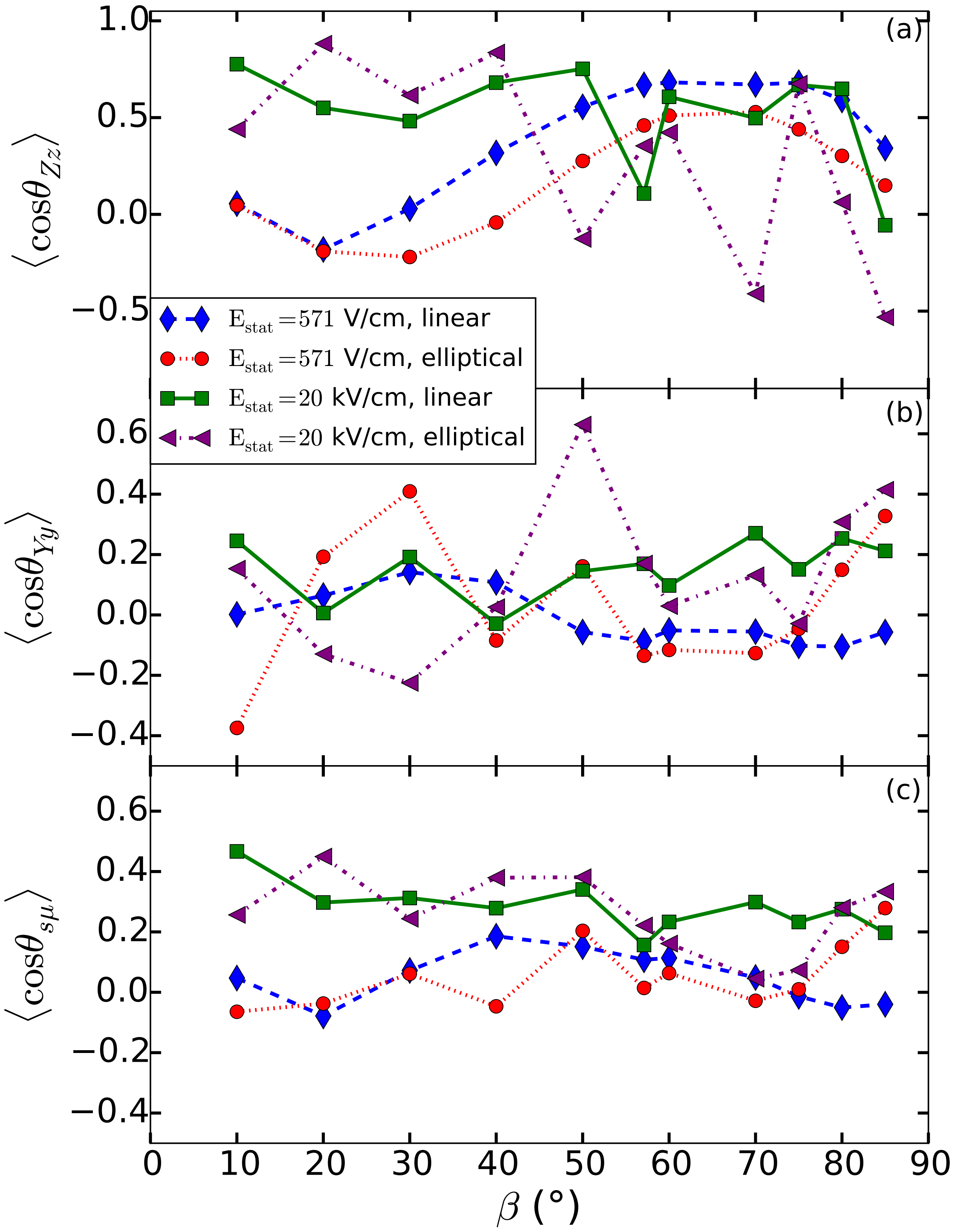

Figure 3.6.: The expectation values (a) $\langle\cos\theta_{Zz}\rangle$, (b) $\langle\cos\theta_{Yy}\rangle$ and (c) $\langle\cos\theta_{s\mu}\rangle$ for the state $|2_{12}1\rangle_t$ at the peak intensity as a function of β for a linearly polarized ac field and dc field strength $\mathbf{E}_{stat} = 571$ V/cm (blue diamonds) and $\mathbf{E}_{stat} = 20$ kV/cm (green squares) as well as for an elliptically polarized ac field and dc field strength $\mathbf{E}_{stat} = 571$ V/cm (red circles) and $\mathbf{E}_{stat} = 20$ kV/cm (purple triangles).

and temporal profile of the laser pulse. In this section, we investigate the influence of these non-adiabatic phenomena on the mixed-field orientation. For illustration, the time evolution of the rotational dynamics of the $|2_{12}1\rangle_\mathrm{t}$ state and the orientation cosines of the adiabatic pendular states are shown in movies provided in the supplementary material (see section 3.6).

3.4.1. Linearly polarized laser

We start by analyzing the dynamics for a linearly polarized laser field. Even at low intensities, the dynamics is highly complicated. This is illustrated in Figure 3.7 (a) and (b), which show the squares of the projection of the time-dependent wave function onto the adiabatic basis formed by the eigenstates of the instantaneous Hamiltonian (3.1). The dynamics is shown for a linearly polarized laser field through the intensity regime 10^9 W/cm^2 $\leq I(t) \leq 10^{10}$ W/cm^2 and both dc field strengths, $\mathbf{E}_\mathrm{stat} = 571$ V/cm and $\mathbf{E}_\mathrm{stat} = 20$ kV/cm. For this example we chose $\beta = 57.1\,^\circ$, which corresponds to the angle between EDM and MPA.

For a weak dc field of 571 V/cm, the population of the adiabatic pendular state $|2_{12}1\rangle_\mathrm{p}$ is already significantly reduced at 1.0×10^9 W/cm^2 compared to the laser field-free value of 1.0, see left side of Figure 3.7 (a). This is due to population transfer at the splitting of the $|2_{12}M\rangle_\mathrm{p}$ manifold with $M = 1, 2$ occurring at even lower intensities [124]. In contrast, for $\mathbf{E}_\mathrm{stat} = 20$ kV/cm, the energy gap between the states within this manifold is so large that their coupling is significantly reduced, preventing population transfer within the manifold as the ac field is turned on.

In this low intensity regime, the large number of avoided crossings, see Figure 3.7 (c) and (d), is the main source of the non-adiabatic behavior and leads to many adiabatic pendular states being involved in the dynamics. At each avoided crossing, the energy spacing among the involved pendular states strongly depends on the dc field strength and the angle between the ac and dc fields. Thus, the adiabatic pendular states contributing to the time-dependent wave function significantly vary for the dc field strengths considered here, cf. Figure 3.7 (a) and (b). By changing the angle β or any other field parameter, the contributions of the adiabatic pendular states to the time-dependent wave function also vary strongly (not shown here). We emphasize that avoided crossings play an important role during the whole rotational dynamics of excited states and are one of the main sources of non-adiabatic effects. The dynamics through an avoided crossing depends, additionally, on the temporal profile of the laser. Achieving completely adiabatic dynamics at arbitrary avoided crossings, i. e., no population transfer between the involved pendular states, would be very challenging since it requires an extremely slowly increasing intensity due to the extremely narrow spacing between the involved states; i. e., to achieve adiabatic dynamics corresponding to the energy and field-strength range presented in Figure 3.7 and Figure 3.10 microsecond-long laser pulses or a continuous-wave control laser [125] would be necessary.

At stronger laser fields, quasi-degenerate pendular doublets are formed providing an additional source of non-adiabatic effects. During the doublet formation with increasing

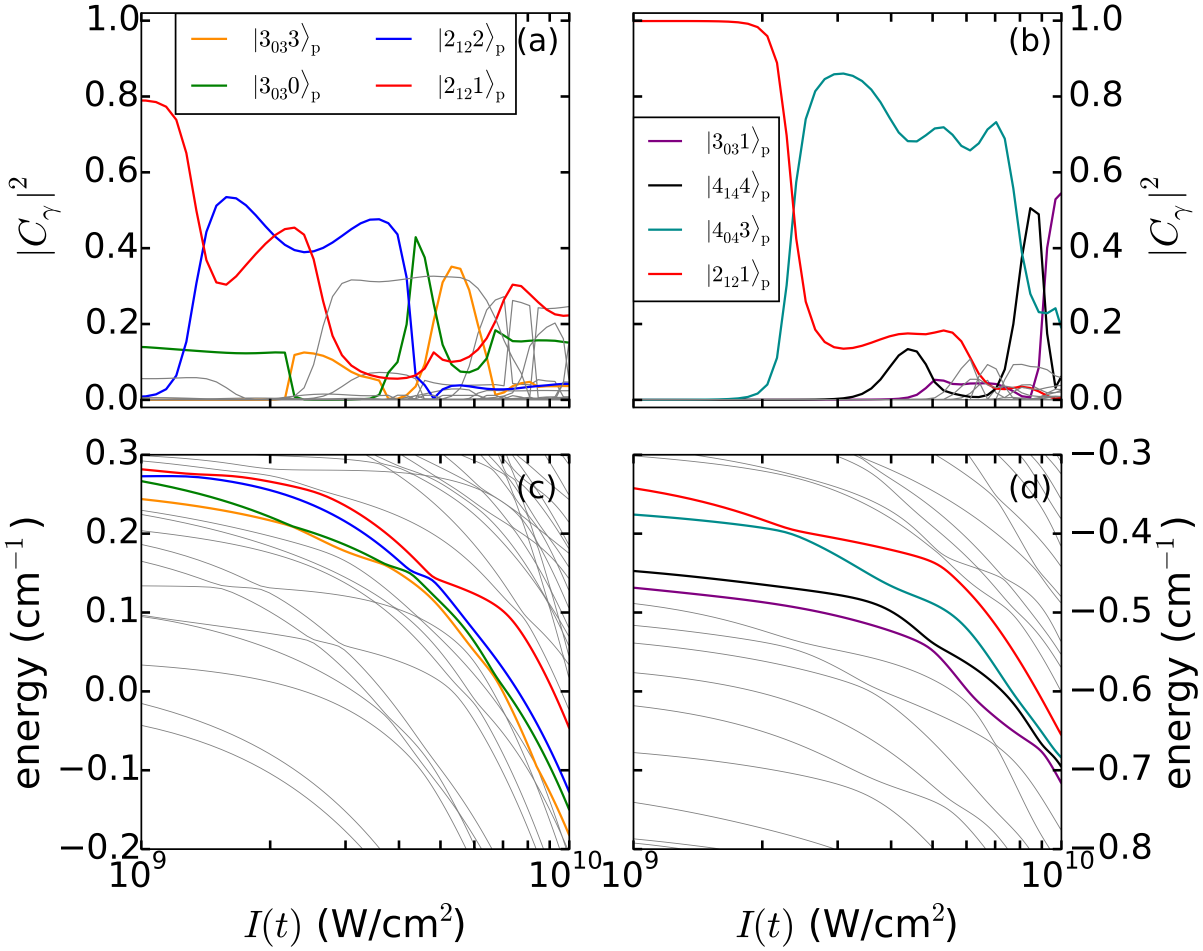

Figure 3.7.: The squares of the projection of the time-dependent wave function onto the adiabatic-pendular-state basis of the state $|2_{12}1\rangle_t$, for a linearly polarized ac field through the field-strength regime 1.0×10^9 W/cm^2 $\leq I(t) \leq 1.0 \times 10^{10}$ W/cm^2 and dc field strengths of (a) $\mathbf{E}_{\text{stat}} = 571$ V/cm and (b) $\mathbf{E}_{\text{stat}} = 20$ kV/cm. Energy level structure for the same intensities and dc field strengths (c) $\mathbf{E}_{\text{stat}} = 571$ V/cm and (d) $\mathbf{E}_{\text{stat}} = 20$ kV/cm. The angle between the ac and dc fields is $\beta = 57.1\,°$.

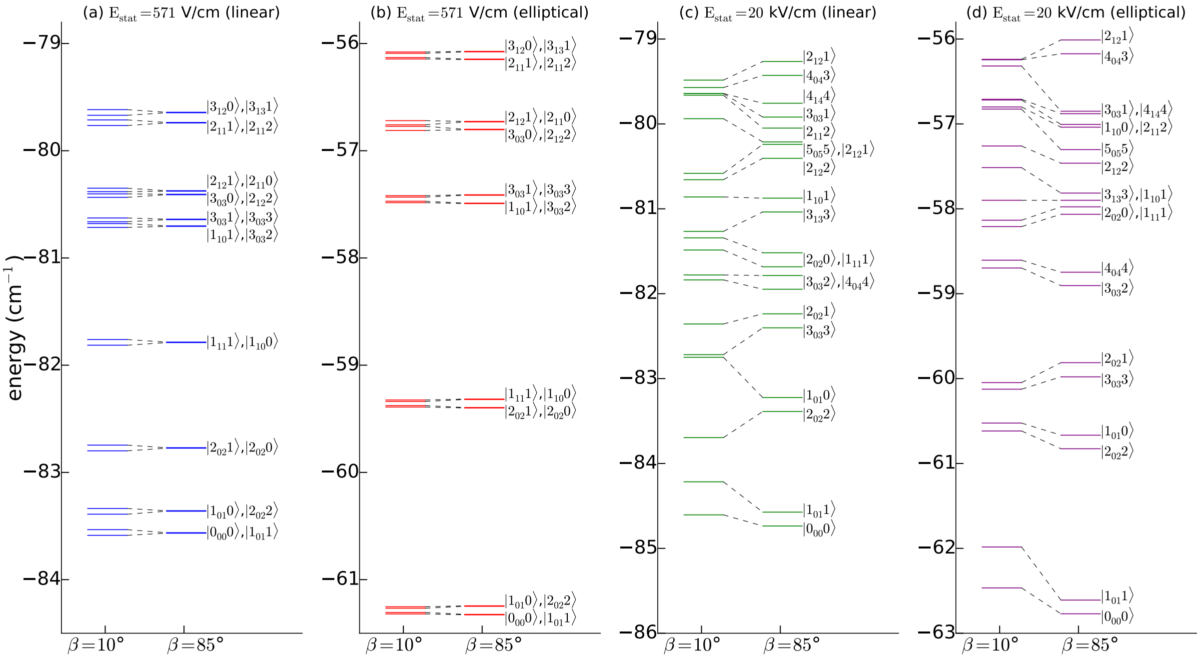

Figure 3.8.: The energies of the 20 lowest lying adiabatic pendular states with even parity under reflection on the plane containing the ac and dc fields, at the peak intensity for (a) linearly polarized ac field and $\mathbf{E}_{\text{stat}} = 571$ V/cm, (b) elliptically polarized ac field and $\mathbf{E}_{\text{stat}} = 571$ V/cm, (c) linearly polarized ac field and $\mathbf{E}_{\text{stat}} = 20$ kV/cm, (d) elliptically polarized ac field and $\mathbf{E}_{\text{stat}} = 20$ kV/cm.

$I(t)$, the energy splitting and the directional properties of the two pendular states change in a way that depends strongly on the external field parameters, in particular the dc field strength and the angle β. Thus, the influence of the doublet formation on the rotational dynamics and the mixed-field orientation at the peak intensity varies significantly if the field configuration is modified.

For $\mathbf{E}_{\text{stat}} = 571$ V/cm, the pendular doublets can be clearly observed for all values of β, see Figure 3.8 (a), which shows the energies of the 20 lowest lying adiabatic pendular states at the peak of the laser pulse for $\beta = 10\,°$ and $\beta = 85\,°$. The energy separation within these pendular doublets, $\Delta E \sim 2\mathbf{E}_{\text{stat}}\mu_z \cos\beta$, decreases as the dc field is rotated towards the perpendicular field configuration. For $\beta = 85\,°$, the small energy splitting and rapid formation of the pendular doublets with increasing laser intensity leads to a redistribution of the population within the quasi-degenerate doublets. This redistribution of the population for $\beta = 85\,°$ can be observed in the projection of the wave function onto the adiabatic basis at the peak intensity, shown in Figure 3.9 (a), where the two adiabatic pendular states in several doublets have similar weights. This can also be observed in the field-dressed-dynamics movies in the supplementary material (see section 3.6). Since the quasi-degenerate doublets consist of strongly aligned pendular states that are oriented in opposite directions along the LFF Z-axis, the overall orientation of the state $|2_{12}1\rangle_{\text{t}}$ at the peak intensity decreases as β approaches $90\,°$, see Figure 3.6 (a). A similar population redistribution within the pendular doublets also occurs for other excited states, and, as a result, the orientation of the thermal ensemble in Figure 3.3 (a) decreases as β approaches $90\,°$.

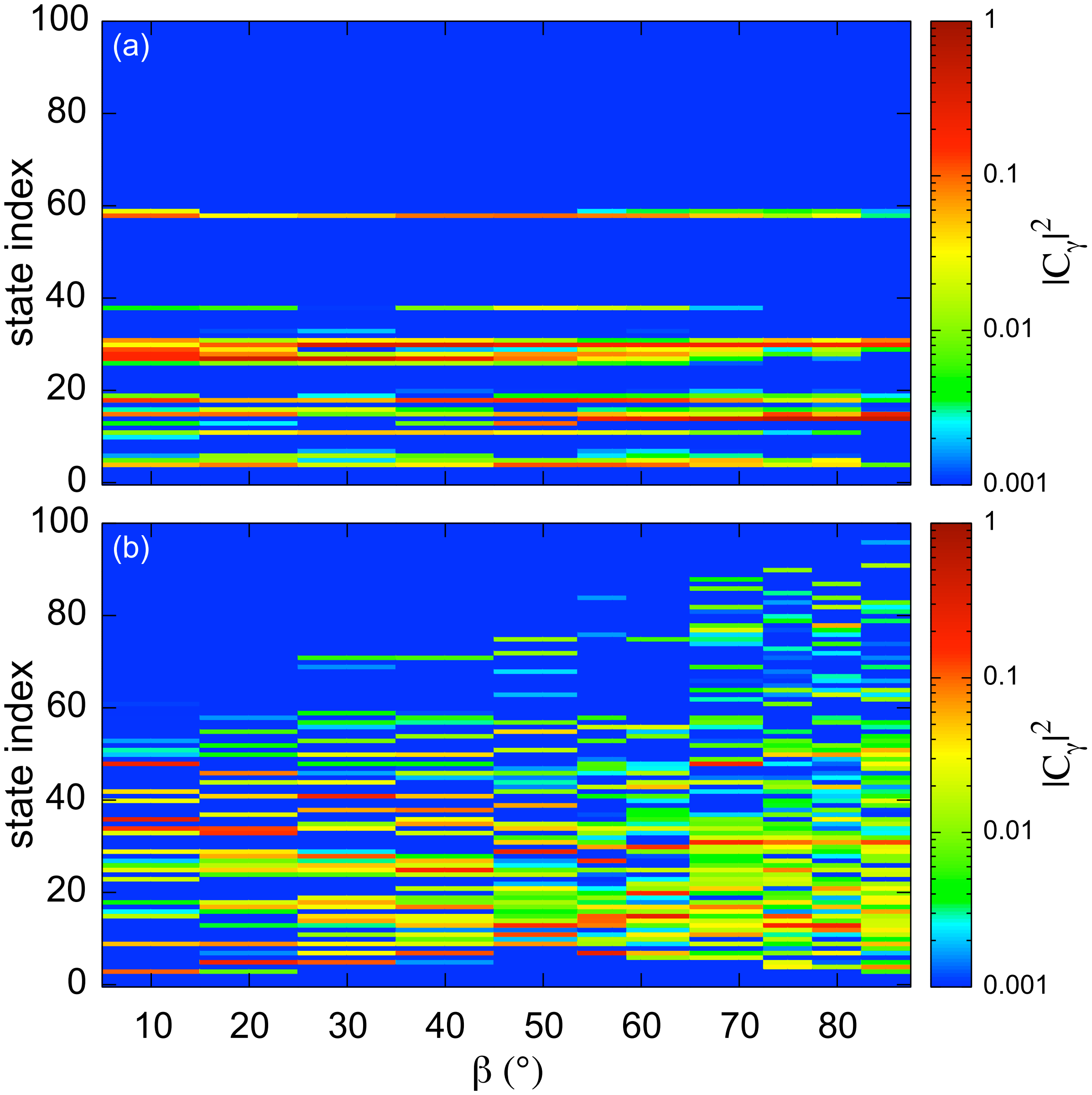

Figure 3.9.: For the state $|2_{12}1\rangle_\mathrm{t}$, the squares of the projection of the wave function at the peak of a linearly polarized laser pulse onto the adiabatic pendular states as a function of β and the index of the pendular states according to energetic order. The dc field strength is (a) $\mathbf{E}_\mathrm{stat} = 571$ V/cm and (b) $\mathbf{E}_\mathrm{stat} = 20$ kV/cm. The index of the adiabatic pendular state $|2_{12}1\rangle_\mathrm{p}$ is 14 and 19 for the weak and strong dc field, respectively.

As β decreases, the increasing Z-component of the dc field leads to larger energy splitting between the two adiabatic pendular states in the doublets. As a result, for small β we find less population transfer among the involved adiabatic pendular states than for β close to $90\,^\circ$. The weights of two adiabatic pendular states forming a quasi-degenerate pair can differ strongly at the peak intensity for $\beta \lesssim 70\,^\circ$, cf. Figure 3.9 (a). In the final population distribution in Figure 3.9 (a), we encounter gaps of unpopulated pendular states that can be explained by population transfer at avoided crossings occurring at high intensities. When the pendular doublets are already formed, we encounter avoided crossings involving four adiabatic pendular states. In these highly non-adiabatic avoided crossings, the population of the oriented (antioriented) state passes to the oriented (antioriented) state of the adjacent doublet (see section 3.6). Due to this mainly diabatic rotational dynamics at high intensities only a few adiabatic pendular states, distributed over a wide range of energies, significantly contribute to the final wave function. These pendular states mainly determine the orientation at different β. Depending on the angle between the ac and dc fields, the contributions of either oriented or antioriented adiabatic states are dominant in the final wave function. This leads to the oscillating behavior of $\langle\cos\theta_{Zz}\rangle$ versus β in Figure 3.6 (a).

For a strong dc field of $\mathbf{E}_{\text{stat}} = 20$ kV/cm, the arrangement in pendular doublets can still be observed for β close to $90\,^\circ$, where the energy separation within the doublets is much larger than for a weak dc field, see Figure 3.8 (c). For small angles, the lower lying adiabatic states do not form pendular doublets having opposite orientation, but there are nearly degenerate adiabatic states oriented in the same direction. For $\beta = 85\,^\circ$, due to the large energy separation, the pendular doublet formation does not lead to a significant population transfer between the two pendular states as for a weak dc field and the same angle. Thus, the field-dressed dynamics for $\mathbf{E}_{\text{stat}} = 20$ kV/cm is dominated by avoided crossings between neighboring levels. The population transfer occurring at these avoided crossings gives rise to a broad and homogeneous distribution of populated pendular states at the peak intensity, see Figure 3.9 (b). As a result, we find similar contributions of oriented and antioriented adiabatic pendular states for $\beta = 85\,^\circ$, giving rise to a small orientation along the Z-axis of the state $|2_{12}1\rangle_{\text{t}}$. We find other time-dependent excited states that are strongly oriented or antioriented at the peak intensity, depending on the weights of the adiabatic states in their final wave functions. The opposite orientations of these time-dependent states cancel in the thermal ensemble, which shows a weak orientation for $\beta = 85\,^\circ$.

If β is small, the initial brute-force orientation of the EDM, induced by the strong dc field, implies a significant orientation of the MFF z-axis along the LFF Z-axis before the laser pulse is turned on. For laser intensities above 1.0×10^{10} W/cm^2, the interaction with the ac field becomes dominant over the interaction with the dc field and the MPA becomes aligned along the Z-axis. Due to this strong confinement of the MPA, the orientation of many adiabatic pendular states along the Z-axis increases while some pendular states gradually become strongly antioriented. The change in the $\langle\cos\theta_{Zz}\rangle$ versus the laser intensity can be observed in the movies provided in the supplementary material (see section 3.6). The pendular states initially becoming antioriented in this intermediate intensity regime are mostly highly excited states that are not populated so that mainly oriented adiabatic states continue to contribute to the rotational dynamics in this regime. As the laser intensity increases further, we encounter numerous avoided crossings between these strongly oriented and strongly antioriented pendular states. At such an avoided crossing, the involved adiabatic pendular states interchange their directional properties, i. e., the previously oriented (antioriented) state becomes antioriented (oriented). Since these avoided crossings are traversed diabatically, the time-dependent wave function does not acquire population on the antioriented adiabatic pendular states. As a result, the distribution in Figure 3.9 (b) shows gaps of unpopulated adiabatic states that are mainly antioriented at the peak intensity. Thus, at the peak intensity, the state $|2_{12}1\rangle_{\mathrm{t}}$ is strongly oriented along the LFF Z-axis for small values of β, see Figure 3.6 (a). The dynamics of other excited states shows a similar behavior, thus enhancing the orientation of the thermal ensemble as seen in Figure 3.3 (a).

For β close to 90°, i. e., small angles between the dc field and the LFF Y-axis, the initial brute-force orientation of the EDM implies an orientation of the MFF y-axis along the LFF Y-axis before the laser pulse is turned on. This orientation is maintained for several adiabatic pendular states even at the peak intensity but we also find other pendular states being weakly antioriented or not oriented (see section 3.6). This leads to an overall moderate orientation of the MFF y-axis along the LFF Y-axis for the state $|2_{12}1\rangle_{\mathrm{t}}$ as well as the thermal average, for β close to 90°, see Figure 3.6 (b) and Figure 3.3 (b). If β is small, the dc electric field does not induce an initial orientation of the MFF y-axis along the LFF Y-axis. In the presence of the laser field, different time-dependent excited states may become moderately oriented in opposite directions or show no orientation along the LFF Y-axis at the peak intensity. Thus, the thermal ensemble shows a very small orientation $\langle\cos\theta_{Yy}\rangle_T$ for small β.

3.4.2. Elliptically polarized laser

We now consider the rotational dynamics in elliptically polarized laser fields. In the absence of the dc field, the elliptically polarized ac field induces 3D alignment of the CPC molecules, with the z and y molecular axes aligned along the LFF Z and Y-axes, respectively. Compared to the linearly polarized cases analyzed in the previous section, and since the total intensities for both polarizations are equal, the effective intensities of the elliptically polarized laser field along these two axes are weaker. This implies a smaller alignment along the Y-axis, as is illustrated in Figure 3.4. In this section, we analyze how this change in the ac field polarization affects the rotational dynamics and mixed-field orientation.

For low intensities, 10^9 W/cm$^2 \leq I(t) \leq$ 10^{10} W/cm^2, the squares of the projection of the time-dependent wave function for the state $|2_{12}1\rangle_{\mathrm{t}}$ are shown in Figure 3.10 (a) and (b) for $\beta = 57.1^\circ$ and $\mathbf{E}_{\mathrm{stat}} = 571$ V/cm and $\mathbf{E}_{\mathrm{stat}} = 20$ kV/cm, respectively. In this intensity regime, we find a similarly complex dynamics as for a linearly polarized laser field presented in Figure 3.7. For $\mathbf{E}_{\mathrm{stat}} = 571$ V/cm, the splitting of the $|2_{12}M\rangle_{\mathrm{p}}$ manifold at weaker intensities leads to population transfer among the two pendular states within this manifold. For a strong dc field with $\mathbf{E}_{\mathrm{stat}} = 20$ kV/cm, this effect is not significant and the population of the state $|2_{12}1\rangle_{\mathrm{p}}$, is still approximately 1.0 at 1.0×10^9 W/cm^2. The large

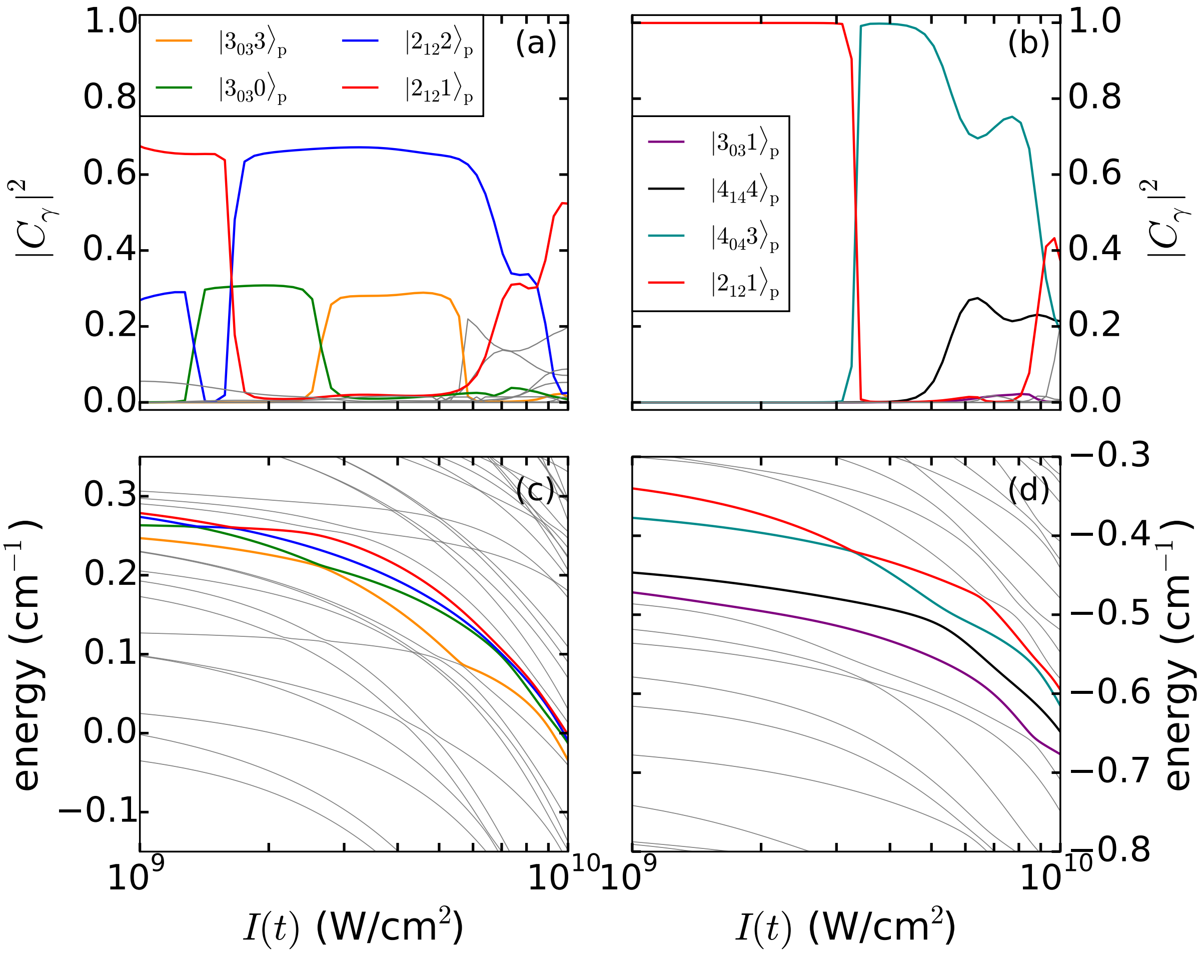

Figure 3.10.: The squares of the projection of the time-dependent wave function onto the adiabatic-pendular-state basis of the state $|2_{12}1\rangle_\mathrm{t}$, for an elliptically polarized ac field through the field-strength regime 1.0×10^9 W/cm$^2 \leq I(t) \leq 1.0 \times 10^{10}$ W/cm^2 and dc field strengths of (a) $\mathbf{E}_\mathrm{stat} = 571$ V/cm and (b) $\mathbf{E}_\mathrm{stat} = 20$ kV/cm. Energy level structure for the same intensities and dc field strengths (c) $\mathbf{E}_\mathrm{stat} = 571$ V/cm and (d) $\mathbf{E}_\mathrm{stat} = 20$ kV/cm. The angle between the ac and dc fields is $\beta = 57.1\,°$.

number of avoided crossings in Figure 3.10 (c) and (d) dominate the rotational dynamics, which involves several adiabatic pendular states even for low intensities. Differences between the dynamics for linearly and elliptically polarized ac fields gain importance at higher intensities where the elliptically polarized ac field significantly influences the energy level structure and the directional features of the adiabatic pendular states.

Analogously to the linearly polarized ac field, near-degenerate pendular doublets are formed as the laser intensity increases. For $\mathbf{E}_\mathrm{stat} = 571$ V/cm and $I(t) \gtrsim 10^{11}$ W/cm^2, we additionally encounter the formation of near-degenerate quadruplets, after the doublets are already formed. This arrangement in doublets and quadruplets can be observed in the energies of the adiabatic pendular states at the peak intensity, shown in Figure 3.8 (b). The energy separations between consecutive quadruplets are larger than between consecutive doublets in the case of a linearly polarized ac field. Due to the quadruplet formation for the elliptically polarized laser field, we find a smaller number of avoided crossings between near-degenerate groups of pendular states than for linear polarization. These features

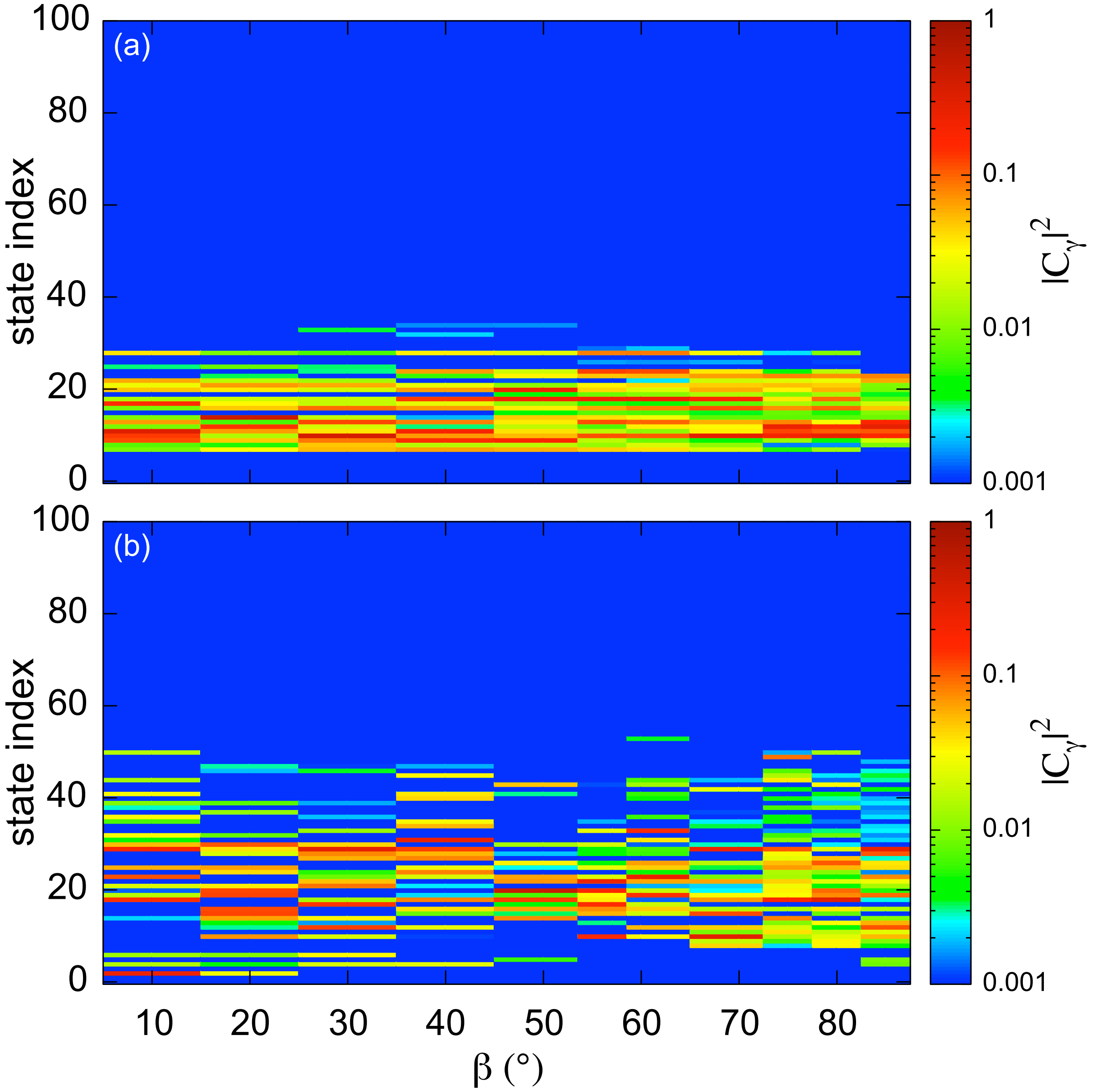

Figure 3.11.: For the state $|2_{12}1\rangle_\mathrm{t}$, the squares of the projection of the wave function at the peak of a elliptically polarized laser pulse onto the adiabatic pendular states as a function of β and the index of the pendular states according to energetic order. The dc field strength is (a) $\mathbf{E}_\mathrm{stat} = 571$ V/cm and (b) $\mathbf{E}_\mathrm{stat} = 20$ kV/cm. The index of the adiabatic pendular state $|2_{12}1\rangle_\mathrm{p}$ is 14 and 19 for the weak and strong dc field, respectively.

of the energy level structure limit the population transfer to highly excited states and the population at the peak intensity is confined to a small region of relatively low-lying adiabatic pendular states for all values of β, cf. Figure 3.11 (a) and section 3.6.

For the weak dc field and β close to $90\,^\circ$, a redistribution of the population occurs during the formation of the near-degenerate doublets similar to the case of a linearly polarized ac field (see section 3.6). This is reflected in the weights of the adiabatic pendular states contributing to the time-dependent wave function at the peak intensity, cf. Figure 3.11 (a), where there are several neighboring adiabatic levels with similar contributions. This redistribution leads to the decrease of $\langle\cos\theta_{Zz}\rangle$ for $\beta \gtrsim 75\,^\circ$ for the state $|2_{12}1\rangle_\mathrm{t}$ in Figure 3.6 (a) and the thermal ensemble in Figure 3.3 (a), similar to the case of a linearly polarized laser pulse. For $\beta = 85\,^\circ$, the states forming each of the two doublets in a near-degenerate quadruplet are oriented in opposite directions along the LFF Z-axis, but in the same direction along the Y-axis (see section 3.6). Thus, the state $|2_{12}1\rangle_\mathrm{t}$ shows a moderate orientation along the Y-axis at this angle see Figure 3.6 (b). We find other time-dependent excited states that are antioriented at the peak intensity due to different adiabatic pendular states contributing to their rotational dynamics. In the thermal ensemble, the contributions of states, which are oriented along the Y-axis, become more dominant as β approaches $90\,^\circ$, giving rise to the increase of $\langle\cos\theta_{Yy}\rangle$ for increasing β in Figure 3.3 (b).

For a strong dc electric field, pendular doublets can be observed for β close to $90\,^\circ$ and some low-lying pendular states for small β. Near-degenerate quadruplets are not formed, see Figure 3.8 (d). Thus, avoided crossings are the main source of non-adiabatic phenomena in the rotational dynamics at higher intensities.

For $\beta = 10\,^\circ$, a qualitatively similar rotational dynamics can be observed for both, linear and elliptical, polarizations of the ac field, but with different adiabatic states contributing to the time-dependent wave functions (see section 3.6). The distributions of the population of adiabatic pendular states in the wave function at the peak intensity show the same features, i. e., the approximate number and range of contributing pendular states, in both cases, see Figure 3.11 (b) and Figure 3.9 (b). The state $|2_{12}1\rangle_\mathrm{t}$ also shows a significant orientation of the MFF z-axis along the LFF Z-axis at the peak intensity of the elliptically polarized ac field, see Figure 3.6 (a). However, since the weights of the adiabatic pendular states vary when the ac field polarization is changed, $\langle\cos\theta_{Zz}\rangle$ at $\beta = 10\,^\circ$ differs for the linearly and elliptically polarized laser pulses.

Regarding the orientation along the LFF Y-axis for the strong dc field and the elliptically polarized ac field, the state $|2_{12}1\rangle_\mathrm{t}$ shows an analogous behavior for $\beta = 85\,^\circ$ as for the orientation along the LFF Z-axis for $\beta = 10\,^\circ$. Once the ac field component along the LFF Y-axis is sufficiently strong to align the MFF y-axis along the LFF Y-axis, the initially brute-force-oriented adiabatic pendular states become either strongly oriented or strongly antioriented along this axis (see section 3.6). As this occurs, several pendular states becoming antioriented along the Y-axis have significant weights in the time-dependent wave function. As a result, the state $|2_{12}1\rangle_\mathrm{t}$ only shows a moderate orientation of the MFF y-axis along the LFF Y-axis at the peak intensity, cf. Figure 3.6 (b). Other excited states may even be weakly antioriented. Thus, for the thermal ensemble,

$\langle\cos\theta_{Yy}\rangle_T$ in Figure 3.3 (b) is only moderately enhanced by the strong dc field.

To summarize, even if the field-dressed dynamics is highly non-adiabatic, the directional features of individual excited rotational states and, consequently, of the ensemble average, can be controlled to some extend. A significant orientation of the MFF z-axis along the LFF Z-axis can be achieved by applying a strong dc field for small values of β and both a linearly and elliptically polarized laser field. An analogous enhancement of the orientation of the MFF y-axis along the LFF Y-axis is obtained for an elliptically polarized ac field and β close to $90\,^\circ$.

3.5. Conclusion

We present a time-dependent analysis of the rotational dynamics of a non-symmetric molecule in combined ac and dc electric fields. We investigate the influence of the dc field strength and the angle between the ac and dc fields during the turn-on of linearly and elliptically polarized laser pulses. Our theoretical study is focused on the prototypical CPC molecule, which has a permanent dipole moment with a direction that is neither parallel to any principle axis of inertia nor to any principle axis of polarizability.

Our computational results for a thermal ensemble at 200 mK agree quantitatively with mixed-field-orientation experiments of state-selected CPC molecules [54], including the 1D orientation along the Z-axis, and the smooth β-dependence of the orientation that could not be explained by the previous adiabatic description. Our time-dependent description also shows that in the experiment 3D orientation was achieved for the employed combination of the elliptically polarized laser pulse and the weak dc field.

The analysis of the time-dependent dynamics of individual states, which we described for the prototypical state $|2_{12}1\rangle_\mathrm{t}$, shows highly non-adiabatic dynamics. These non-adiabaticities arise due to avoided crossings, M-manifold splitting, and the formation of pendular doublets and quadruplets. The relevance of these phenomena and the exact dynamics are highly dependent on the field parameters, e. g., the laser pulse, the dc field strength, and the angle between the two fields. Generally, the distribution of population over many adiabatic pendular states leads to a weak net orientation, because *a priori* as many oriented as antioriented pendular states are involved in the field-dressed dynamics. However, for strong dc electric fields, preferred contributions of oriented pendular states to the wave function are obtained and strong degrees of orientation are achieved even for rotationally excited states.

For a ground-state ensemble, which for complex molecules can be produced by state-specific guiding [126], adiabatic 3D orientation can be achieved by combining a long laser pulse with a moderately strong dc electric field. For excited states, although the dynamics is non-adiabatic, their directional features can be controlled to some degree by applying strong dc fields. Furthermore, we show that 3D orientation of a thermal ensemble can be achieved in two ways: Firstly, by combining a linearly polarized laser field with a strong dc electric field, effectively locking the MPA to the laser polarization axis and the EDM to the dc electric field direction. Secondly, by combining an elliptically polarized laser field with a strong dc electric field to induce mixed-field orientation of the

3D aligned sample.

While the current work is focused on the prototypical complex molecule CPC, similar rotational dynamics are expected for other non-symmetric molecules. Even if the principle axes of inertia and polarizability are non-parallel, mixed-field orientation is expected. Since the non-adiabatic effects strongly depend on the molecular properties, accurate predictions of the results of mixed-field experiments requires an accurate description, e.g., a TDSE analysis of the rotational dynamics. The present work paves the way to an accurate description of the mixed-field orientation of large molecules in general, which is highly relevant for molecular-frame imaging experiments of complex molecules, where experimental determinations of the degree of alignment and orientation become very difficult and corresponding simulations of the angular control are necessary to analyze the experimental data [14, 70].

3.6. Supplementary Material

See supplementary material of Ref. [127] for movies of the field-dressed rotational dynamics of the state $|2_{12}1\rangle_{\mathrm{t}}$ and the orientation cosines of the adiabatic pendular states.

4 Laser-induced alignment of weakly-bound molecular aggregates[4]

4.1. Introduction

Biological function is strongly shaped by the intricate interaction of the molecules with their aqueous environment. Unraveling the underlying (bio)molecule-water solvation interactions as well as their relevance for chemical dynamics promises a detailed understanding of their contributions to function. Approaching this through studies of the elementary chemical processes as intrinsic properties in well-defined molecular aggregates enables the definition of fundamental building blocks as a dynamical basis of intermolecular solute-solvent interactions and their chemical dynamics. This rationalizes the longstanding history of detailed studies of molecule-solvent clusters in the gas phase [128, 129].

Novel imaging techniques with highest spatiotemporal resolution, such as ultrafast x-ray [17, 130] or electron diffraction [11, 131], photoelectron imaging [2–4], and laser-induced electron diffraction [12] will provide a new level of detail to these investigations and promise to allow for the recording of molecular movies of the dynamical interactions. The applicability of these imaging methods to complex molecular systems relies on the preparation of pure samples [70, 71] and benefits tremendously from fixing the molecules in space [14, 20, 70, 132], i. e., to align or orient them [48, 61, 72, 121]. Recently, some of us have demonstrated the preparation of pure beams of the prototypical indole-water dimer cluster as well as its laser alignment [102, 103, 133].

However, it is not clear in how far the very floppy structure of weakly bound molecular clusters modifies or hinders the control techniques, especially regarding alignment with strong laser fields. It is well understood that internal rotation, or torsions, and overall rotation are coupled [106] and that internal rotations can also be controlled with the same strong laser fields [82]. So far, experimental and theoretical studies have been limited to highly symmetric molecular systems [81–85], e. g., with G_{16} symmetry, such as biphenyls. It is *a priori* not clear how these effects will transfer to complex "real world" (bio)molecules and their complexes.

Here, we set out to analyze the laser alignment and the corresponding influence of internal rotations to the overall rotational dynamics of molecule-solvent systems, which, generally, have lower symmetries and asymmetric shapes of the constituents. Specifically,

---

[4] This chapter is based on the publication: *Laser-induced alignment of weakly-bound molecular aggregates*, Linda V. Thesing, Andrey Yachmenev, Rosario González-Férez and Jochen Küpper, Phys. Rev. A **98**, 053412 (2018), arXiv:1808.01206 [physics]. I contributed to the development of the computational code for the energy levels and rotation-torsional dynamics. Furthermore, I contributed to the *ab initio* calculations and performed the calculations of the molecular energy levels, matrix elements as well as alignment/orientation, analyzed the data and contributed to writing the manuscript.

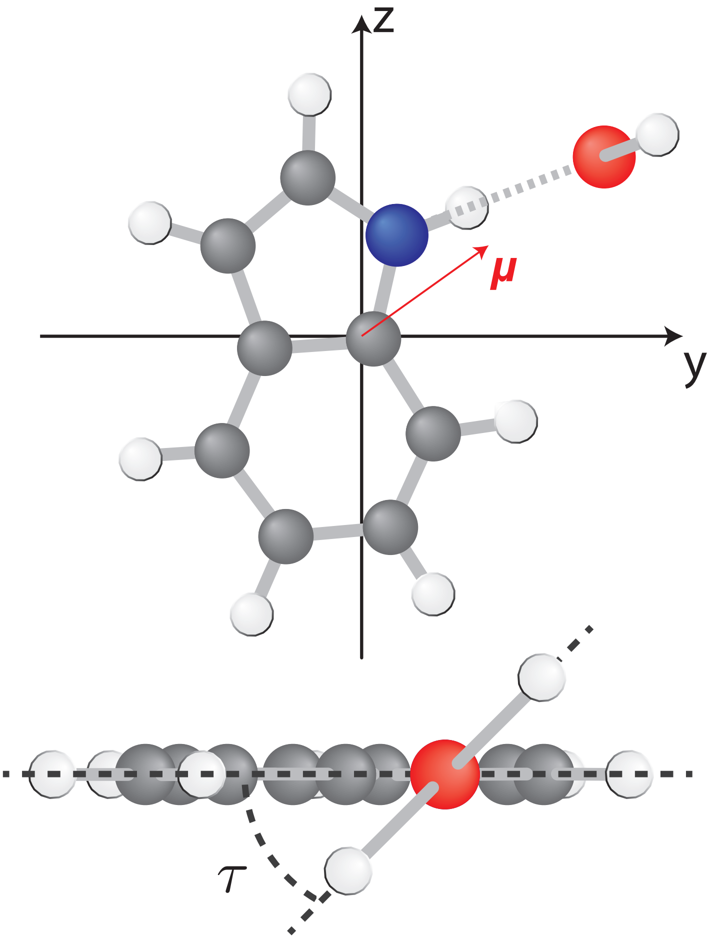

Figure 4.1.: Sketch of the indole(H_2O) dimer cluster. The most polarizable axis defines the z-axis of the molecular frame. The torsional angle is defined as the dihedral angle between the indole and water planes. For the experimentally determined structure, see Ref. 77.

we start these investigations with a theoretical analysis of the laser alignment of the prototypical indole-water dimer systems [76, 77, 134, 135], which we treat as a semirigid-rotor with an additional one-dimensional internal rotation coordinate corresponding to the rotation of the water moiety about its b-axis; see Figure 4.1. We utilize a reduced-mode variational approach based on the general-molecule variational approach [114, 136, 137] combined with a general treatment of electric fields [115].

4.2. Theory and computational setup

The model structure of indole(H_2O) that is employed in this work is schematically shown in Figure 4.1. The water molecule is attached to the planar indole frame *via* a hydrogen bond where the oxygen atom of the water molecule lies in the indole plane. We treat the indole(H_2O) cluster as a floppy molecule with the water molecule undergoing an internal rotation. The angle of internal rotation τ is defined as the dihedral angle between the indole and the water planes (see Figure 4.1), with $\tau = 90\,^\circ$ in the equilibrium configuration [77]. We keep all other vibrational coordinates fixed at their equilibrium values along the minimum-energy path (MEP) of the internal rotation. The MEP is determined by optimizing the structural parameters of the indole(H_2O) complex at different values of the τ coordinate between $0\,^\circ$ and $360\,^\circ$.

We assume the Born-Oppenheimer approximation and consider four degrees of freedom, three Euler angles (ϕ, θ, χ) describing the overall rotation of the system, and the angle τ associated with the internal rotation of the water molecule. The field-free Hamiltonian of the system is

$$\begin{aligned} H_0 = &+\frac{1}{2}\sum_{\alpha,\beta=x,y,z}\hat{J}_\alpha G^{\mathrm{rot}}_{\alpha\beta}(\tau)\hat{J}_\beta + \frac{1}{2}p_\tau G^{\mathrm{tor}}_{\tau}(\tau)p_\tau \\ &+\frac{1}{2}\sum_{\alpha=x,y,z}\left[p_\tau G^{\mathrm{cor}}_{\tau\alpha}(\tau)\hat{J}_\alpha + \hat{J}_\alpha G^{\mathrm{cor}}_{\alpha\tau}(\tau)p_\tau\right] + V(\tau), \end{aligned} \tag{4.1}$$

where $\hat{J}_\alpha$ are components of the rotational angular momentum operator in the molecule-fixed frame (MFF) and $p_\tau = -i\hbar\partial/\partial\tau$. The kinetic-energy matrices $G^{\mathrm{tor}}_{\tau}(\tau)$ and $G^{\mathrm{rot}}_{\alpha\beta}(\tau)$ are associated with the internal torsional and overall rotational motions, $G^{\mathrm{cor}}_{\tau\alpha}(\tau)$ describes coupling between the two motions, and $V(\tau)$ is the potential-energy function. The elements of the kinetic-energy matrices are calculated as functions of the torsional coordinate τ following the generalized procedure from TROVE [110, 114]. The kinetic-energy matrices and potential energy function in (4.1) were built along the MEP. The geometry optimizations were carried out using the density-fitted second-order Møller-Plesset perturbation theory DF-MP2 in the frozen-core approximation, in conjunction with the augmented correlation-consistent basis set aug-cc-pVTZ [138, 139]. For the density-fitting approximation, we utilized the JKFIT [140] and MP2FIT [141] auxiliary basis sets specifically matched to aug-cc-pVTZ. All electronic-structure calculations were carried out using Psi4 [142]. The *ab initio* potential-energy surface (PES) is represented by an analytical function by fitting the expression

$$V(\tau) = \sum_{n=0}^{2} V_{2n}\cos(2n\tau)\ . \tag{4.2}$$

The PES is depicted in Figure 4.2 (a) and the coefficients are $V_0 = -101.950\ \mathrm{cm}^{-1}$, $V_2 = 106.006\ \mathrm{cm}^{-1}$ and $V_4 = -3.58143\ \mathrm{cm}^{-1}$, in good agreement with the experimental value for this motion of $V_2 = 99\ \mathrm{cm}^{-1}$ [77]. The structural parameters are represented by similar analytical functions; see section 4.5.

Our analysis is restricted to a nonresonant linearly polarized laser ac electric field combined with a parallel weak dc electric field. The interaction of the polarizability with the weak dc field is neglected. In addition, we can average over the rapid oscillations of the nonresonant ac field and the interaction of the electric-dipole moment with the laser field vanishes. The interaction of the molecule with the external electric fields then reads

$$H_{\mathrm{int}}(t) = -\boldsymbol{\mu}(\tau)\cdot\mathbf{E}_{\mathrm{stat}} - \frac{1}{4}\mathbf{E}_{\mathrm{laser}}(t)\underline{\underline{\alpha}}(\tau)\mathbf{E}_{\mathrm{laser}}(t)\ , \tag{4.3}$$

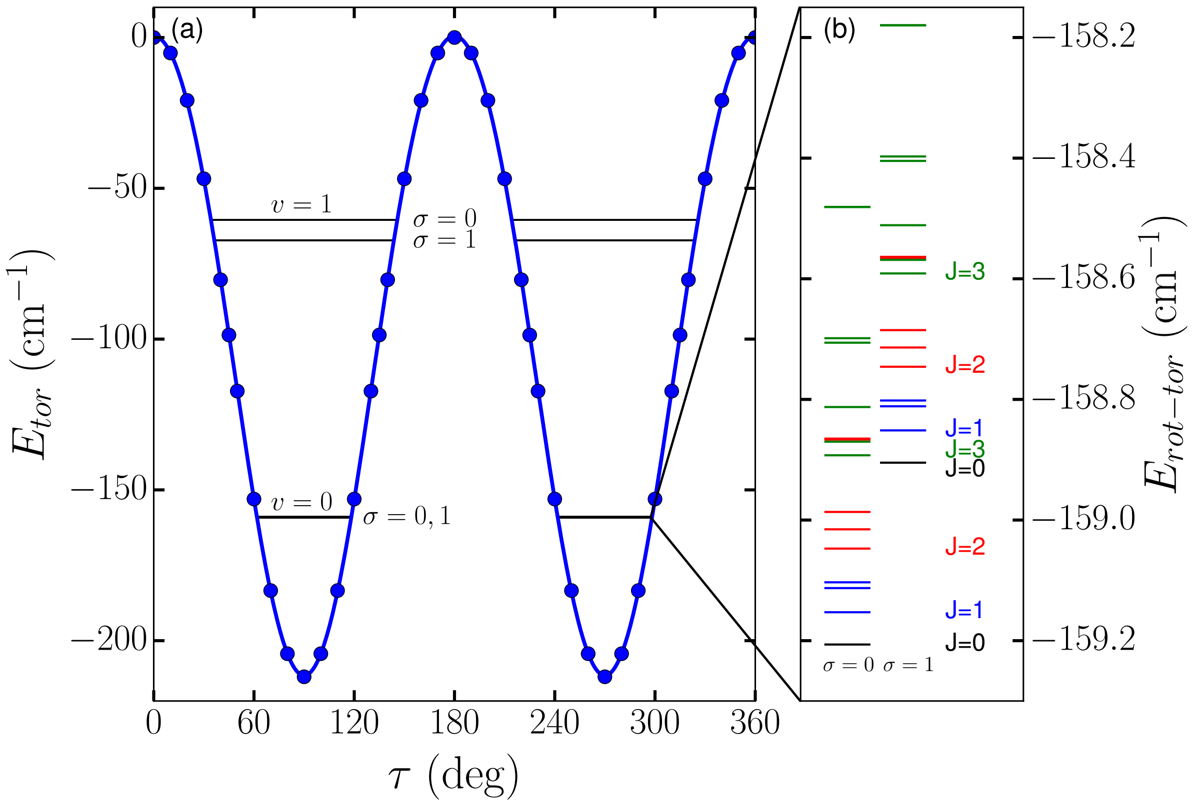

Figure 4.2.: (a) The *ab initio* 1D potential-energy surface (blue circles) and corresponding fit (blue line) and the lowest two field-free torsional energy levels of indole(H_2O), obtained from the pure torsional part of the Hamiltonian (4.1). Each torsional level, denoted by the vibrational quantum number v, is split into two sublevels $\sigma = 0, 1$ of opposite parity. (b) Field-free rotation-torsional energy levels for $J = 0, \ldots, 3$ corresponding to the torsional ground state, obtained from the Hamiltonian (4.1). Due to the small coupling between the internal and overall rotation, the energy levels are approximately given by the sum of the pure torsional and pure rotational energies. Thus, for each J, there are $2J + 1$ rotational energy levels in a given torsional sublevel; see text for more details.

where $\mathbf{E}_{\text{stat}}$ is the static electric field and $\mathbf{E}_{\text{laser}}(t)$ is the envelope of the laser electric field. The electric-dipole moment (EDM) $\boldsymbol{\mu}(\tau)$ and the polarizability tensor $\underline{\underline{\alpha}}(\tau)$ of indole(H_2O) are calculated along the minimum-energy path created by varying the τ coordinate; see section 4.5. They are represented by analytical functions similar to the ones used for the PES; see section 4.5. The polarization axis of the laser is chosen as the Z-axis of the laboratory fixed frame (LFF). The molecule-fixed frame (x, y, z) is defined by the principle axes of polarizability at the equilibrium configuration so that the diagonal elements fulfill $\alpha_{xx} < \alpha_{yy} < \alpha_{zz}$.

To study the rotational dynamics of indole(H_2O), we solve the time-dependent Schrödinger equation (TDSE) for the full Hamiltonian

$$H(t) = H_0 + H_{\text{int}}(t) \;, \tag{4.4}$$

using the short iterative Lanczos method [118, 119] for the time propagation and a basis-set expansion for the spatial coordinates using the eigenstates of the field-free Hamiltonian (4.1). The field-free eigenbasis is calculated variationally in several steps. First, the pure rotational and torsional basis functions, $\Psi_l^{rot}(\phi, \theta, \chi)$ and $\Psi_l^{tor}(\tau)$, are constructed by diagonalizing the respective parts of the field-free Hamiltonian (4.1). In this step, we use Wang states [109], i. e., symmetrized combinations of symmetric-top functions, as a basis set for the rotational coordinates. For the torsional coordinates, we use sine and cosine functions $\phi_n^{\text{even}}(\tau) = \cos(n\tau)/\sqrt{\pi}$ and $\phi_n^{\text{odd}}(\tau) = \sin(n\tau)/\sqrt{\pi}$, $n > 0$, and $\phi_0^{\text{even}}(\tau) = 1/\sqrt{2\pi}$ to preserve the even and odd symmetry of the states. The matrix elements of the full Hamiltonian (4.4) are then set up in the product basis $\Psi_l^{rot}(\phi, \theta, \chi)\Psi_m^{tor}(\tau)$ and transformed to the eigenbasis of the complete field-free Hamiltonian (4.1) following the generalized approach developed in RichMol [115].

To analyze the importance of the internal motion of the water molecule, we compare our results to calculations using the rigid-rotor approximation [124], i. e., considering only the three degrees of freedom of the overall rotation in (4.1). For the rigid-rotor calculations, we use the structural parameters, EDM, and polarizability tensor at the equilibrium configuration, i. e., $\tau = 90\,^\circ$.

4.3. Results and Discussion

In this section, we analyze the overall rotational and torsional dynamics of indole(H_2O). We solve the TDSE using the field-free ground state as the initial state of the time-propagation, i. e., $T = 0$ K. For the laser pulse, we consider a Gaussian envelope $\mathbf{E}_{\text{laser}}(t) = \hat{\mathbf{e}}_Z \mathrm{E}_0 \exp\left(-4\ln 2 t^2/\tau_{\text{FWHM}}^2\right)$ with $\mathrm{E}_0 = 2.74 \times 10^7$ V/cm and $\tau_{\text{FWHM}} = 1$ ns. The parallel static electric field is increased to a field strength of $\mathbf{E}_{\text{stat}} = 600$ V/cm slowly enough to ensure adiabatic behavior before the laser field is applied. We analyze the alignment and mixed-field-orientation dynamics of indole(H_2O), quantified by the expectation values $\left\langle\cos^2\theta\right\rangle$ and $\langle\cos\theta\rangle$, respectively, as well as the torsional alignment $\left\langle\cos^2\tau\right\rangle$.

Figure 4.3 (a) and (b) show the time evolution of the alignment and orientation of the

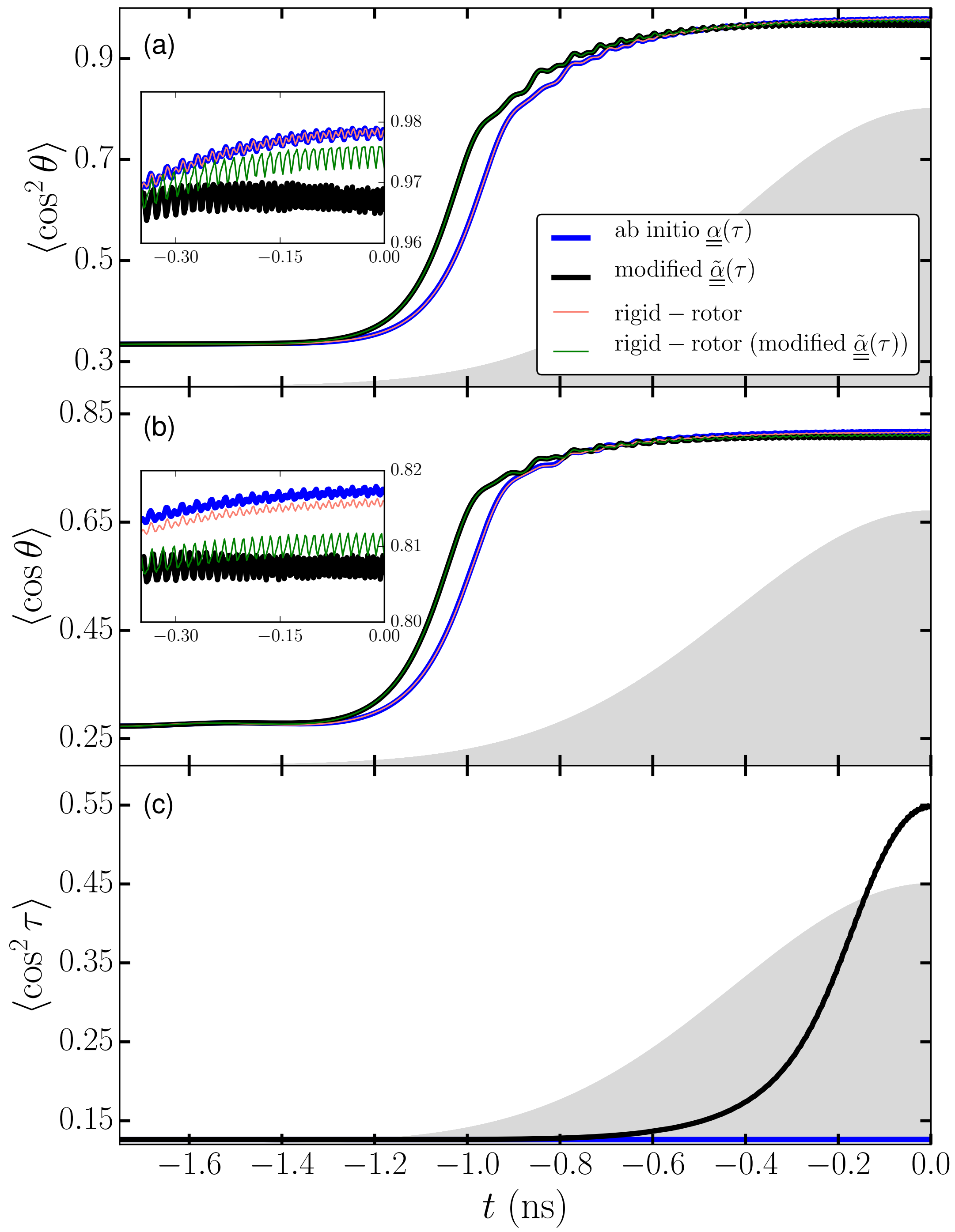

Figure 4.3.: For the ground state of indole(H_2O) ($T = 0$ K), the time evolution of the expectation values (a) $\langle\cos^2\theta\rangle$, (b) $\langle\cos\theta\rangle$ and (c) $\langle\cos^2\tau\rangle$ using $\underline{\underline{\alpha}}(\tau)$ from *ab initio* calculations [thick blue (dark gray) lines] and the modified $\underline{\underline{\tilde{\alpha}}}(\tau)$ (thick black lines). For comparison, results using the rigid-rotor approximation for the two polarizabilities are shown [thin red (light gray) lines and thin green (gray) lines, respectively]. The results for the *ab initio* polarizability $\underline{\underline{\alpha}}(\tau)$ and the rigid-rotor approximation in (a) and (b) are practically indistinguishable. The smallest values of $\langle\cos^2\theta\rangle$ and $\langle\cos\theta\rangle$ and the largest value of $\langle\cos^2\tau\rangle$ at the peak intensity are obtained for the modified polarizability $\underline{\underline{\tilde{\alpha}}}(\tau)$. The result for the modified polarizability differs from the corresponding rigid-rotor result at the peak intensity. The insets in (a) and (b) show a zoom of $\langle\cos^2\theta\rangle$ and $\langle\cos\theta\rangle$ close to the peak intensity. The gray area illustrates the envelope of the laser field with $E_0 = 2.74 \times 10^7$ V/cm. The static field strength is $\mathbf{E}_{\text{stat}} = 600$ V/cm.

ground state of indole(H_2O) obtained using the nonrigid rotation-torsional Hamiltonian [thick blue (dark gray) lines] as well as the results using the rigid-rotor approximation [thin red (light gray) lines]. As the laser-field strength rises, the most polarizable axis (MPA) becomes strongly aligned along the polarization axis of the laser, reaching $\left\langle\cos^2\theta\right\rangle = 0.98$ at the peak intensity. For both the rigid and the nonrigid models, we observe a typical mixed-field-orientation dynamics that has previously been described for other linear and asymmetric top molecules [55, 57, 122, 123]. Due to the presence of the static electric field, the orientation increases as laser-aligned pendular states are formed and increasingly coupled with increasing laser-field strength. The orientation at the peak intensity, $\langle\cos\theta\rangle = 0.82$, is lower than the value obtained in the adiabatic description, $\langle\cos\theta\rangle = 0.99$, indicating a nonadiabatic dynamics, i. e., several field-dressed eigenstates of the instantaneous Hamiltonian (4.4) contribute to the time-dependent wave function [56, 124, 127].

We point out that the results obtained for the rigid and non-rigid descriptions are practically identical, which shows that the indole(H_2O) cluster can be treated as a rigid molecule for moderate electric-field strengths that are typically employed in molecular alignment and mixed-field-orientation experiments. To understand why the internal rotation of the water molecule does not influence the overall rotational dynamics, we look at the coupling between the internal and overall rotations and the resulting rotation-torsional energy levels. In the field-free case, the coupling of the two motions is described by the off-diagonal blocks $G^{\text{cor}}_{\tau\alpha}(\tau)$ of the kinetic-energy matrix and the dependence of $G^{\text{rot}}_{\alpha\beta}(\tau)$ on the torsional angle τ in (4.1). Since this field-free coupling is very small [77], the eigenstates of the Hamiltonian (4.1) are approximately described by the product states $\Psi^{rot}_{l}(\phi,\theta,\chi)\Psi^{tor}_{m}(\tau)$, and the energy levels are given approximately by the sum of the pure rotational and torsional energies, Figure 4.2, even for large values of the quantum number J. Due to tunneling, each torsional level splits into two sublevels, denoted by $\sigma = 0, 1$ in Figure 4.2 (a). The energy difference between two consecutive torsional states is three orders of magnitude larger than the energy gaps between pure rotational states. As a result, the rotation-torsional energy levels are distributed as bands of rotational states for each torsional sublevel, see Figure 4.2 (b).

In the presence of external electric fields, the internal and overall rotations are additionally coupled due to the dependence of the EDM and the polarizability on the torsional angle [see (4.3)], which is weak for indole(H_2O). Thus, for the ac and dc field strengths considered here, the field-induced coupling between the torsional ground and first-excited state $\left\langle\Psi^{rot-tor}_{i,v=0}\left|H_{\text{int}}\right|\Psi^{rot-tor}_{j,v=1}\right\rangle$, where $v = 0, 1$ indicates the torsional ground and excited state, respectively, is small (< 1 cm^{-1}) compared to the energy gap $\Delta E \approx 98$ cm^{-1} between these torsional levels. Due to the symmetry of the EDM and the polarizability, the two sublevels $\sigma = 0, 1$ of a torsional state are not coupled by the external electric fields; see section 4.5. As a consequence, the field-dressed rotation-torsional wavepacket is dominated by the torsional ground state. The torsional alignment shown in Figure 4.3 (c) [thick blue (dark gray) lines] thus remains constant with $\left\langle\cos^2\tau\right\rangle = 0.126$. To achieve a field-induced coupling that is strong enough to overcome the energy gap between the torsional ground and first-excited state, laser-field

n	$\tilde{\alpha}_n^{(11)}$ (a. u.)	$\tilde{\alpha}_n^{(13)}$ (a. u.)	$\tilde{\alpha}_n^{(22)}$ (a. u.)	$\tilde{\alpha}_n^{(33)}$ (a. u.)
0	98.8163	56.5324	-9.156292	193.5136
1	-23.5024	49.02866	-77.91074	47.57616

Table 4.1.: Coefficients of the analytical functions (4.7) used to fit the modified polarizability. The components α_{12} and α_{23} are zero.

strengths larger than $E_0 \approx 10^8$ V/cm, i. e., intensities $I_{\text{control}} > 10^{13}$ W/cm^2, would be necessary. Such fields would, however, affect the electronic structure and induce ionization of indole(H_2O) and are generally not used to control the rotational dynamics of these clusters [103].

In the following, we investigate for which regimes of field-free and field-induced couplings the rigid-rotor approximation can still be applied to describe the rotational dynamics. To obtain a large field-induced coupling, stronger external ac and dc electric fields could be applied or the dependence of the EDM and the polarizability on the torsional angle τ could be, artificially, increased. We begin by studying a molecular cluster that has a modified polarizability $\underline{\underline{\tilde{\alpha}}}(\tau)$ and is otherwise identical to indole(H_2O). Since the interaction with the weak static electric field is much weaker than the one with the laser field, we do not modify the EDM. We set $\tilde{\alpha}_{pq}(\tau)$ including only terms with $n \leq 1$ (see section 4.5) and with the coefficients listed in Table 4.1. The coefficients $\tilde{\alpha}_2^{(pq)}$ are chosen to be 200 times larger than the largest ones obtained from fits to the *ab inito* results. The chosen $\tilde{\alpha}_0^{(pq)}$ satisfy $\underline{\underline{\tilde{\alpha}}}(\tau = 90\,°) = \underline{\underline{\alpha}}(\tau = 90\,°)$. This polarizability increases the field-induced coupling by a similar magnitude as increasing the laser-field strength by a factor of $\sqrt{200}$. We carry out an additional rigid-rotor calculation using the structural parameters and EDM at the equilibrium configuration, but the expectation values $\left\langle \tilde{\alpha}_{pq} \right\rangle = \left\langle \Psi_0^{tor} \left| \tilde{\alpha}_{pq}(\tau) \right| \Psi_0^{tor} \right\rangle$ in the torsional ground state as these values differ significantly from $\tilde{\alpha}_{pq}(\tau = 90\,°)$. We point out that the expectation value of the modified polarizability is not diagonal in the chosen MFF, i. e., the MPA of the modified polarizability is not parallel to the MFF z-axis.

The results for this enhanced-response molecular system are depicted in Figure 4.3 for the nonrigid-rotor (black lines) and rigid-rotor [thin green (gray) lines] cases. At lower laser-field strengths, the alignment does not differ from the results obtained using the rigid-rotor approximation. Close to the peak intensity, the alignment starts to decrease and reaches a value of $\left\langle \cos^2\theta \right\rangle$ =0.965, slightly smaller than the rigid-rotor result $\left\langle \cos^2\theta \right\rangle$ =0.972. Simultaneously, the orientation starts to differ slightly from the rigid-rotor result reaching a smaller value at the peak intensity. Regarding the torsional alignment, we observe an increase of $\left\langle \cos^2\tau \right\rangle$ with increasing laser-field strength, due to the contribution of excited torsional states, in particular the second-excited state $v = 2, \sigma = 0$. The reason for this is that due to the symmetry of the polarizability, the coupling between the field-free rotation-torsional states with different torsional symmetry is small [74, 102]; see section 4.5. The difference between the nonrigid and the rigid-rotor descriptions can be understood in terms of the effective polarizability $\left\langle \Psi_m^{tor} \left| \underline{\underline{\tilde{\alpha}}}(\tau) \right| \Psi_m^{tor} \right\rangle$ of the torsional states. For weak laser fields, excited torsional states are not involved in the dynamics.

As a consequence, the alignment and orientation evolve in a similar way as for the rigid indole(H_2O). The torsional ground-state wave function is localized around $\tau = 90\,^\circ$, yielding a polarizability with small off-diagonal elements $\langle\tilde{\alpha}_{13}\rangle = \langle\tilde{\alpha}_{31}\rangle = 5.2$ a. u.; $\tilde{\alpha}_{13}(\tau = 90\,^\circ) = 0$. At stronger laser fields, the contributions of excited torsional states modify the polarizability, with $\langle\tilde{\alpha}_{13}\rangle = 23.5$ a. u. at the peak intensity. As a result, a different molecular axis is aligned compared to the rigid-rotor case and $\left\langle\cos^2\theta\right\rangle$ decreases. In addition to the change in the MPA, the anisotropy of the polarizability increases with increasing laser field strength. The alignment of the MPA $\left\langle\cos^2\theta_{\text{MPA}}\right\rangle$, where θ_{MPA} is the angle between the MPA and the LFF Z-axis, is thus larger at the peak intensity than for the rigid-rotor case. As a result of the change in the MPA, the orientation $\langle\cos\theta\rangle$ in Figure 4.3 (b) also decreases, but a larger orientation of the MPA $\langle\cos\theta_{\text{MPA}}\rangle$ is obtained for the non-rigid than for the rigid case.

Additionally modifying the EDM in an analogous way results in different effective dipole moments $\langle\boldsymbol{\mu}\rangle$ and a correspondingly changed degree of orientation compared to the rigid-rotor result. However, since the interaction of the dc electric field with the dipole moment is comparably weak, no additional excitation of torsional states occurs. Increasing the laser field strength by the corresponding factor of $\sqrt{200}$ does not have the same impact on the rotational dynamics as the modified polarizability. While a stronger laser field leads to contributions of excited torsional states, the expectation value of the polarizability in these excited states does not differ much from the one in the torsional ground state. Thus, no significant change of the MPA or polarizability anisotropy occurs. Calculations performed for a laser-field strength of $\mathrm{E}_0 = 3 \times 10^8$ V/cm and $\mathbf{E}_{\text{stat}} = 0$ show a small increase in $\left\langle\cos^2\tau\right\rangle$ during the laser pulse, but no difference in the overall alignment $\left\langle\cos^2\theta\right\rangle$ between the rigid and non-rigid descriptions. Increasing the laser-field strength further was computationally too expensive.

In addition to analyzing the impact of a strong field-induced coupling, we investigate the influence of the barrier height. This affects the torsional energy-level structure [106] and may thus alter the field-dressed coupling necessary to achieve an excitation of the torsion in the presence of external fields. To this end, we use a modified torsional potential $\tilde{V}(\tau) = \tilde{V}_0(\cos(2\tau) - 1)$ with a very small barrier height $\tilde{V}_0 = 1.0\ \text{cm}^{-1}$. Using the same field parameters as in Figure 4.3 and the *ab initio* polarizability, we observe an overall rotational dynamics that is very similar to the dynamics obtained using the *ab initio* torsional potential. The reason for this is that by lowering the barrier height the energy gap between the torsional ground and second-excited level is only decreased to $\Delta E \approx 55\ \text{cm}^{-1}$, which is still large compared to the coupling induced by the external electric fields. Finally, we consider molecules with an internal rotor that has a smaller rotational constant. For a modified molecular system increasing the mass of the protons in the water molecule of indole(H_2O) to 14 u and keeping the *ab initio* polarizability, the rotational dynamics for the rigid and nonrigid descriptions are almost indistinguishable when applying the field configuration as in Figure 4.3. If we additionally consider a low torsional barrier with $\tilde{V}_0 = 1.0\ \text{cm}^{-1}$ (see above), the energy gap between the torsional ground state and second-excited state is lowered to $\Delta E \approx 4.5\ \text{cm}^{-1}$ and we observe contributions of excited torsional states. Here, the field-free rotation-torsional states belonging to the excited torsional levels cannot be approximated well as product states of pure rotational and torsional states. As a consequence, the orientation slightly differs from the rigid-rotor result with $\Delta\left\langle\cos\theta\right\rangle = 0.01$.

4.4. Summary and Conclusions

We investigate the rotational dynamics of a floppy molecule in combined laser and static electric fields. Our work is focused on the prototypical indole(H_2O) cluster where the attached water molecule undergoes an internal rotation. The molecular structure, electric-dipole moment, and polarizability are calculated with *ab initio* methods. We solve the time-dependent Schrödinger equation for a moderate laser-field strength and a weak dc electric field taking into account four degrees of freedom for the internal and overall rotation. We compare the obtained alignment and orientation dynamics to results computed within the rigid-rotor approximation. We demonstrate that indole(H_2O) can be treated as a rigid molecule in typical alignment and mixed-field-orientation experiments. This conclusion is rationalized by the weak field-free and field-induced couplings of the internal and overall motions compared to the respective energy spacings. We explore regimes of laser-field strengths for which the internal rotation of the water moiety can no longer be neglected. However, such strong laser pulses, $I_{\text{control}} > 10^{13}$ W/cm^2, are not likely to be used in alignment experiments as they would result in electronic excitation and ionization. Let us remark that even at a rotational temperature of $T = 0$ K, both torsional sublevels $\sigma = 0, 1$ of the rotational ground state would be populated in a molecular beam according to their nuclear spin statistical weights. However, as the rotational and torsional dynamics of these two sublevels in the presence of the ac and dc fields do not differ significantly, our analysis of the $\sigma = 0$ sublevel provides a good description of the overall rotational dynamics in the external fields.

We analyze the influence of a larger field-induced coupling on the overall and internal rotational dynamics by using artificially modified electric-dipole moment and polarizability with a two-orders-of-magnitude-stronger dependence on the torsional angle. We find a decrease of the overall alignment and orientation close to the peak intensity due to an effective change in the MPA in the excited torsional state. In addition, we observe an increase of the torsional alignment with increasing laser-field strength caused by the contributions of excited torsional states. In contrast, for unmodified indole(H_2O), a constant torsional alignment is found.

Based on these results for indole(H_2O), we conclude that similar molecular clusters can also be treated as rigid molecules. This conclusion can also be extended to other floppy molecular systems provided their dipole moment and polarizability depend only weakly on the internal motion and their rotational and torsional energy levels are approximately given by the sum of pure rotational and torsional energies with large gaps between consecutive torsional levels. For molecules with a small torsional barrier or a smaller internal rotational constant, e. g., for previously studied biphenyl-type molecules, a weaker field-induced coupling may already lead to contributions of excited torsional states to the field-dressed dynamics. However, the rigid-rotor approximation can still be employed for moderate laser-field strengths. This is different than for previously studied biphenyl-type molecules, which have their axis of internal rotation parallel to a principle axis of inertia and their MPA not modified by the torsion, which results in a qualitatively different coupled rotational and torsional dynamics than for generic low-symmetry molecular clusters, such as indole(H_2O). To achieve an accurate description of the rotational dynamics for molecules with small energy gaps between the torsional ground and excited states, the coupling of the internal and overall rotations cannot be neglected. Furthermore, for impulsive alignment, even the small coupling between the internal and overall rotation in indole(H_2O) becomes important on longer, e. g., nanosecond, timescales, since the revivals of the alignment are sensitive even to small energy shifts of the field-free rotational states in the wave packet.

The variational approach applied in this work allows one to extend our study to include multiple internal modes in a multidimensional PES and to study their effect on the field-dressed rotational dynamics, which will be investigated in the future.

4.5. Supplementary Material

Ab initio results

The *ab initio* results for the components of the EDM $\boldsymbol{\mu}(\tau)$ and polarizability $\underline{\underline{\alpha}}(\tau)$ are depicted in Figure 4.4 together with the analytical functions fitted to the *ab initio* results; see below. For each geometry obtained for a fixed value of the torsional angle, the EDM and polarizability are calculated as first and second derivatives of the electronic energy with respect to external electric fields along the corresponding axis. We use electric-field strengths of +0.005 a. u.. and −0.005 a. u., where 1 a. u.. = 5.14×10^9 V/cm. As for the geometry optimization, the DF-MP2 method and aug-cc-pVTZ basis set is used.

Analytical expressions for the structural parameters

The bond lengths r_i, angles a_i, and dihedral angles d_i of indole(H_2O) are defined in Z-matrix form according to Table 4.2, where $d_{18} = \tau$, $d_i = 0$ for $i \in \{4, 5, 7, 8, 9\}$ and $d_i = \pi$ for $i \in \{6, 10, 11, 12, 13, 14, 15, 16, 17, 19\}$. The coordinates r_i, $i \neq 18, 19$, and a_i, $i \neq 18$, are represented as analytical functions of the torsional angle similar to the potential-energy surface,

$$x_i = \sum_{n=0}^{3} x_{2n}^{(i)} \cos(2n\tau) \tag{4.5}$$

to preserve their symmetry. To obtain expressions for $r_{18} = r_{\mathrm{OH}_1}$, $r_{19} = r_{\mathrm{OH}_2}$, and $a_{18} = a_{\mathrm{NOH}_1}$, we fit symmetrized coordinates defined as $r_+ = (r_{18} + r_{19})/2$, $r_- = (r_{18} - r_{19})/2$, and $a_- = a_{18} + a_{19}/2 - \pi$, where $a_{19} = a_{\mathrm{HOH}}$. For r_+, the expression (4.5) is used and for r_- and a_-, we fit

$$x_i = \sum_{n=0}^{2} x_{2n+1}^{(i)} \cos((2n+1)\tau)\ . \tag{4.6}$$

Analytical expressions for the coordinates r_{18}, r_{19}, and a_{18} are then obtained from those

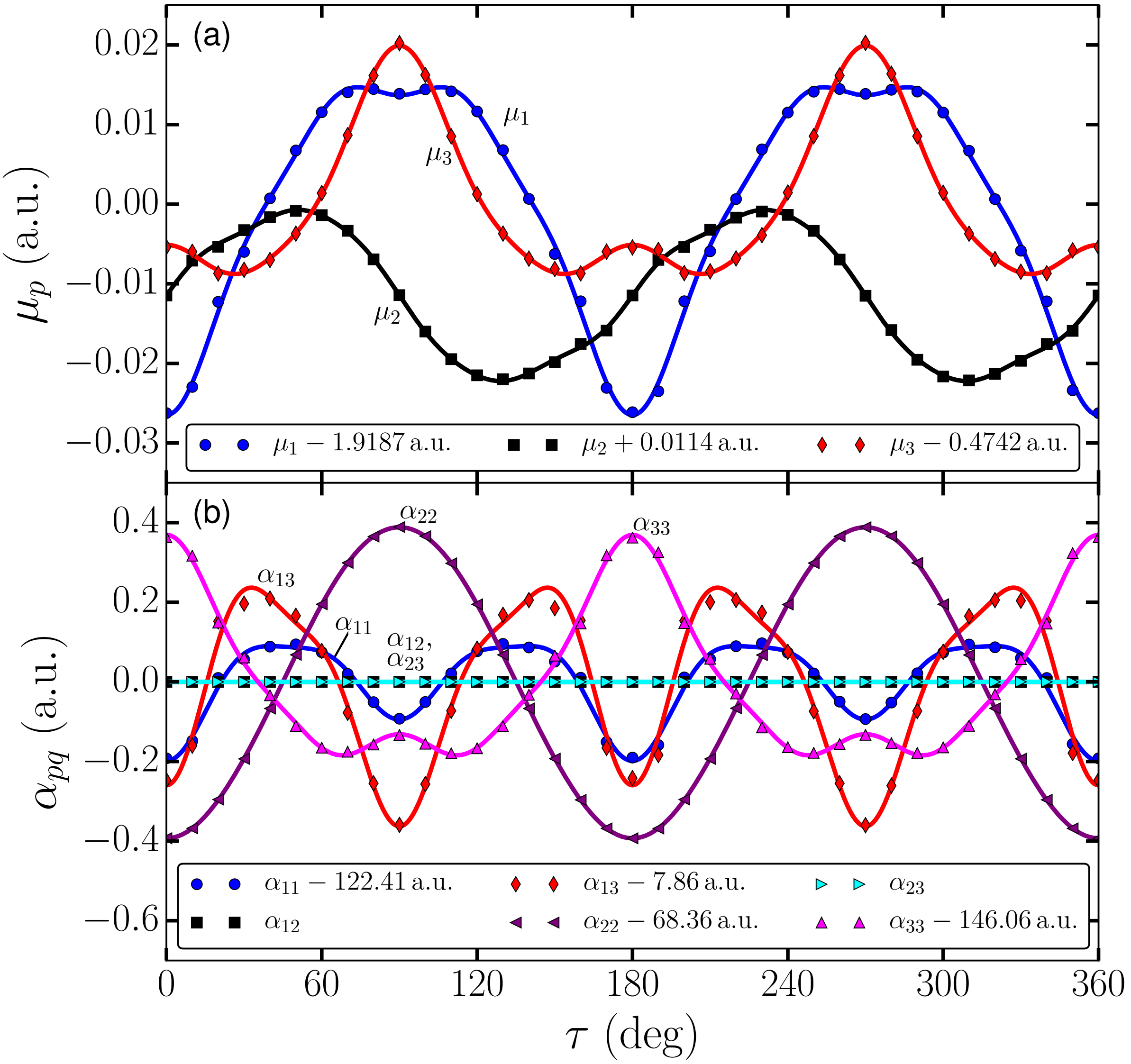

Figure 4.4.: The *ab initio* results for the components of (a) the EDM $\boldsymbol{\mu}(\tau)$ and (b) the polarizability $\underline{\underline{\alpha}}(\tau)$ (symbols). The solid lines are the analytical functions fitted to the *ab initio* results; see below.

C						
C	1	r_2				
C	2	r_3	1	a_3		
C	3	r_4	2	a_4	1	d_4
N	1	r_5	2	a_5	3	d_5
C	2	r_6	1	a_6	3	d_6
C	6	r_7	2	a_7	1	d_7
C	7	r_8	6	a_8	2	d_8
C	8	r_9	7	a_9	6	d_9
H	3	r_{10}	2	a_{10}	1	d_{10}
H	4	r_{11}	3	a_{11}	2	d_{11}
H	6	r_{12}	2	a_{12}	1	d_{12}
H	7	r_{13}	6	a_{13}	2	d_{13}
H	8	r_{14}	7	a_{14}	6	d_{14}
H	9	r_{15}	8	a_{15}	7	d_{15}
O	5	r_{16}	1	a_{16}	2	d_{16}
H	5	r_{17}	1	a_{17}	2	d_{17}
H	16	r_{18}	5	a_{18}	1	d_{18}
H	16	r_{19}	18	a_{19}	5	d_{19}

Table 4.2.: Z-matrix for internal coordinates of indole(H_2O) as used in the input of the *ab initio* calculations.

x_i	$x_0^{(i)}$	$x_1^{(i)}$	$x_2^{(i)}$	$x_3^{(i)}$	$x_4^{(i)}$	$x_5^{(i)}$	$x_6^{(i)}$
r_2	1.4165	0.0000	1.1241×10^{-4}	0.0000	-2.4354×10^{-5}	0.0000	7.9153×10^{-7}
r_3	1.4190	0.0000	-1.5673×10^{-4}	0.0000	-6.2654×10^{-6}	0.0000	-2.3140×10^{-6}
r_4	1.3723	0.0000	-5.2534×10^{-6}	0.0000	1.1913×10^{-5}	0.0000	-2.0983×10^{-6}
r_5	1.3653	0.0000	-1.9057×10^{-4}	0.0000	-1.8848×10^{-5}	0.0000	-4.9656×10^{-6}
r_6	1.3996	0.0000	-1.9349×10^{-5}	0.0000	1.2147×10^{-6}	0.0000	-2.3413×10^{-6}
r_7	1.3798	0.0000	-3.3917×10^{-5}	0.0000	3.2087×10^{-6}	0.0000	-7.9436×10^{-7}
r_8	1.4048	0.0000	-5.2823×10^{-5}	0.0000	-1.4796×10^{-6}	0.0000	-4.7037×10^{-6}
r_9	1.3811	0.0000	-4.8092×10^{-5}	0.0000	1.2176×10^{-5}	0.0000	3.4123×10^{-6}
r_{10}	1.0751	0.0000	-1.4861×10^{-5}	0.0000	-1.0067×10^{-6}	0.0000	-4.9208×10^{-7}
r_{11}	1.0752	0.0000	-5.7300×10^{-6}	0.0000	-4.9008×10^{-6}	0.0000	-2.9040×10^{-6}
r_{12}	1.0798	0.0000	-2.7355×10^{-6}	0.0000	3.3204×10^{-6}	0.0000	2.1854×10^{-6}
r_{13}	1.0797	0.0000	-1.7141×10^{-5}	0.0000	8.4508×10^{-6}	0.0000	1.3853×10^{-6}
r_{14}	1.0795	0.0000	6.4960×10^{-7}	0.0000	-2.0485×10^{-5}	0.0000	-1.7834×10^{-6}
r_{15}	1.0800	0.0000	1.9670×10^{-5}	0.0000	8.2218×10^{-6}	0.0000	6.9811×10^{-7}
r_{16}	2.9378	0.0000	1.4169×10^{-2}	0.0000	-1.2038×10^{-4}	0.0000	-4.9276×10^{-5}
r_{17}	1.0090	0.0000	4.6907×10^{-5}	0.0000	4.8672×10^{-7}	0.0000	3.1249×10^{-6}
r_{18}	9.5964×10^{-1}	1.6137×10^{-5}	-3.7570×10^{-5}	-2.3695×10^{-6}	-1.7981×10^{-5}	7.0582×10^{-7}	-2.5055×10^{-6}
r_{19}	9.5964×10^{-1}	-1.6137×10^{-5}	-3.7570×10^{-5}	2.3695×10^{-6}	-1.7981×10^{-5}	-7.0582×10^{-7}	-2.5055×10^{-6}
a_3	1.8649	0.0000	3.7557×10^{-5}	0.0000	-5.1228×10^{-5}	0.0000	-1.1234×10^{-6}
a_4	1.8647	0.0000	-1.7675×10^{-4}	0.0000	4.1198×10^{-5}	0.0000	1.2049×10^{-6}
a_5	1.8773	0.0000	1.8366×10^{-6}	0.0000	6.5937×10^{-5}	0.0000	1.5983×10^{-6}
a_6	2.0751	0.0000	2.8057×10^{-4}	0.0000	-3.9346×10^{-5}	0.0000	1.3686×10^{-5}
a_7	2.0749	0.0000	2.0874×10^{-4}	0.0000	2.1963×10^{-6}	0.0000	2.3899×10^{-6}
a_8	2.1167	0.0000	-1.8787×10^{-4}	0.0000	2.3553×10^{-5}	0.0000	-3.4979×10^{-6}
a_9	2.1152	0.0000	-2.1611×10^{-4}	0.0000	-2.4107×10^{-5}	0.0000	-6.0503×10^{-6}
a_{10}	2.2269	0.0000	-1.1047×10^{-4}	0.0000	4.6785×10^{-5}	0.0000	-1.6861×10^{-5}

Table 4.3.: Coefficients of the analytical functions (4.5) and (4.6) used to fit the internal coordinates computed with *ab initio* methods.

a_{11}	2.2678	0.0000	-7.3596×10^{-4}	0.0000	-3.7692×10^{-5}	0.0000	1.2068×10^{-5}
a_{12}	2.1047	0.0000	-1.6749×10^{-4}	0.0000	2.1358×10^{-5}	0.0000	1.1809×10^{-6}
a_{13}	2.0896	0.0000	1.6504×10^{-4}	0.0000	-7.4212×10^{-6}	0.0000	-2.8143×10^{-7}
a_{14}	2.0825	0.0000	1.8096×10^{-4}	0.0000	6.1563×10^{-5}	0.0000	8.5536×10^{-6}
a_{15}	2.1148	0.0000	-1.8007×10^{-3}	0.0000	2.2403×10^{-4}	0.0000	-4.2819×10^{-5}
a_{16}	2.1705	0.0000	-2.6675×10^{-4}	0.0000	-8.9622×10^{-3}	0.0000	-1.2984×10^{-3}
a_{17}	2.1885	0.0000	8.9775×10^{-4}	0.0000	-9.4758×10^{-4}	0.0000	1.1903×10^{-5}
a_{18}	2.2242	-4.7488×10^{-2}	9.8120×10^{-4}	-1.5970×10^{-3}	-4.1175×10^{-5}	-4.0832×10^{-3}	1.0285×10^{-5}
a_{19}	1.8347	0.0000	-1.9624×10^{-3}	0.0000	8.2349×10^{-5}	0.0000	-2.0570×10^{-5}

Table 4.3.: continued

n	$\mu_{2n}^{(1)}$ (a. u.)	$\mu_{2n}^{(2)}$ (a. u.)	$\mu_{2n}^{(3)}$ (a. u.)	$\alpha_{2n}^{(11)}$ (a. u.)	$\alpha_{2n}^{(13)}$ (a. u.)	$\alpha_{2n}^{(22)}$ (a. u.)	$\alpha_{2n}^{(33)}$ (a. u.)
0	1.91872	1.146652×10^{-2}	4.742808×10^{-1}	122.4133	7.866651	68.36602	146.069
1	1.897090×10^{-2}	1.110871×10^{-3}	1.161703×10^{-2}	3.613539×10^{-2}	8.455194×10^{-2}	3.895537×10^{-1}	2.378808×10^{-1}
2	4.952774×10^{-3}	1.531671×10^{-3}	6.384580×10^{-3}	1.17512×10^{-1}	2.451433×10^{-1}	-1.195350×10^{-3}	9.374843×10^{-2}
3	1.113748×10^{-3}	6.033855×10^{-4}	8.993579×10^{-4}	1.584098×10^{-2}	3.293678×10^{-2}	1.155859×10^{-3}	1.251454×10^{-2}
4	1.443935×10^{-3}	5.059124×10^{-4}	1.0173×10^{-3}	2.897917×10^{-2}	6.613491×10^{-2}	-1.084440×10^{-3}	2.512222×10^{-2}

Table 4.4.: Coefficients of the analytical functions (4.7) and (4.8) used to fit the EDM and polarizability computed with *ab initio* methods. The components α_{12} and α_{23} are zero.

J	K_c	Γ_{tor}	$\Gamma_{\text{rot}} \otimes \Gamma_{\text{tor}}$	symmetry species
e	e	A_1	A_1	$+$
o	e	A_1	A_1	$-$
e	o	A_1	A_2	$-$
o	o	A_1	A_2	$+$
e	e	A_2	A_2	$-$
o	e	A_2	A_2	$+$
e	o	A_2	A_1	$+$
o	o	A_2	A_1	$-$

Table 4.5.: Symmetry species + and − for $M = 0$ and $\sigma = 0$ in the presence of parallel ac and dc electric fields. The torsional symmetry Γ_{tor} and K_c quantum number refer to the product state $\Psi_l^{rot}(\phi, \theta, \chi)\Psi_m^{tor}(\tau)$ that approximately describes a given field-free rotation-torsional state. To obtain the $M = 0$ symmetry species for the $\sigma = 1$ sublevels, $A_{1,2}$ has to be replaced with $B_{1,2}$.

for the symmetrized coordinates. The coefficients $x_{2n}^{(i)}$ and $x_{2n+1}^{(i)}$ are listed in Table 4.3.

Analytical expressions for the electric dipole moment and polarizability

To represent $\boldsymbol{\mu}(\tau)$ and $\underline{\underline{\alpha}}(\tau)$ by analytical functions of τ, we transform their components to a coordinate system fixed to the molecular bond structure. The first unit vector $\hat{e}_1$ is chosen along the N-O bond axis, the second one $\hat{e}_2$ is perpendicular to the indole plane, and the third one is given by $\hat{e}_3 = \hat{e}_1 \times \hat{e}_2$. Similar to the fit of the PES, we fit the following expressions to the *ab initio* results of $\boldsymbol{\mu}(\tau)$ and $\underline{\underline{\alpha}}(\tau)$:

$$\mu_p = \sum_{n=0}^{4} \mu_{2n}^{(p)} \cos(2n\tau) \ , \ \alpha_{pq} = \sum_{n=0}^{4} \alpha_{2n}^{(pq)} \cos(2n\tau) \tag{4.7}$$

with $p \in \{1, 3\}$ and $pq \in \{11, 22, 33, 13\}$ as well as

$$\mu_2 = \sin(2\tau) \sum_{n=0}^{4} \mu_{2n}^{(p)} \cos(2n\tau) \ . \tag{4.8}$$

The coefficients $\mu_{2n}^{(p)}$ and $\alpha_{2n}^{(pq)}$ are listed in Table 4.4.

Symmetry properties and coupling due to external electric fields

We summarize the symmetry properties of indole(H_2O) and the coupling of different rotation-torsional states in the presence of parallel nonresonant laser and weak static electric fields. In the field-free case, indole(H_2O) belongs to the molecular symmetry group $G_4 = \{E, (12), E^*, (12)^*\}$ [74, 77, 102]. The static electric field mixes field-free states of different parity and the molecular symmetry group of indole(H_2O) in the field reduces to $G_2 = \{E, (12)\}$ [102]. In terms of the product states $\Psi_l^{rot}(\phi, \theta, \chi)\Psi_m^{tor}(\tau)$, the matrix elements of the two parts of the interaction Hamiltonian (4.3) depend on $\left\langle \Psi_m^{tor} \left| \mu_i(\tau) \right| \Psi_n^{tor} \right\rangle$ and $\left\langle \Psi_m^{tor} \left| \alpha_{ij}(\tau) \right| \Psi_n^{tor} \right\rangle$ with $i, j \in x, y, z$, respectively. Since the dipole moment and polarizability do not change sign under the operation (12), rotation-torsional states with different σ are not coupled by the external ac and dc electric fields. The nonzero components of the polarizability are of A_1 symmetry in G_4 and thus only couple field-free torsional states that have the same symmetry. Since the field-free rotation-torsional states are linear combinations of states with the same rotation-torsional symmetry and only approximately described by product states, the coupling due to the laser field (which is the dominant interaction) between field-free states with different torsional symmetry is nonzero, but smaller than the coupling between states with the same torsional symmetry. Here, the torsional symmetry of a field-free rotation-torsional state refers to the product state $\Psi_l^{rot}(\phi, \theta, \chi)\Psi_m^{tor}(\tau)$ with the largest contribution. For parallel laser and static electric fields, M is a good quantum number and we have to distinguish the cases $M = 0$ and $M \neq 0$.

If $M \neq 0$, we find two different symmetry species corresponding to states with A and B symmetry in G_2.

For $M = 0$, the interaction of the laser field with the polarizability as well as the interaction of the static electric field with the y and z components of the dipole moment couple field-free rotational states with the same $J + K_c$ parity. The y and z components of the dipole moment are of A_1 symmetry in G_4 and thus only couple field-free torsional states with the same symmetry. The x component of the dipole moment is of A_2 symmetry and couples field-free torsional states with different parity, i. e., A_1 and A_2 torsional states as well as B_1 and B_2 states. For $M = 0$, the interaction with the x-component of the dipole moment couples field-free rotational states with different $J + K_c$ parity. As a consequence, we find two different symmetry species for each value of σ. The two cases for $\sigma = 0$ are listed in Table 4.5.

5 Laser-induced dynamics of molecules with strong nuclear quadrupole coupling[5]

5.1. Introduction

Laser-controlled rovibrational molecular dynamics is a subject of active research in physics and chemistry [62, 85, 143, 144]. In particular, the control of molecular spatial alignment and orientation [48, 61, 72] is highly leveraged in many ultrafast imaging experiments [4, 8, 11, 17, 62, 70, 145, 146] and stereochemistry studies [27, 147, 148] to increase the experimental resolution. The mechanism of the alignment and orientation is tied to the driven rotational dynamics of molecules in the ground vibrational state and described by two-photon [59, 149] or three-photon [150, 151] Raman excitation processes. The adiabatic alignment is induced by slowly increasing laser electric field, which creates a directional potential trapping molecules in pendular states. Adiabatic alignment combined with a dc electric field, produces the mixed-field orientation of molecules [55, 57, 72]. In the impulsive alignment regime using short laser pulses, the created rotational wavepacket evolves with repeated alignment/orientation and antialignment revivals. In all of these schemes, the temporal evolution of the rotational wavepacket and the resulting revival structure is characteristic to the rotational-energy-level structure of the molecule [55, 58, 152]. Typically, this temporal wavepacket evolution is accurately predicted using the rigid-rotor or semirigid rotor Hamiltonian models [48, 127, 153, 154].

Many heavy atoms, such as, for example, bromine, iodine, or platinum, have large nuclear quadrupoles. In molecules, these create large hyperfine splittings, comparable or even larger than the rotational-energy spacings. These strong hyperfine interactions arise from the coupling between the quadrupole moments of nuclei and the electric field gradients produced by the distribution of nuclei and electrons through the molecule. In such heavy-atom containing molecules the presence of the manifold of hyperfine-split nuclear-spin states makes the temporal evolution of the laser-excited rotational wavepacket, and thus the alignment revival structure, more complicated [95]. Therefore, a detailed understanding of the effect of these nuclear-quadrupole interactions is an important ingredient for the control over the alignment of heavy-atom-containing molecules, with

---

[5] This chapter is based on the publication: *Laser-induced dynamics of molecules with strong nuclear quadrupole coupling*, Andrey Yachmenev, Linda V. Thesing and Jochen Küpper, J. Chem. Phys. **151**, 244118 (2019), arXiv:1910.13275 [physics]. I contributed to the development of the computational code for the hyperfine energy levels and rotational dynamics, performed the calculations of the molecular energy levels, matrix elements as well as alignment, analyzed the data and contributed to writing the manuscript.

corresponding implications for molecular-frame imaging experiments. Heavy atoms are commonly utilized as strong scattering and absorption centers in x-ray imaging experiments [17, 155, 156]. They are also exploited as good leaving groups in Coulomb-explosion velocity-map imaging of molecular dynamics [157, 158].

Here, we present a general variational approach for computing the field-driven rovibrational dynamics of molecules including nuclear-quadrupole interactions. The present approach extends our previously reported variational method for computing the nuclear-quadrupole hyperfine spectra of small molecules [112]. We developed a generalized methodology for computing the matrix representations of various electric-multipole-moment tensor operators in the basis of hyperfine wave functions. These tensor operators are used as building blocks of the molecule-field interaction potential in simulations of the field-driven rovibrational dynamics, as implemented in the computational approach RichMol [115]. To our knowledge, this is the first attempt to generalized simulations of this kind. We demonstrate the effect by calculating the one-dimensional alignment dynamics of the asymmetric $\mathrm{CF^{35}Cl^{79}Br^{127}I}$ molecule by a short laser pulse.

5.2. Theoretical description

In brief, in RichMol the time-dependent wavepacket $\Psi(t)$ is built from a superposition of the field-free rovibrational wave functions $|J, m_J, l\rangle$

$$\Psi(t) = \sum_{J,m_J,l} c_{J,m_J,l}(t)\,|J, m_J, l\rangle\,, \tag{5.1}$$

where J and m_J denote the quantum numbers of the total rotational angular momentum operator $\mathbf{J}$ and its projection onto the laboratory-fixed Z axis, respectively. l represents a set of additional rotational and vibrational quantum numbers. The time-dependent coefficients $c_{J,m_J,l}(t)$ are determined by a numerical solution of the time-dependent Schrödinger equation using the time-evolution operator method. The total Hamiltonian consists of the sum of the molecular rovibrational Hamiltonian H_{rv}, with the eigenfunctions $|J, m_J, l\rangle$, and the molecule-field interaction potential $V(t)$, expanded in terms of molecular electric multipole moment operators:

$$H(t) = H_{\mathrm{rv}} - \mu_A E_A(t) - \frac{1}{2}\alpha_{AB} E_A(t) E_B(t) + \ldots \tag{5.2}$$

A and B are Cartesian indices denoting the X, Y, and Z axes in the laboratory frame and the summation over all Cartesian indices is implicitly assumed. $E_A(t)$ is the A Cartesian component of the electric field vector, and μ_A and α_{AB} are the electronic contributions to the molecular-frame electric-dipole-moment vector and polarizability tensor, respectively. The interaction terms of higher expansion order, such as the first and second hyperpolarizability tensors, can also in principle be included into the sum in (5.2) [115].

The time-evolution operator for the time step $\Delta t = t - t'$ is computed using the split-operator method as

$$\mathcal{U}(t,t') = e^{-i\frac{\Delta t}{2\hbar}H_{\text{rv}}} \Bigg(e^{i\frac{\Delta t}{\hbar}\mu_A E_A(\frac{t+t'}{2})} \\ \cdot e^{i\frac{\Delta t}{2\hbar}\alpha_{AB}E_A(\frac{t+t'}{2})E_B(\frac{t+t'}{2})} \cdot \ldots \Bigg) e^{-i\frac{\Delta t}{2\hbar}H_{\text{rv}}}. \quad (5.3)$$

H_{rv} is diagonal in the basis of its eigenfunctions $|J, m_J, l\rangle$ and the diagonal elements are the molecular rovibrational energies. The exponentials of the Cartesian tensor operators $\mu_A, \alpha_{AB}, \ldots$ are evaluated using an iterative approximation based on the Krylov-subspace methods. The computational performance of the iterative methods depends crucially on how efficient the matrix-vector products can be computed between the operator exponential and the subspace vectors. In the following, we will use $T_A^{(\Omega)}$ to denote any index-symmetric Cartesian tensor operator of rank Ω with A being a multi-index labeling Cartesian components in the upper simplex of the tensor in the laboratory frame. For example, for the dipole moment, $\Omega = 1$ and $A = X$, Y, or Z, and for the polarizability tensor, $\Omega = 2$ and $A = XX$, XY, XZ, YY, YZ, or ZZ.

The computations of the matrix-vector products can be significantly sped up by expressing the matrix representation of Cartesian tensor operators $T_A^{(\Omega)}$ in a contracted tensor form:

$$\langle J', m_J', l'|T_A^{(\Omega)}|J, m_J, l\rangle = \sum_{\omega=0}^{\Omega} \mathcal{M}_{A,\omega}^{(J',m_J',J,m_J)} \mathcal{K}_{\omega}^{(J',l',J,l)}. \quad (5.4)$$

The sum runs over all irreducible representations ω of the tensor and the matrices $\mathcal{M}_{A,\omega}^{(J',m_J',J,m_J)}$ and $\mathcal{K}_{\omega}^{(J',l',J,l)}$ decouple the laboratory-frame projections A and quantum numbers m_J and m_J' from the molecular-frame rovibrational quantum numbers l and l'.

The explicit expressions for the $\mathcal{M}_{A,\omega}$ and $\mathcal{K}_\omega$ matrices depend on the form of the field-free wave functions $|J, m_J, l\rangle$. We use the general-molecule variational approach TROVE [110, 113, 114, 159] to compute the field-free energies and wave functions $|J, m_J, l\rangle$, which are represented by linear combinations of products of vibrational wave functions $|v\rangle$ and symmetric-top rotational functions $|J, m_J, k\rangle$

$$|J, m_J, l\rangle = \sum_{v,k} c_{v,k}^{(J,l)} |v\rangle |J, m_J, k\rangle . \quad (5.5)$$

v denotes the composite vibrational quantum number and k denotes the quantum number of the molecular-frame z-projection of the rotational angular momentum operator. Using the wave functions from (5.5), the expressions for $\mathcal{M}_{A,\omega}$ and $\mathcal{K}_\omega$ can be derived as

$$\mathcal{M}_{A,\omega}^{(J',m_J',J,m_J)} = (-1)^{m_J'} \sqrt{(2J'+1)(2J+1)} \\ \times \sum_{\sigma=-\omega}^{\omega} [U^{(\Omega)}]^{-1}_{A,\omega,\sigma} \begin{pmatrix} J & \omega & J' \\ m_J & \sigma & -m_J' \end{pmatrix} \quad (5.6)$$

and

$$\mathcal{K}_{\omega}^{(J',l',J,l)} = \sum_{k',v'}\sum_{k,v}\left[c_{v',k'}^{(J',l')}\right]^{*} c_{v,k}^{(J,l)}(-1)^{k'}$$
$$\times \sum_{\sigma=-\omega}^{\omega}\sum_{a}\begin{pmatrix} J & \omega & J' \\ k & \sigma & -k' \end{pmatrix} U_{\omega,\sigma,a}^{(\Omega)}\left\langle v'\left|T_{a}^{(\Omega)}\right|v\right\rangle. \tag{5.7}$$

$T_a^{(\Omega)}$ denotes Cartesian tensor operator in the molecular frame, with a being a Cartesian multi-index (similar to A), and the matrix $U^{(\Omega)}$ defines the transformation of tensor from Cartesian to spherical-tensor form [115].

This approach is general and can be interfaced with any rovibrational computer code that provides the tensor-matrix elements in the form of (5.4). The approach also permits the use of more complex field-free wave functions than those defined in (5.5). As multipole-moment operators commute with the nuclear-spin angular momenta, the operators' matrix elements in the basis of hyperfine states can also be cast into the form of (5.4). In the following, we derive the explicit expressions for the $\mathcal{M}_{A,\omega}$ and $\mathcal{K}_{\omega}$ matrix elements in the basis of the nuclear-spin hyperfine-structure wave functions.

The general variational implementation of the nuclear-spin hyperfine effects at the level of the nuclear-quadrupole interaction was recently implemented [112] and used for the generation of a quadrupole-resolved line list of the ammonia molecule [160]. The nuclear-quadrupole interaction in a molecule containing $n = 1 \ldots N$ quadrupolar nuclei is described by the coupling of the electric field gradient tensor (EFG) at each n-th nucleus $\mathbf{V}(n)$ with its quadrupole moment tensor $\mathbf{Q}(n)$. The total spin-rovibrational Hamiltonian takes the form

$$H_{\text{srv}} = H_{\text{rv}} + \sum_{n}\mathbf{V}(n)\cdot\mathbf{Q}(n). \tag{5.8}$$

The overall rotational, $\mathbf{J}$, and the nuclear spin, $\mathbf{I}_n$, and total, $\mathbf{F}$, angular momentum operators for $n = 1 \ldots N$ quadrupolar nuclei are coupled as $\mathbf{I}_{1,2} = \mathbf{I}_1 + \mathbf{I}_2$, $\mathbf{I}_{1,3} = \mathbf{I}_{1,2} + \mathbf{I}_3$, $\ldots$, $\mathbf{I}_{1,N-1} = \mathbf{I}_{1,N-2} + \mathbf{I}_{N-1}$, $\mathbf{I} \equiv \mathbf{I}_{1,N} = \mathbf{I}_{1,N-1} + \mathbf{I}_N$, and $\mathbf{F} = \mathbf{J} + \mathbf{I}$. The nuclear-spin functions $|I, m_I, \mathcal{I}\rangle$ depend on the quantum numbers I and m_I of the collective nuclear spin angular momentum operator $\mathbf{I}$ and its projection onto the laboratory Z axis, respectively. The set of auxiliary spin quantum numbers $\mathcal{I} = \{I_1, I_{1,2}, \ldots, I_{1,N-1}\}$ of the intermediate spin angular momentum operators provide a unique assignment of each nuclear-spin state. The total spin-rovibrational wave functions $|F, m_F, u\rangle$ are built as symmetry-adapted linear combinations of the products of the rovibrational wave functions

$|J, m_J, l\rangle$ in (5.5) and the nuclear-spin functions $|I, m_I, \mathcal{I}\rangle$:

$$|F, m_F, u\rangle = \sum_{I,\mathcal{I},J,l} c^{(F,u)}_{I,\mathcal{I},J,l} \left[\sum_{m_J,m_I} (-1)^{F+m_F} \right. \\ \left. \times \sqrt{2F+1} \begin{pmatrix} F & I & J \\ -m_F & m_I & m_J \end{pmatrix} |I, m_I, \mathcal{I}\rangle \, |J, m_J, l\rangle \right]. \quad (5.9)$$

$c^{(F,u)}_{I,\mathcal{I},J,l}$ are the eigenvector coefficients of the spin-rovibrational Hamiltonian (5.8), F and m_F are the quantum numbers of $\mathbf{F}$ and its projection onto the laboratory-fixed Z-axis, and u denotes the hyperfine-state running index.

The explicit expressions for the matrix elements of the spin-rovibrational Hamiltonian (5.8) for an arbitrary number of quadrupolar nuclei and details of the variational solution can be found in reference [112]. Here, we derived explicit expressions for the matrix elements of the general electric multipole Cartesian tensor operator $\left\langle F', m'_F, u' \middle| T^{(\Omega)}_A \middle| F, m_F, u \right\rangle$, which in the contracted-tensor form of (5.4) are

$$\mathcal{M}^{(F',m'_F,F,m_F)}_{A,\omega} = (-1)^{m'_F} \sqrt{(2F'+1)(2F+1)} \\ \times \sum_{\sigma=-\omega}^{\omega} [U^{(\Omega)}]^{-1}_{A,\omega,\sigma} \begin{pmatrix} F' & \omega & F \\ -m'_F & \sigma & m_F \end{pmatrix} \quad (5.10)$$

and

$$\mathcal{K}^{(F',u',F,u)}_{\omega} = \sum_{I',\mathcal{I}',J',l'} \sum_{I,\mathcal{I},J,l} \left[c^{(F',u')}_{I',\mathcal{I}',J',l'} \right]^{*} c^{(F,u)}_{I,\mathcal{I},J,l} (-1)^{I} \\ \times \sqrt{(2J'+1)(2J+1)} \begin{Bmatrix} J' & F' & I \\ F & J & \omega \end{Bmatrix} \mathcal{K}^{(J',l',J,l)}_{\omega} \delta_{I',I} \delta_{\mathcal{I}',\mathcal{I}}. \quad (5.11)$$

$\mathcal{K}^{(J',l',J,l)}_{\omega}$, defined in (5.7), contains the rovibrational matrix elements of $T^{(\Omega)}_A$ in the basis $|J, m_J, l\rangle$. Using the expressions (5.10) and (5.11) in (5.4), RichMol could directly be employed to simulate the coupled nuclear-spin-rovibrational molecular dynamics in external fields. In (5.3), the diagonal representation of H_{rv} in the rovibrational energies was replaced by the diagonal representation of H_{srv} in the hyperfine energies (5.8).

5.3. Results and discussion

This new approach was used to investigate the effect of nuclear-quadrupole coupling on the impulsive alignment of bromochlorofluoroiodomethane $CF^{35}Cl^{79}Br^{127}I$. This molecule has a quasi-rigid structure and contains three different heavy nuclei with large quadrupole coupling constants and with correspondingly nontrivial laser-induced rotational and nuclear spin spectra and dynamics. A short non-resonant laser pulse is linearly polarized along the laboratory Z axis. Its intensity is given by the Gaussian function $I(t) = I_0 \exp\left(-4\ln 2t^2/\sigma^2\right)$ with $\sigma = 1$ ps and $I_0 = 6 \times 10^{11}$ W/cm^2 or 1×10^{12} W/cm^2. The excitation by a non-resonant laser field is described by the electric polarizability term in the interaction potential (5.2). The explicit expressions for the elements of the matrix $U^{(2)}$ for the polarizability are listed in the Table I of reference [115]. The degree of molecular alignment is characterized by the expectation value $\left\langle\cos^2\theta\right\rangle = \left\langle \Psi(t) \left|\cos^2\theta\right| \Psi(t) \right\rangle$, with the angle θ between the molecular-frame z and the laboratory-frame Z axes. The matrix elements of the $\cos^2\theta$ operator can be easily computed using the general expressions (5.10), (5.11), and (5.7) by noting the relationship $\cos^2\theta = (2d^2_{00} + 1)/3$, where d is the Wigner d matrix. The vibrational matrix elements of d^2_{00} in (5.7) are $\langle v'|d^2_{00}|v\rangle = \delta_{v'v}$ and $U^{(0)}_{\omega,\sigma} = \delta_{\omega,2}\delta_{\sigma,0}$; here the index a in (5.7) is redundant.

For simplicity we neglected the vibrational motion of the molecule and approximated the full rovibrational wave functions in (5.5) by rigid-rotor solutions. The rigid-rotor approximation in simulations of the laser-induced alignment of quasi-rigid and even non-rigid molecules in ultracold molecular beams has been validated in numerous studies [45, 55, 60, 64, 154, 161]. The zero-point vibrational corrections to various electromagnetic tensors are known to be quite small, on the order of 1–3%, even for non-rigid molecules like H_2O_2 [162] and have been neglected in this study. The equilibrium geometry and polarizability of CFClBrI were calculated using density functional theory (DFT) with the B3LYP functional and the def2-TZVPP basis set [163, 164] in conjunction with the relativistic effective core potential def2-ECP on the iodine atom [165]. The accuracy of hybrid functionals for the prediction of molecular polarizabilities was assessed on a dataset of 132 molecules, yielding a root-mean-square error of 3–5 % relative to CCSD(T) [166]. Calculations of the electric field gradient tensors, needed for the nuclear-quadrupole coupling Hamiltonian in (5.8), were carried out at the DFT/B3LYP level of theory using the all-electron scalar relativistic Douglas-Kroll-Hess Hamiltonian [167] with the DKH-def2-TZVP basis set [168, 169]. Systematic studies of the accuracy of DFT functionals for predictions of the electric field gradient tensors of transition metal complexes provided a mean error estimate of about 0.071 a.u. for the B3LYP functional [170]. All electronic structure calculations employed the quantum chemistry package ORCA [171, 172]. The quadrupole moments for the ^{35}Cl, ^{79}Br, and ^{127}I nuclei are $Q = -81.65$ mb, 313 mb, and -696 mb, respectively [173].

The calculations of the molecule-field dynamics in the basis of the nuclear-spin hyperfine states were performed in a three-step procedure: First we solved the field-free problem using the rigid-rotor Hamiltonian and obtained the rotational energies and the rotational matrix elements of the EFG and the polarizability tensors, as well as of the $\cos^2\theta$ operator, (5.6) and (5.7). Then we used the rotational energies and the matrix elements of the EFG tensors together with the nuclear-quadrupole constants to build and diagonalize the nuclear-spin quadrupole-coupling Hamiltonian [112], (5.8). We obtained the spin-rotational eigenfunctions in (5.9) and transformed the rotational matrix elements of the polarizability tensor and $\cos^2\theta$ operator into the spin-rotational eigen-basis using (5.10) and (5.11). Finally, we used the spin-rotational energies and the

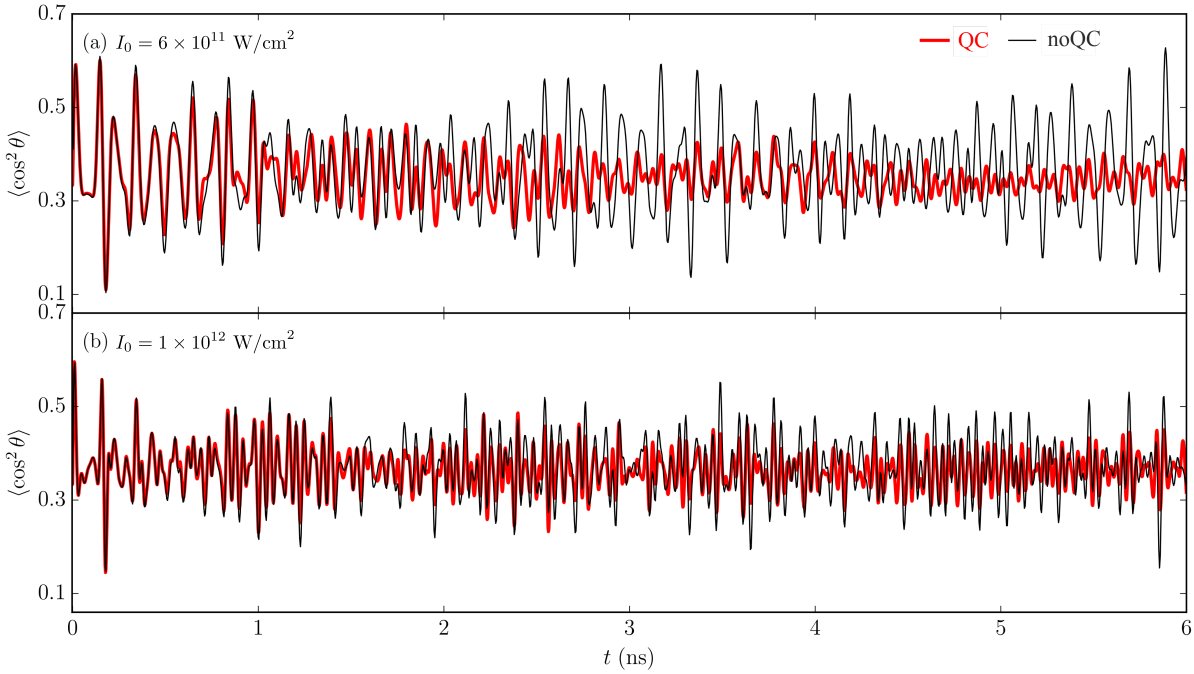

Figure 5.1.: Laser-alignment dynamics of CFClBrI, with and without nuclear-quadrupole coupling (QC and noQC) following excitation by a Gaussian laser pulse with $\tau_{\text{FWHM}} = 1$ ps and a maximum laser intensity of (a) $I_0 = 6 \times 10^{11}$ W/cm^2 and (b) $I_0 = 1 \times 10^{12}$ W/cm^2.

matrix elements of the polarizability to build the molecule-field interaction Hamiltonian and solve the time-dependent problem. The wavepacket $\Psi(t)$ in (5.1) was built from a linear combination of spin-rotational wave functions with time-dependent coefficients. The expectation value $\langle\cos^2\theta\rangle$ is calculated from the spin-rotational matrix elements of $\cos^2\theta$ computed at the previous step.

Here, we used a rotational basis that included all spin-rotational states of CFClBrI with $F \leq 41/2$, corresponding to $J \leq 26$. We assumed that CFClBrI is initially in the ground rotational state $J = 0$, which has 96 different nuclear-spin state components, including the m_F degeneracy. Therefore, we performed a series of simulations starting from the different nuclear-spin components and averaged the results assuming equal normalized populations of different spin components. For comparison, we also performed calculations neglecting the hyperfine effects, i. e., using rigid-rotor wavefunctions as the field-free basis. It should be noted that samples of heavy molecules populating a few of the lowest rotational states, with $T_{\text{rot}} \approx 0.4$ K, can be produced from cold molecular beams using the electrostatic deflector [71, 121, 133].

The temporal evolution of the alignment calculated for two different laser intensities is shown in Figure 5.1. For both laser intensities, the alignment without nuclear-quadrupole interaction shows complex revival patterns originating from the dephasing and rephasing of the rotational wavepacket. Since CFClBrI is an asymmetric-top molecule (asymmetry parameter $\kappa = -0.75$), the revival patterns lack the typical periodicity of the J-type or C-type revivals observed for near-symmetric-top molecules [64, 65, 174]. Noticeably, the broader wave packet, produced by the higher-intensity pulse, shows higher-frequency oscillations and generally reduced peak alignment. This is ascribed to mismatches of the phases of the populated rotational states after the laser pulse [69] and successive dephasing due to the molecule's asymmetry [64], preventing the simultaneous rephasing of more than a few rotational states with significant populations.

The nuclear-quadrupole interaction increases complexity of the revival dynamics and depletion of the peak alignment compared to the rigid-rotor results. Nevertheless, during the first 300 ps after the laser pulse the degree of alignment is almost identical to the rigid-rotor result. We also observed a dependence of the nuclear-quadrupole effect on the laser-field intensity. For the lower intensity, Figure 5.1 (a), the impact is seen about 200 ps earlier than for the higher intensity, Figure 5.1 (b).

The non-periodic recurrences in the alignment dynamics of the asymmetric-top molecules originate from large asymmetry splittings of the rotational energy levels. The influence of the nuclear-quadrupole interaction can be understood in a similar manner, as dephasing effect resulting from the incommensurate hyperfine splittings for different rotational states. The dephasing is stronger for the wavepacket dominated by the low-energy rotational states, where the hyperfine splittings are most irregular. For large J, the hyperfine splittings become increasingly uniform [106] and the contribution to the dephasing is minimized. This explains why the effect of the nuclear-quadrupole interaction is less striking for the higher-intensity laser field, which populates higher-energy rotational states. For both intensities, however, the small-J states have relatively large populations and the nuclear-quadrupole interaction has a strong influence on the field-free alignment.

5.4. Conclusions

In conclusion, we have presented the first general implementation of nuclear-quadrupole hyperfine effects in the rovibrational dynamics of molecules driven by external electric fields. Our approach combines TROVE, which provides hyperfine energies and wave functions for arbitrary molecule, with RichMol, designed for generalized simulations of external-field effects. In principle, the presented approach can be applied to simulate the fully-coupled spin-rovibrational dynamics of any molecule with no inherent limitations on the number of quadrupolar nuclei. The external field effects are not limited by the polarizability interaction: other multipole moment operators, including the permanent dipole moment or the first and second hyperpolarizabilities, can be considered without additional implementation efforts.

We studied the influence of the nuclear-quadrupole coupling on the laser impulsive alignment of a prototypical heavy-atom molecule CFClBrI. While the effect is small for the first few revivals, it turns out to be entirely detrimental for the revivals at later times. The laser field plays an important role, with lower intensities prompting larger effect of the nuclear-quadrupole coupling. This can be explained by dephasing of the rotational wavepacket due to the incommensurate structure of the hyperfine-split levels for different rotational states. This effect is stronger for small-J rotational states and practically disappears for states with high angular momenta. Given that small-J states in the wavepacket will be the source of the largest dephasing effects, we expect that stronger laser intensities and higher initial rotational temperatures should further diminish the effect of the nuclear-quadrupole coupling. More rigorous studies of these effects for different alignment scenarios and molecular systems are ongoing. We envisage future applications of the presented approach to inform and interpret diverse laser-field experiments on molecules containing nuclei with large quadrupole constant.

6 The effect of nuclear-quadrupole coupling in the laser induced alignment of molecules[6]

6.1. Introduction

Controlling the rotational motion of molecules with external electric fields is among the most interesting goals in physical chemistry. The simplest approach to theoretically describe this field-induced control relies on applying the rigid rotor approximation. For many molecular species, this approach has been shown to be sufficient [45, 55, 60, 64, 161], even for some floppy molecules [154]. However, the coupling of the overall angular momentum to additional angular momenta or internal rotations cannot be neglected under certain circumstances. For instance, it has been shown that coupling of nuclear spins and the overall angular momentum can have a significant impact on the rotational dynamics on experimentally relevant timescales [86–94].

Fixing molecules in space, i. e., aligning and orienting them [31, 48, 49], is of particular interest among rotational control schemes as it reduces the blurring of experimental observables caused by averaging over the random orientations and allows to obtain information in the molecular frame [20, 70, 132]. Molecules can be aligned by subjecting them to nonresonant laser fields. If the laser pulse is switched on slowly compared to the molecular rotational period, adiabatic alignment is achieved. On the other hand, by using short laser pulses, coherent superpositions of field-free rotational states are created. The wavepackets rephase periodically and show revivals of the alignment in field-free space [58, 60, 62, 152]. Such coherent superpositions can also be obtained by shaped laser pulses which are turned off rapidly compared to the rotational period of the molecule [42, 66–69].

Recently, it has been shown that the impulsive alignment of I_2 molecules can only be described accurately if the nuclear-quadrupole coupling is taken into account [95]. Here, we systematically analyze the impact of this coupling for different laser intensities and pulse shapes for both linear and asymmetric top molecules using I_2 and 1,4-diiodobenzene as examples. Our results thereby serve as a guideline to understand under which circumstances the quadrupole coupling has a significant influence on the rational dynamics.

---

[6] This chapter is based on the publication: *The effect of nuclear-quadrupole coupling in the laser induced alignment of molecules*, Linda V. Thesing, Andrey Yachmenev, Rosario González-Férez and Jochen Küpper, J. Phys. Chem. A, accepted (2020), arXiv:1911.12270 [physics]. I contributed to the development of the computational code for the hyperfine energy levels and rotational dynamics, performed the calculations of the molecular energy levels, matrix elements as well as alignment, analyzed the data and contributed to writing the manuscript.

6.2. Theoretical description

In I_2 and 1,4-diiodobenzene (DIB), the interaction between the nuclear quadruple moments of two equivalent iodine ^{127}I nuclei and the electric field gradients, arising from the charge distributions of the surrounding nuclei and electrons, lead to the well known hyperfine splittings of the rotational energy levels. Each rotational level of the molecule is thus split into a maximum of 36 sub-levels, labeled by the quantum number F of the total angular momentum operator $\boldsymbol{F} = \boldsymbol{J} + \boldsymbol{I}$, where $\boldsymbol{J}$ is the rotational angular momentum neglecting the spin, which for the molecules considered here is the angular momentum of overall rotation. Here, $\boldsymbol{I} = \boldsymbol{I}_1 + \boldsymbol{I}_2$ is the collective nuclear spin angular momentum operator with $I_1 = I_2 = 5/2$ and thus $0 \leq I \leq 5$.

The theoretical model to describe the nuclear-quadrupole interactions has been described before [175]. Briefly, within the Born-Oppenheimer and semirigid-rotor approximations, the field-free Hamiltonian can be written as

$$H_{\mathrm{mol}} = H_{\mathrm{rot}} + \sum_{l=1,2} \boldsymbol{V}(l) \cdot \boldsymbol{Q}(l), \tag{6.1}$$

where H_{rot} is the semirigid-rotor Hamiltonian. The molecule-fixed frame (MFF), x, y, z, is defined by the principal axes of inertia. In the second term, $\boldsymbol{Q}(l)$ is the nuclear-quadrupole tensor of the l-th iodine nucleus and $\boldsymbol{V}(l)$ is the electric-field-gradient tensor at the instantaneous position of the corresponding nucleus. The elements $V_{ij}(l)$ $(i, j = x, y, z)$ and all relevant molecular parameters are provided in section 6.5.

The interaction of a molecule with a nonresonant laser field, linearly polarized along the laboratory-fixed Z axis, is given by

$$H_{\mathrm{las}}(t) = -\frac{I(t)}{2\varepsilon_0 c}\alpha_{ZZ} \tag{6.2}$$

where α_{ZZ} is the element of the polarizability tensor of the molecule along the laser polarization axis. The polarizabilities defined in the laboratory frame are directly transformed to the molecular frame α_{ij} $(i, j = x, y, z)$ [115], see section 6.5.

To study the rotational dynamics of I_2 and DIB, we solve the time-dependent Schrödinger equation (TDSE) for the full Hamiltonian

$$H(t) = H_{\mathrm{mol}} + H_{\mathrm{las}}(t). \tag{6.3}$$

The time-dependent wave function is built from a superposition of the field-free spin-rotational eigenfunctions of H_{mol}; see section 6.5. The time-dependent coefficients are determined by numerical solution of the TDSE using the split-operator method using RichMol [115]. The alignment is quantified by $\left\langle\cos^2\theta\right\rangle$, with the Euler angle θ between the molecule-fixed z and the laboratory-fixed Z axes.

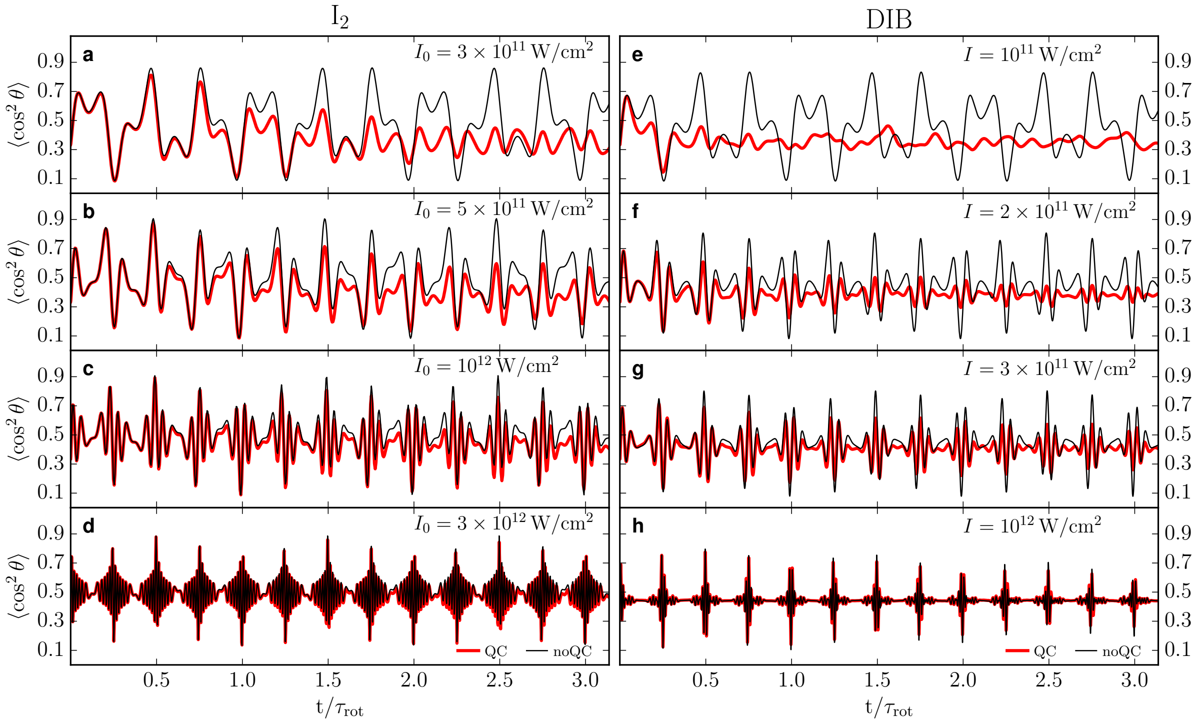

Figure 6.1.: Impulsive alignment induced by laser pulses with $\tau_{\mathrm{FWHM}} = 1$ ps for (a–d) I_2 and (e–h) DIB including (QC) and neglecting the nuclear-quadrupole coupling (noQC). The expectation value $\langle \cos^2\theta \rangle$ is shown as a function of t/τ_{rot}, where τ_{rot} is the rotation period of the molecules. For each row, the laser intensities were chosen to create rotational wave packets involving similar distributions of J values for both molecules when the quadrupole coupling is neglected.

6.3. Results and discussion

Adiabatic alignment We considered a linearly polarized laser pulse with a Gaussian envelope $I(t) = I_0 \exp\left(-4 \ln 2 t^2/\tau^2_{\mathrm{FWHM}}\right)$, where $\tau_{\mathrm{FWHM}} = 8$ ns and $I_0 = 2 \times 10^{11}$ W/cm^2. For the rotational temperature $T_{\mathrm{rot}} = 0$ K, we assumed that all hyperfine states corresponding to the rotational ground state $J = 0$ were populated according to their statistical weights. For I_2, the spin-rotational states with even I have equal weights while the ones with odd I have zero weights [176]. For DIB, the Hydrogen nuclear-spin functions result in weights of 7 (3) for even (odd) I; see section 6.5. The adiabatic alignment with nuclear-quadrupole coupling was computed by averaging over individually obtained alignment results for the 15 (36) initial nuclear-spin states of I_2 (DIB).

As the interaction of the external electric field with the polarizability of the molecules is much stronger than the quadrupole interaction, the influence of the nuclear-quadrupole coupling is negligible for both molecules. At the peak intensity, we thus obtained $\langle \cos^2\theta \rangle = 0.946$ and $\langle \cos^2\theta \rangle = 0.988$ for I_2 and DIB, respectively, both, including and neglecting the quadrupole coupling.

Impulsive alignment We analyzed the impulsive alignment induced by short ($\tau_{\mathrm{FWHM}} =$ 1 ps) nonresonant linearly polarized laser pulses with Gaussian envelopes. We compared the post-pulse dynamics including and neglecting the nuclear-quadrupole coupling for the rotational gound states, i. e., $T_{\text{rot}} = 0$ K. To allow for a better comparison of the alignment with and without the coupling, we used initial states with well defined rotational quantum numbers, i. e., uncoupled states $|IM_I\rangle\,|00\rangle$ ($|IM_I\rangle\,|0_{00}0\rangle$) for I_2 (DIB), and averaged over the results for the different spin isomers, see above. We point out that the corresponding field-free eigenstates have contributions of $J > 0$ rotational states, which might lead to additional differences in the dynamics. To solve the TDSE, we projected each initial state onto the field-free eigenbasis.

Figure 6.1 shows the post-pulse alignment for (a–d) I_2 for intensities 3×10^{11} W/cm^2 $<$ $I_0 < 3\times10^{12}$ W/cm^2 and (e–h) DIB for intensities 10^{11} W/cm^2 $< I_0 < 10^{12}$ W/cm^2 as a function of time in units of the rotational periods, $\tau_{\text{rot}} = 446.98$ ps and $\tau_{\text{rot}} = 3187.48$ ps for I_2 and DIB, respectively. The post-pulse alignment simulated without the quadrupole interaction shows typical revival structures for rotational wave packets induced by short laser pulses. For the smallest intensities, Figure 6.1 a, e, the field-dressed dynamics is dominated by a few low-energy rotational states and $\langle\cos^2\theta\rangle$ oscillates with the period τ_{rot}. For DIB and $I_0 = 10^{11}$ W/cm^2, contributions of rotational states with $K_a > 0$ are negligible and the post-pulse dynamics is similar to the one of the linear molecule I_2. With increasing intensity I_0, more highly excited rotational states are involved in the dynamics. The rotational dynamics of DIB in Figure 6.1 h shows a decrease of the peak alignment over time resulting from the asymmetry splitting of rotational states with $K_a > 0$ [64, 65].

The effect of the nuclear-quadrupole coupling on the alignment depends strongly on the laser intensity. For the low intensities in Figure 6.1 a, e it is strongest and the field-free alignment decreases over time for both I_2 and DIB. However, during the short pulse the quadrupole interaction plays a negligible role for both molecules and the laser field only affects the rotational part of the wave packet, leaving the nuclear spin quanta unchanged. As a consequence, the alignment traces with and without the quadrupole coupling are very similar to each other directly after the laser pulse. This also holds for higher laser intensities.

For DIB, the alignment then decreases quickly after the pulse, while for I_2 the rotational dynamics starts to differ at $t \approx \tau_{\text{rot}}/2$. This decrease in the field-free alignment for small intensities can be rationalized in terms of the hyperfine energy levels of the Hamiltonian (6.1). For the low-energy rotational states, which contribute most to the dynamics in Figure 6.1 a, e, the hyperfine-splitting patterns depend strongly on J. These irregular patterns introduce incommensurate frequencies that lead to a dephasing of the wave packet, thus preventing strong revivals of the alignment. In contrast to I_2, for DIB the energy differences of hyperfine components within the low-energy rotational states are similar to the energy differences between the rotational levels themselves and strong inter-J coupling is observed in the spin-rotational states. As a consequence, the alignment of DIB is affected much more strongly and faster, with respect to the rotational timescale, than it is for I_2.

The influence of the quadrupole coupling can also be interpreted using a classical picture. The precession of $\boldsymbol{I}$ and $\boldsymbol{J}$ around $\boldsymbol{F}$ results in a variation of their projections

M_J and M_I, leading to a decrease of the alignment. In addition, the magnitudes $|\boldsymbol{I}|$ and $|\boldsymbol{J}|$ are changed over time by the quadrupole coupling, further affecting the rotational dynamics. Note that for I_2, the changes in $|\boldsymbol{J}|$ are very small but a change in $|\boldsymbol{I}|$ stills affects the spatial orientation of $\boldsymbol{J}$, since the total angular momentum $\boldsymbol{F}$ is preserved.

As the laser intensity was risen, Figure 6.1 b–d, f–h, the influence of the quadrupole interaction diminished for both molecules. In Figure 6.1 d, h, minor differences can only be observed after the first rotational period. For these strong fields, highly excited states with up to $J \approx 44$ (and $K_a \approx 10$ for DIB) dominate the post-pulse dynamics, for which the hyperfine patterns become increasingly uniform [106, 108]. For these large J, the matrix elements of $\cos^2\theta$ that contribute significantly to the alignment are those between field-free eigenstates with $\Delta F = \Delta J$ and the same nuclear-spin contributions. Since the hyperfine energy shifts are approximately the same for these states, their energy gaps are very similar to those between the corresponding rotational levels. As a result, we observe only a very weak dephasing in Figure 6.1 d, h.

If field-free eigenstates are used as initial states the averaged alignment results for I_2 do not differ significantly from the result in Figure 6.1. For DIB on the other hand, we observe small deviations originating from a considerable mixing of different J-states in the hyperfine eigenstates, modifying the initial rotational wave function. The impact of the quadrupole interaction is, however, qualitatively the same. The different sets of initial states can only be considered equivalent when the result is averaged over all different spin isomers and M-states for a given rotational level. Individual eigenstates are in general linear combinations of uncoupled states with different values of I, M_I and M_J, even if the coupling of different J-states by the quadrupole interactions is neglected.

Truncated pulse alignment For asymmetric top molecules, truncated laser pulses typically allow to obtain larger degrees of field-free alignment than short laser pulses, taking advantage of the initial adiabatic alignment [66, 69]. Here, we consider a laser pulse with a rising and falling edge, both with a Gaussian shape corresponding to $\tau_\text{FWHM} = 600$ ps and $\tau_\text{FWHM} = 2$ ps, respectively, and a peak intensity of $I_0 = 5 \times 10^{11}\,\text{W/cm}^2$.

The alignment results for I_2 and DIB as a function of t/τ_rot are shown in Figure 6.2 a, b, respectively. For both molecules, strong alignment was reached before the cut-off of the laser field with $\left\langle\cos^2\theta\right\rangle$ close to 1. As in the adiabatic regime, the effect of the quadrupole coupling on the degree of alignment is very weak in the presence of the field. After the laser field is switched off, the quadrupole-free alignment shows a typical revival structure. For the linear I_2 molecules, $\left\langle\cos^2\theta\right\rangle$ at the full revival $t = \tau_\text{rot}$ reaches the same value as during the pulse, $\left\langle\cos^2\theta\right\rangle = 0.96$. Analogous behavior was observed for DIB with $\left\langle\cos^2\theta\right\rangle = 0.98$. Note that such high degrees of the post-pulse alignment for DIB are generally possible because the molecule is a near symmetric-top with only small populations of states with $K_a > 0$, effectively reducing the dynamcis to that of a linear rotor. Generally, the peak alignment of asymmetric top molecules at the full revival does not reach the same value as at the peak intensity of the truncated pulse [42, 69].

For both molecules, the dephasing due to the nuclear-quadrupole coupling is comparable to the impulsive alignment case with intermediate intensities, see Figure 6.1 b, f.

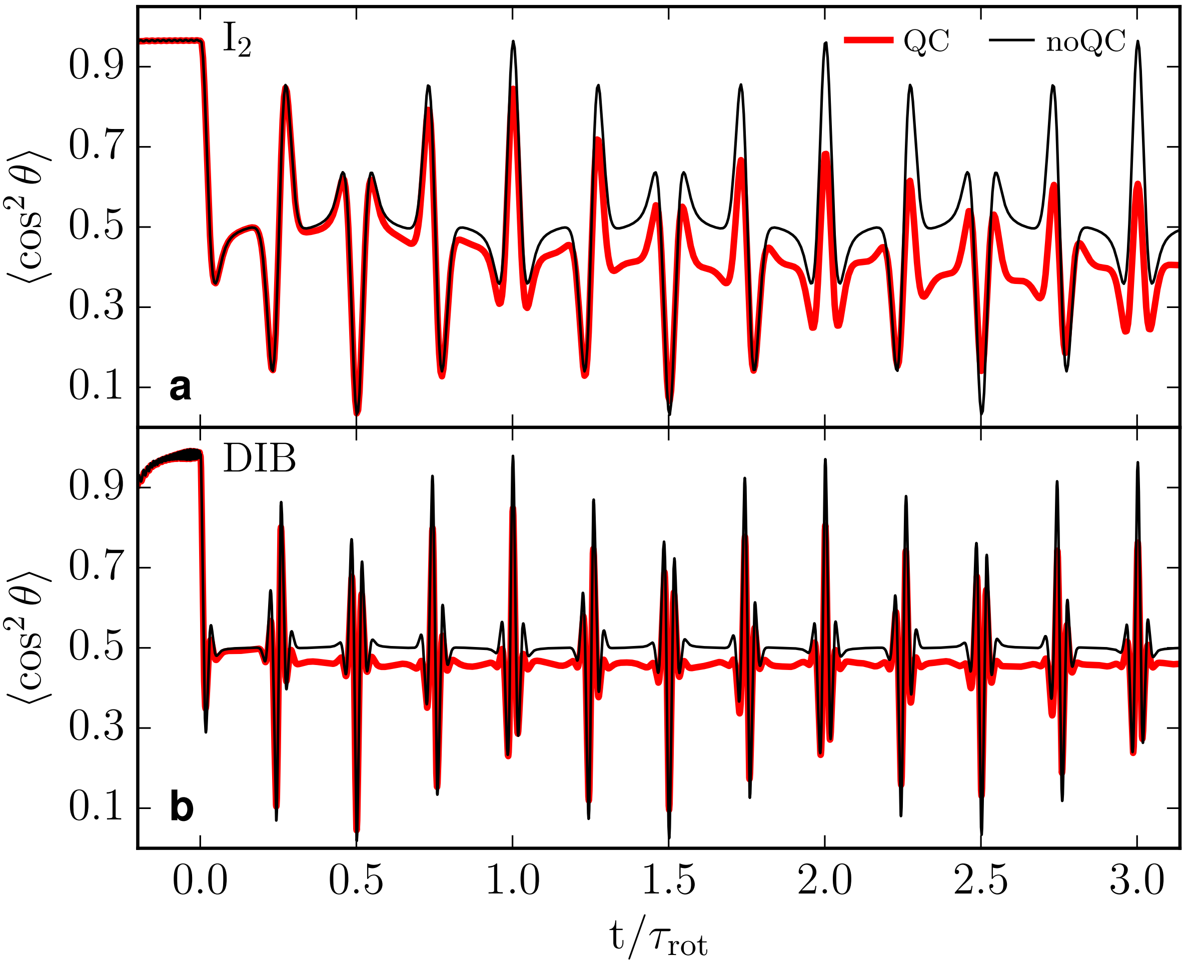

Figure 6.2.: Truncated pulse alignment with and without quadrupole coupling (QC and noQC) as a function of t/τ_{rot} for (a) I_2 and (b) DIB following a truncated laser pulse with a maximum laser intensity of $I_0 = 5 \times 10^{11}\text{W/cm}^2$. The rising and falling edges of the pulse had Gaussian shapes with $\tau_{\text{FWHM}} = 600$ ps and 2 ps, respectively.

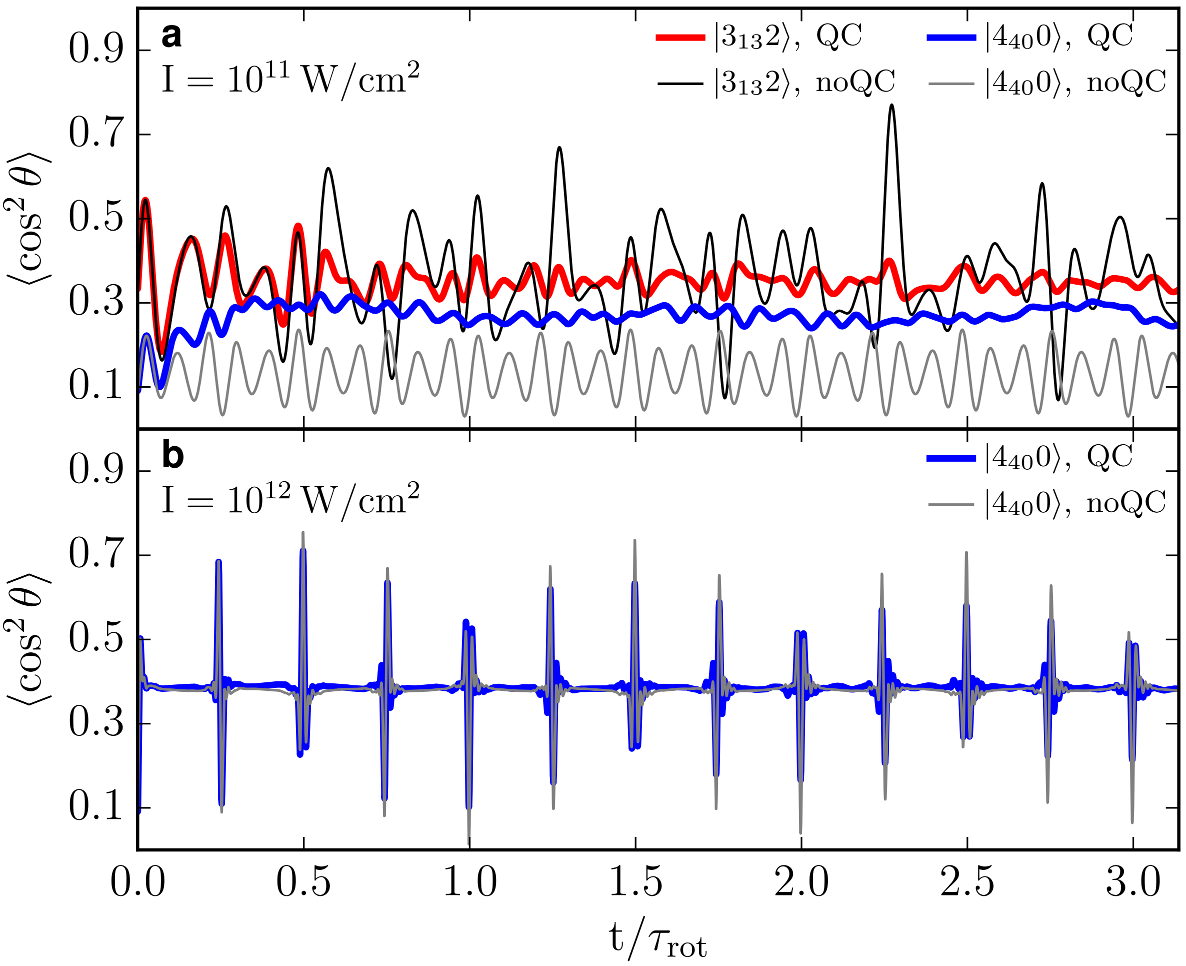

Figure 6.3.: Impulsive alignment for the initial states $|3_{13}2\rangle$ and $|4_{40}0\rangle$ of DIB including the quadrupole coupling (QC) and neglecting it (noQC) as a function of t/τ_{rot}. The duration of the laser pulse is $\tau_{\mathrm{FWHM}} = 1$ ps and (a) $I_0 = 1 \times 10^{11}\mathrm{W/cm}^2$ and (b) $I_0 = 1 \times 10^{12}\mathrm{W/cm}^2$.

For DIB, the inter-J coupling due to quadrupole interaction noticeably influences the populations of rotational states during the pulse, where the dynamics shows nonadiabatic behavior. The alignment then starts to slightly deviate from the quadrupole-free results directly after the truncation of the laser field. By including the coupling, the strongest peak alignment was observed at the full revival $t = \tau_{\mathrm{rot}}$ with $\left\langle \cos^2\theta \right\rangle = 0.85$ (0.84) for I_2 (DIB), which is larger than the peak alignment obtained in the impulsive regime, see Figure 6.1 d, h. However, the enhancement of the post-pulse alignment by using truncated laser pulses instead of impulsive-kick pulses was much smaller than without the quadrupole interaction.

Post-pulse dynamics of excited rotational states While state-selected molecular beams [62, 70, 71, 177–180] or ultracold-molecules techniques [181, 182] can produce near-0 K samples, this is not generally feasible, especially not for the heavy organic molecules discussed here. Therefore, we investigated the impulsive-alignment dynamics for several initially excited states of I_2 and DIB. Since comparable results were obtained for both molecules, we focus our analysis on DIB, namely the rotational states $|J_{K_aK_c}, M_J\rangle = |3_{13}, 2\rangle$ and $|4_{40}, 0\rangle$. For both excited states, we observe a qualitatively similar influence of the quadrupole coupling as for the rotational ground state. For $I_0 = 1 \times 10^{11}\mathrm{W/cm}^2$, $\left\langle\cos^2\theta\right\rangle$ in Figure 6.3 a approaches 1/3 on timescales similar to the one in Figure 6.1 e. For the higher intensity $I_0 = 1 \times 10^{12}\mathrm{W/cm}^2$, we find a more significant decrease of the post-pulse alignment for the initial state with $J = 4, M_J = 0$, Figure 6.3 b than for the rotational ground state, Figure 6.1 h. This can be attributed to the populations of field-free eigenstates, which are shifted toward smaller values of J for $|4_{40}, 0\rangle$. However, for other excited states the impact of the quadrupole coupling for higher laser intensities can be smaller, as is the case for $|3_{13}2\rangle$. Thus, for a thermal ensemble of molecules, we expect a small influence of nuclear-quadrupole interactions on the post-pulse alignment induced by strong laser fields. However, to accurately describe the alignment the coupling cannot be fully neglected even in this regime. Furthermore, on longer timescales even small frequency shifts will lead to a significant decrease of the alignment [95].

6.4. Conclusions

In conclusion, a significant dephasing of rotational wave packets was observed in the post-pulse dynamics for different laser-field shapes and intensities. The influence on the degree of alignment is the largest if low-energy, small-J rotational states dominate the dynamics and diminishes for highly excited states. For initially excited rotational states, the quadrupole coupling has a similar effect on the post-pulse dynamics as for the rotational ground state, which we expect to hold for thermal ensembles as well. Adiabatic alignment is essentially not affected by the nuclear-quadrupole interactions.

Our results emphasize the need to take into account the nuclear-quadrupole interactions in the description of field-free alignment for molecules with heavy nuclei with large nuclear quadrupoles. Since many biomolecules include such heavy elements, we plan to investigate other molecular species and their properties including rotational constants and molecular symmetry in the context of nuclear-quadrupole interactions.

6.5. Supplementary Material

Molecular parameters

The rotational constant of I_2 was experimentally determined to $B_0 = 1118.63$ MHz [95]. For DIB, the rotational constants $B_z = A = 5712.768$ MHz, $B_y = B = 159.017$ MHz, and $B_x = C = 154.710$ MHz were obtained from a geometry optimization using density functional theory (DFT) with the B3LYP functional and the def2-QZVPP basis set [163, 164]; for the iodine atoms the effective core potential def2-ECP was used [165]. Due to the symmetry of DIB, the electric field gradient (EFG) tensors on the two iodine centers are equal to each other with nonzero elements only on the diagonal $V_{xx} = -5.5879$ a. u.,

$V_{yy} = -6.2295$ a. u. and $V_{zz} = 11.8174$ a. u.. The nuclear quadrupole moment for ^{127}I is $Q = -696$ mb [173]. For I_2, instead of computing the EFG tensors we used the experimental nuclear-quadrupole coupling constant $\chi_{zz} = eQV_{zz} = -2.45258$ GHz [183], with the elementary charge e. For both, I_2 and DIB, the polarizability tensor α_{ij} is diagonal in the inertial frame. For I_2, we used the values $\alpha_{xx} = \alpha_{yy} = 7.94$ Å^3 and $\alpha_{zz} = 13.96$ Å^3 [184]. For DIB, calculated values of $\alpha_{xx} = 11.307$ Å^3, $\alpha_{yy} = 16.676$ Å^3, and $\alpha_{zz} = 32.667$ Å^3 were used [7]. Calculations of the EFG and polarizability tensors for the DIB molecule were carried out at the DFT/B3LYP level of theory using the all-electron scalar relativistic Douglas-Kroll-Hess Hamiltonian [167] with the DKH-def2-TZVP basis set [168, 169]. All electronic structure calculations employed the quantum-chemistry package ORCA [171, 172].

Matrix representation of the Hamiltonian

To obtain the field-free spin-rotational wave functions, we solved the time-independent Schrödinger equation for the Hamiltonian H_{mol}. The matrix representation of H_{mol} was constructed in a symmetry-adapted coupled basis $|F, J, I, w\rangle$ of the rotational wave functions $|J, w\rangle$ and the nuclear-spin functions $|I\rangle$. Here, w represents additional rotational (pseudo) quantum numbers, such as K_a and K_c for DIB. For I_2, we take into account the symmetry requirement that J and I have to be either both even or both odd [176], while for DIB all combinations of basis states are allowed. The rotational states $|J, w\rangle$ were obtained as linear combinations of symmetric top functions by diagonalizing H_{rot}. The explicit expressions for the matrix elements of the quadrupole coupling Hamiltonian and various multipole Cartesian tensor operators can be found elsewhere [111, 112, 175]. To obtain the matrix representation of the interaction Hamiltonian, the matrix elements were first set up in the coupled basis [111] and then transformed to the field-free eigenbasis [175].

Spin-statistical weights of hyperfine states

To derive the weights of the iodine-spin-rotational wavefunctions of DIB, we made use of its molecular symmetry group $D_{2\text{h}}$, the corresponding character table can be found elsewhere [107]. Pure rotational states obey either A_g, $B_{1\text{g}}$, $B_{2\text{g}}$ or $B_{3\text{g}}$ symmetry, while the iodine nuclear-spin functions $|I\rangle$ obey A_g or $B_{1\text{u}}$ symmetry for I odd or even, respectively. This follows from the effect of symmetry operations $\hat{P}$ that involve a permutation of the iodine nuclei, $\hat{P}\,|I\rangle = (-1)^{I_1+I_2+I}\,|I\rangle$, yielding a sign change for even values of I. The representation generated by the hydrogen nuclear-spin functions was derived [107] as $7A_\text{g} \oplus 3B_{1\text{g}} \oplus 3B_{2\text{g}} \oplus 3B_{3\text{g}}$. We considered rotational states having either A_g ($|J_{K_aK_c}\rangle = |0_{00}\rangle$ and $|4_{40}\rangle$) or $B_{2\text{g}}$ ($|3_{13}\rangle$) symmetry. With the requirement that the total internal wavefunction has to be of $B_{1\text{g}}$ or $B_{1\text{u}}$ symmetry, we obtained weights of 7 (3) for even (odd) I for the former case, while for the latter all spin-rotational states have equal weights.

---

[7] For convenience and tradition, we specify polarizabilities in Å^3, which can easily be converted to SI units as 1Å$^3 = 10^6$ pm^3.

In the case of the diatomic I_2 molecule, there are no additional nuclear spins leading to degeneracies of the hyperfine levels. However, in the electronic and vibrational ground state considered here, states with J and I having opposite parities are forbidden due to the generalized symmetrization postulate [176].

7

Nuclear-quadrupole coupling effects in the laser induced alignment of different molecular species[8]

7.1. Introduction

The coupling of nuclear spins to overall angular momenta can have a significant influence on the rotational dynamics of molecules [86–94]. These effects are prominent in molecules containing heavy atoms such as Se, Br, I, Fe, Au, or Pt which show strong nuclear-quadrupole interactions. Such atoms are found in many biologically relevant molecules. Due to their large scattering cross sections, x-ray or electron diffractive imaging techniques [11, 17, 130, 131] are often used to determine the stuctures of such molecules. Here the prime goal is to measure intermediate configurations of the molecules during dynamical processes [14, 19, 20]. A key ingredient of these experiments is the laser alignment of molecules to increase the contrast and to obtain information directly in the molecular frame. To avoid perturbations due to the external fields, aligning molecules in field-free space is of high interest.

Field-free alignment relies on the preparation of rotational wave packets by means of nonresonant laser pulses [48]. These wave packets dephase and rephase periodically after the external fields are switched off and show revivals of the alignment. Typical pulse shapes range from short kick pulses [58, 60, 152] to truncated laser fields [42, 66–68] with long rising and short falling edges. The resulting revival structures are highly sensitive to the molecule's energy level structure. A detailed understanding of all degrees of freedom that couple significantly to the rotations is thus needed to accurately predict degrees of alignment.

A substantial impact of nuclear-quadrupole interactions on the field-free alignment of molecules was recently demonstrated experimentally [95]. The influence of these interactions on the alignment depends strongly on the laser field configuration and diminishes for strong laser field strengths populating highly excited spin-rotational states [175, 185]. Here, we investigate the nuclear-quadrupole coupling effects in the impulsive alignment of a variety of molecular species that differ strongly in their hyperfine and rotational energy level structures.

---

[8] This chapter is based on a draft of the manuscript: *Nuclear-quadrupole coupling effects in the laser induced alignment of different molecular species*, Linda V. Thesing, Andrey Yachmenev, Rosario González-Férez and Jochen Küpper, in preparation (2020). I contributed to the development of the computational code for the hyperfine energy levels and rotational dynamics, performed the calculations of the molecular energy levels, matrix elements as well as alignment, analyzed the data and contributed to writing the manuscript.

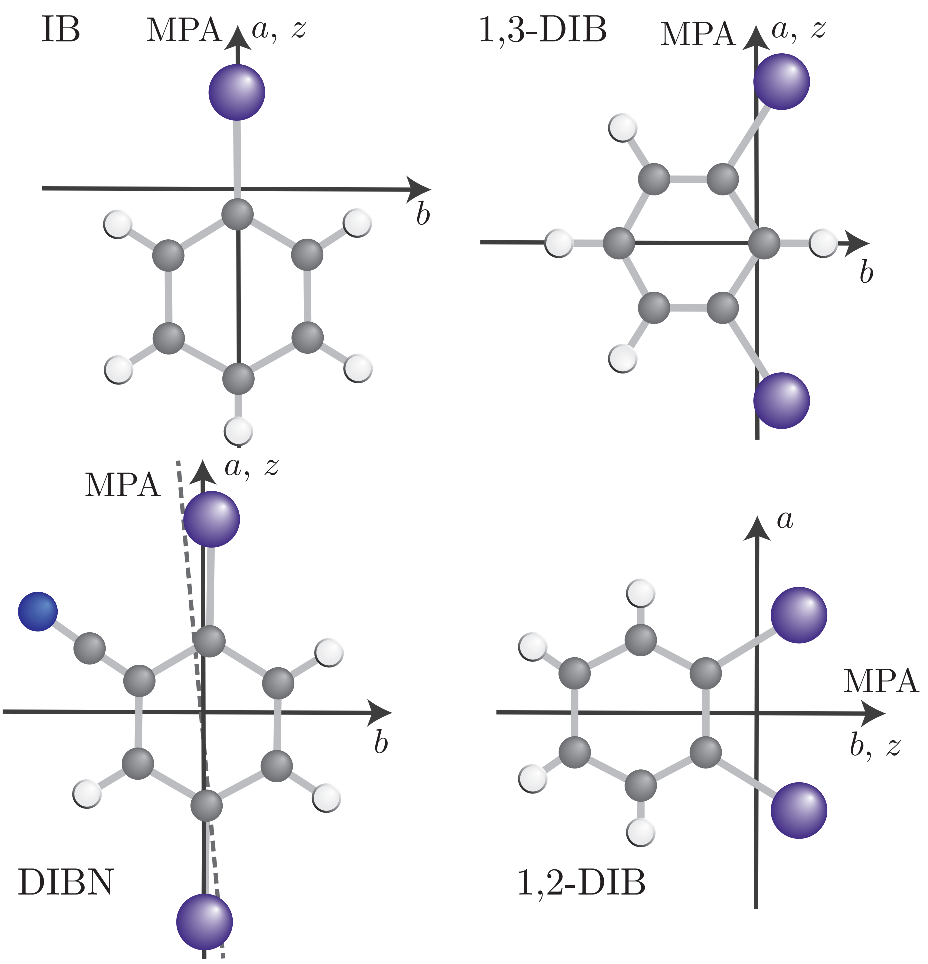

Figure 7.1.: Sketches of the molecules IB, DIBN, 1,3-DIB and 1,2-DIB. For IB and 1,3-DIBN the most polarizable axis (MPA) is parallel to the a axis, for DIBN it forms an angle of $5\,^\circ$ with the a axis and for 1,2-DIB the MPA is parallel to the b axis. The molecule-fixed z axis is indicated in the respective sketches.

7.2. Theoretical Description

We analyzed the rotational dynamics, induced by nonresonant laser fields, of asymmetric top molecules taking into account nuclear-quadrupole interactions. The theoretical description we employed has been presented before [175]. Briefly, the field-free Hamiltonian of the system is given by

$$H_{\text{mol}} = H_{\text{rot}} + \sum_{l} \mathbf{V}(l) \cdot \mathbf{Q}(l), \tag{7.1}$$

where $H_{\text{rot}} = A\hat{J}_a^2 + B\hat{J}_b^2 + C\hat{J}_c^2$ is the rigid-rotor Hamiltonian with the rotational constants A, B and C and the components $\hat{J}_i$, $i = a, b, c$, of the rotational angular momentum operator $\hat{\mathbf{J}}$. The second term in Equation 7.1 describes the coupling of the nuclear-quadrupole moment tensor $\mathbf{Q}(l)$ of the l-th nucleus with its electric field gradient (EFG) tensor $\mathbf{V}(l)$.

The interaction with the nonresonant, linearly-polarized laser field can be written as

$$H_{\mathrm{las}}(t) = -\frac{I(t)}{2\varepsilon_0 c}\alpha_{ZZ} \tag{7.2}$$

where $I(t)$ is the laser intensity and α_{ZZ} is the element of the polarizability tensor of the molecule along the laboratory-fixed Z axis which was chosen parallel to the polarization axis of the laser field.

We considered the molecules iodobenzene (IB), diiodobenzonitrile (DIBN), 1,3-diiodobenzene (1,3-DIB) and 1,2-diiodobenzene (1,2-DIB); see Figure 7.1. All four molecules possess ^{127}I nuclei which produce considerable hyperfine energy splittings due to their large quadrupole moments with $Q = -696$ mb [173]. IB has only one iodine nucleus and the total spin angular momentum is $\hat{\mathbf{I}} = \hat{\mathbf{I}}_1$, where $I_1 = 5/2$, while for the other molecules $\hat{\mathbf{I}} = \hat{\mathbf{I}}_1 + \hat{\mathbf{I}}_2$ and the associated quantum number can have values $I = 0, ..., 5$. The total angular momentum is given by $\hat{\mathbf{F}} = \hat{\mathbf{J}} + \hat{\mathbf{I}}$. The nitrogen nucleus in DIBN has an additional nonzero quadrupole moment, which is however small in comparison to the iodine quadrupole moment [173]. We thus neglected its contribution to the hyperfine interactions. The relevant molecular parameters are listed in section 7.7.

To study the field-dressed dynamics, we used the same computational setup as in our previous work [115, 175]. The time-dependent Schrödinger equation (TDSE) was solved for the full Hamiltonian $H(t) = H_{\mathrm{mol}} + H_{\mathrm{las}}(t)$ using the program RichMol [115]. We expanded the time-dependent wave function in a basis set consisting of the field-free eigenstates $\left|F, \tilde{J}_{\tilde{K}_a\tilde{K}_c}, n, M\right\rangle$ of H_{mol}, see section 7.7. The alignment is quantified by the expectation value $\left\langle\cos^2\theta\right\rangle$, where θ is the Euler angle between the laboratory-fixed Z axis and molecule-fixed z axis. The molecule-fixed frame is defined by the principle axes of inertia, see Figure 7.1 and section 7.7. We compare the post-pulse alignment with and without the nuclear-quadrupole interactions for a rotational temperature $\mathrm{T}_{\mathrm{rot}} = 0$ K and in the case of IB up to $\mathrm{T}_{\mathrm{rot}} = 0.3$ K. As initial states of the time-propagation we used field-free eigenstates of H_{rot} and H_{mol} for calculations with and without quadrupole coupling, respectively. When the coupling was taken into account, we assumed equal populations of different hyperfine levels corresponding to a given rotational state and averaged over the individual alignment results.

7.3. Weak Intensity Impulsive Alignment

Since the influence of the nuclear-quadrupole coupling is the strongest for wave packets consisting of low-energy rotational states [185], we begin by investigating how this coupling affects the impulsive alignment in the weak-intensity regime for the different molecules. We considered a laser pulse with a Gaussian envelope $I(t) = I_0 \exp\left(-4\ln 2t^2/\tau_{\mathrm{FWHM}}^2\right)$, where $\tau_{\mathrm{FWHM}} = 1$ ps and the peak intensity is $I_0 = 10^{11}$ W/cm^2. Figure 7.2 shows the temporal evolution of the post-pulse alignment dynamics induced by this laser pulse. For each molecule, $\left\langle\cos^2\theta\right\rangle$ is plotted both including (thick lines) and neglecting (thin lines) the nuclear-quadrupole interactions.

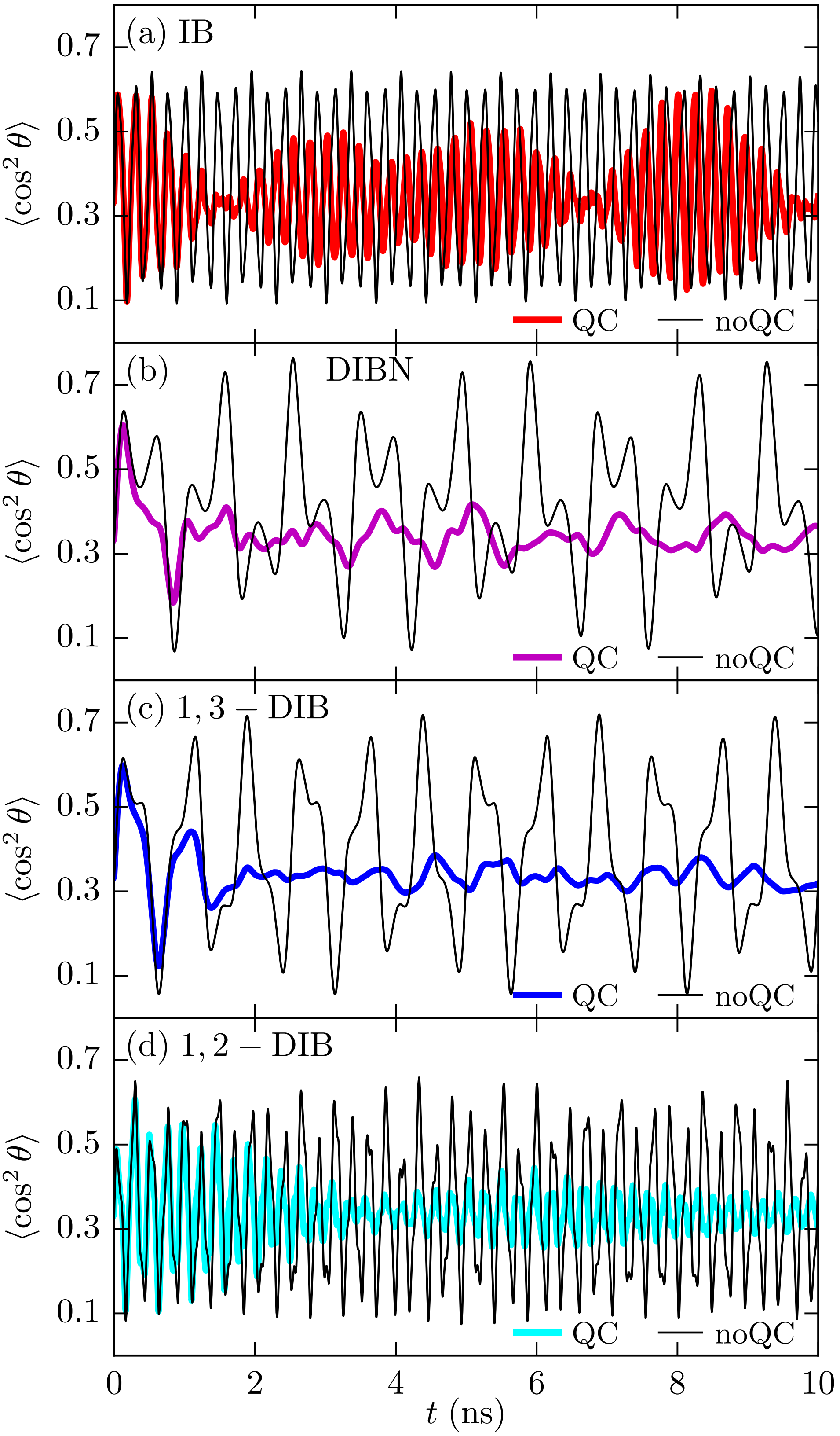

Figure 7.2.: Impulsive alignment induced by a Gaussian laser pulse with 1 ps and $I_0 = 10^{11}$ W/cm^2 for (a) IB, (b) DIBN, (c) 1,3-DIB and (d) 1,2-DIB including (QC) and neglecting the nuclear-quadrupole coupling (noQC).

Without this coupling, we observe revival patterns resulting from the dephasing and rephasing of the narrow rotational wave packets created by the laser field. These revival structures show strong variations among the different molecules, which are characteristic of their rotational energy level structures. The weak intensity post-pulse dynamics of IB, DIBN and 1,3-DIB is dominated by low-energy J-states with $K_a = 0$. Since the energies of these states can be approximated by symmetric top energy levels, the revival patterns in Figure 7.2 (a), (b) and (c) repeat themselves after multiples of the respective rotational periods $\tau_{\text{rot}}^{\text{IB}} = 707.69$ ps, $\tau_{\text{rot}}^{\text{DIBN}} = 3365.7$ ps and $\tau_{\text{rot}}^{\text{1,3-DIB}} = 2499.4$ ps, where $\tau_{\text{rot}} = 1/(B + C)$. In the case of 1,2-DIB, the post-pulse dynamics [Figure 7.2 (d)] does not show such a periodicity which can be attributed to the molecule's larger asymmetry leading to more irregular rotational energy splittings.

If the quadrupole coupling is included, the complexity of the post-pulse alignment dynamics increases. Initially after the pulse, $\left\langle\cos^2\theta\right\rangle$ with and without coupling behaves similarly for all molecules since this interaction is much weaker than the one with the laser field. Over time, however, we observe strong deviations of the alignment caused by a dephasing of the wave packets [185]. The discrepancy of the alignment with and without coupling is characteristic of the hyperfine structure of the low-energy rotational states dominating the respective dynamics. For IB, each rotational state splits into a maximum of 6 hyperfine levels (neglecting the M degeneracy) while we find up to 36 hyperfine components for the rotational states of the other molecules, which have two ^{127}I nuclei. For the molecules DIBN and 1,3-DIB, which have small B and C constants, small rotational energy level splittings enable a strong mixing of neighboring levels in the spin-rotational eigenstates. Here, the hyperfine eigenstates belonging to one rotational level have significant contributions of other J-states. This inter-J mixing also affects the rotational parts of the initial hyperfine states and thus adds to the differences of $\left\langle\cos^2\theta\right\rangle$ in Figure 7.2. As a consequence for DIBN and 1,3-DIB, the influence of the quadrupole interactions is detrimental already shortly after the laser pulse and practically no rephasing of the wave packet is observed in Figure 7.2 (b) and (d). For IB and 1,2-DIB on the other hand, $\left\langle\cos^2\theta\right\rangle$ oscillates in a similar manner with and without quadrupole coupling, but the amplitude in Figure 7.2 (a), (g) varies with time when the coupling is taken into account.

The time-dependent expectation value $\left\langle\cos^2\theta\right\rangle(t)$ is given by a sum of sinusoidal terms with frequencies that result from the energy differences between populated states with nonzero matrix elements of $\cos^2\theta$. To illustrate the interplay of the hyperfine levels and rotational energy gaps, we computed the fast fourier transforms (FFTs) of the post-pulse alignment of IB and 1,3-DIB for one initial eigenstate of each molecule, i. e., the state $\left|F, \tilde{J}_{\tilde{K}_a\tilde{K}_c}, n, M\right\rangle = \left|5/2, 0_{00}, 1, 1/2\right\rangle$ of IB and $\left|0, 0_{00}, 1, 0\right\rangle$ of 1,3-DIB. The FFTs are depicted in Figure 7.3 (c) and (d), respectively. The alignment dynamics of these states is additionally plotted in Figure 7.3 (a) and (b), together with $\left\langle\cos^2\theta\right\rangle$ neglecting the quadrupole coupling from Figure 7.2.

The fourier transforms without quadrupole coupling show a small number of peaks with regularly spacings which leads to the periodic behavior of $\left\langle\cos^2\theta\right\rangle$. For both molecules, the most significant frequency contribution originates from the energy gaps between the

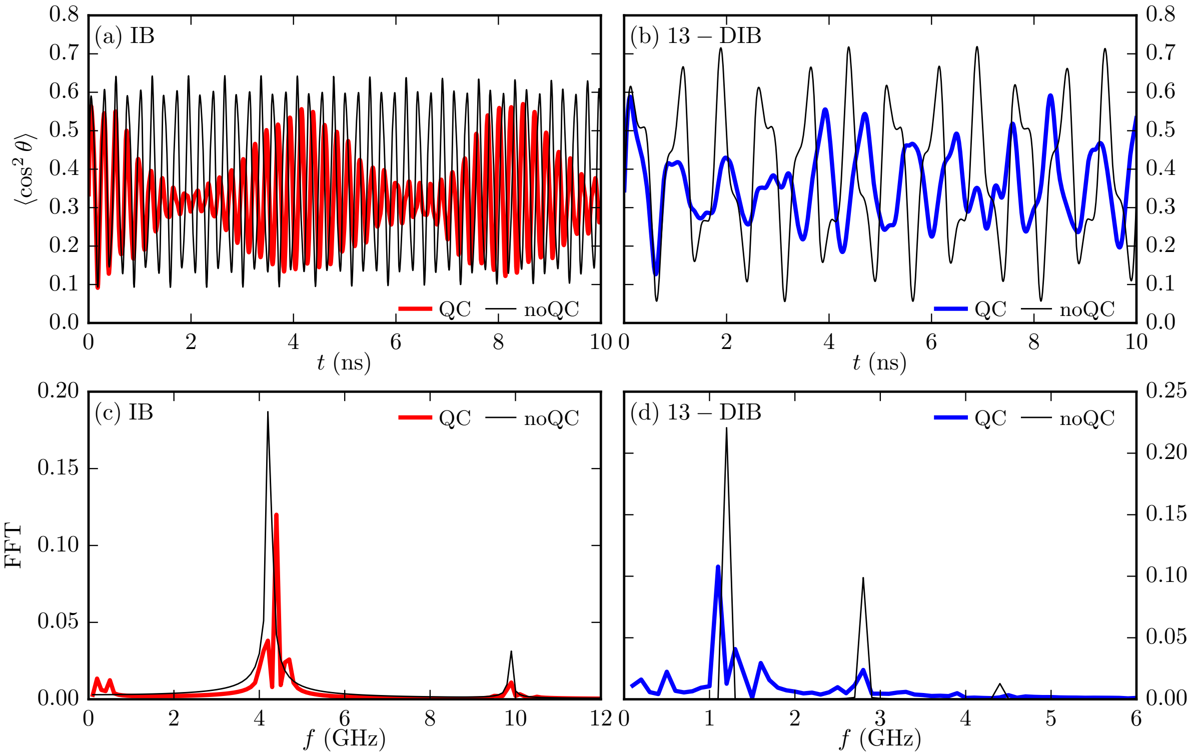

Figure 7.3.: Impulsive alignment for $I_0 = 10^{11}$ W/cm^2 with nuclear-quadrupole coupling (QC) for the initial states (a) $|5/2, 0_{00}, 1/2\rangle$ of IB and (b) $|0, 0_{00}, 0\rangle$ of 1,3-DIB and without coupling (noQC). (c),(d) Fast Fourier transform of $\langle\cos^2\theta\rangle$ with and without quadrupole coupling.

rigid-rotor states $|0_{00}, 0\rangle$ and $|2_{02}, 0\rangle$. With quadrupole coupling, these peaks are split into several frequencies corresponding to the energy gaps between different hyperfine levels. For IB [Figure 7.3 (c)], the the component at $f \approx 4.2$ GHz is shifted towards a higher frequency causing the faster oscillation of the alignment in Figure 7.3 (a) compared to the result without quadrupole coupling. In addition, the splitting of this peak results in a varying amplitude of $\langle\cos^2\theta\rangle$. For 1,3-DIB, the frequency shifts in Figure 7.3 (d) are of a similar magnitude as those for IB in Figure 7.3 (c). However, they are larger in relation to the frequencies without quadrupole interaction. The deviation of the post-pulse alignment thus occurs on the same timescale as the rotational revivals while the effect is slower for IB with respect to its rotational period. Furthermore, the larger number of hyperfine states increases the amount of significant frequency contributions. The irregular spacings of these components give rise to the non-periodic revival pattern in Figure 7.3 (b). Since other initial spin-rotational eigenstates behave analogously, revivals of $\langle\cos^2\theta\rangle$ are on average almost entirely suppressed, see Figure 7.2 (c). For both molecules, the frequency components below $f \approx 1$ GHz originate from the energy gaps between different hyperfine states belonging to the same rotational level. For other initial states as well as for the other two molecules, an analogous analysis can be made.

To gain more insight into the influence of the number of nuclear spins, we additionally computed $\langle\cos^2\theta\rangle$ for a modified 1,3-DIB molecule, where we only considered the quadrupole coupling of one iodine nucleus leaving all other properties of the molecule unchanged. This allows us to compare two molecular systems which differ only in the

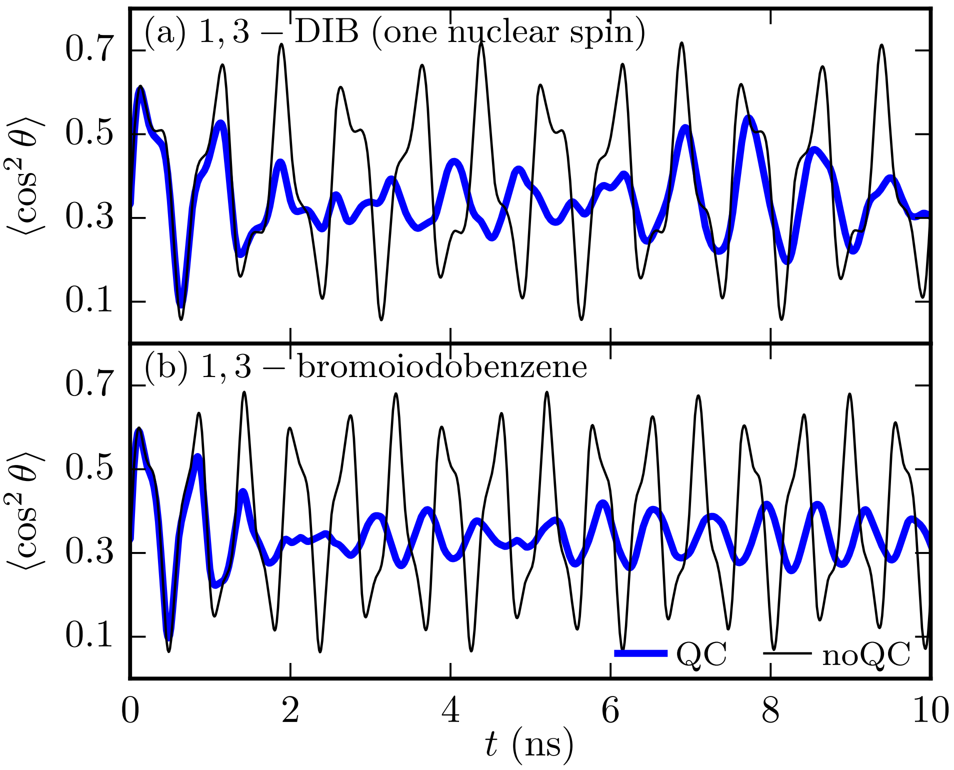

Figure 7.4.: Impulsive alignment induced by 1 ps laser pulses with $I_0 = 10^{11}$ W/cm^2 for (a) 1,3-DIB neglecting the quadrupole coupling of the second iodine nucleus and (b) 1,3-bromoiodobenzene including (QC) and neglecting the nuclear quadrupole coupling (noQC).

number of nuclei producing hyperfine splittings. The alignment of this modified 1,3-DIB [Figure 7.4 (a)] including the quadrupole coupling shows stronger revivals than for 1,3-DIB. However, the impact of the hyperfine interactions is still more pronounced than for IB even though the energy shifts due to nuclear spin interactions are similar. As the pure rotational energy gaps of IB are much larger than for 1,3-DIB, this implies that the relative difference of the hyperfine and rotational energy gaps plays a crucial role in the effect of the quadrupole coupling on the alignment dynamics. The rotational dynamics of 1,2-DIB further supports this conclusion, as this molecule has two iodine nuclei but $\left\langle\cos^2\theta\right\rangle$ is affected by the quadrupole interactions in a manner that qualitatively resembles the behavior of IB rather than 1,3-DIB, i. e., the peak alignment with quadrupole increases after several nanoseconds.

We further investigated the influence of the nuclear spins using the molecule 1,3-bromoiodobenzene, see section 7.7, which, like 1,3-DIB, has two nuclei with strong quadrupole coupling but fewer (up to 24) hyperfine levels for a given rotational level, due to the spin $I = 3/2$ of the bromine nucleus. The post-pulse alignment for this molecule with and without quadrupole interactions is depicted in Figure 7.4 (b). The rotational dynamics without quadrupole interactions is comparable to the one of 1,3-DIB due to their similar rotational constants. Here, the alignment is strongly influenced by the coupling as in the case of 1,3-DIB in Figure 7.2 (c). However, some low amplitude oscillations of $\left\langle\cos^2\theta\right\rangle$ can be observed. On the one hand this can be attributed to the smaller number of hyperfine states over which the alignment is averaged. On the other hand, the rotational energy gaps of 1,3-bromoiodobenzene are larger than the ones of 1,3-DIB while the hyperfine energy shifts are slightly smaller. This molecule thus represents and intermediate case between 1,3-DIB and the modified 1,3-DIB with one spin.

Apart from their rotational constants and the number of hyperfine levels, an important distinction of the molecules considered here lies in the symmetry of their EFG and polarizability tensors. In IB, both tensors are diagonal in the coordinate system defined by the principle axes of inertia while the EFG tensors of the other molecules and the polarizability tensor of DIBN have nonzero off-diagonal elements. The diagonal elements of these tensors couple rotational states having the same symmetry in the D_2 rotation group [106]. The off-diagonal elements α_{ab} and V_{ab} couple rotational states with A and B_c symmetry as well as B_a and B_b. For DIBN and the two diiodobenzene molecules, however, a given spin-rotational eigenstate of these molecules is a linear combination of basis states $|F, J_{K_aK_c}, I, M\rangle$ with A and B_c or B_a and B_b rotational symmetries. For a given eigenstate $\left|F, \tilde{J}_{\tilde{K}_a\tilde{K}_c}, n, M\right\rangle$, only an approximate rotational symmetry of an eigenstate can be assigned according to $\tilde{K}_a$ and $\tilde{K}_c$ being even or odd [106]. Consequently, a weak interaction due to the polarizability can be observed between the hyperfine states corresponding to rotational states of different symmetries even if the laser field does not couple the pure rotational levels neglecting quadrupole interactions.

Without quadrupole interactions, the wave packets of IB, 1,3-DIB and 1,2-DIB consist exclusively of rotational states having the same symmetry in the D_2 group as the initial state, i. e., A symmetry for $T_{\text{rot}} = 0$ K. For DIBN, states with B_c symmetry also contribute due to the polarizability tensor having nonzero off-diagonal elements. With quadrupole coupling, nonzero populations of B_c rotational states are observed for 1,3-DIB and 1,2-DIB as well. While these contributions are small here ($\lesssim 5$ %) and thus do not influence the alignment significantly, we point out that this aspect of the rotational dynamics is not captured if the nuclear-quadrupole interactions are neglected. In addition, for rotational levels which are strongly mixed by these interactions, a much larger impact on the population distribution is possible. This is, for instance, the case for the excited states $|2_{12}, M_J\rangle$ and $|2_{02}, M_J\rangle$ of 1,2-DIB, see section 7.5.

7.4. Strong Intensity Impulsive Alignment

Impulsive alignment experiments typically use laser pulses which populate a large number of highly-excited rotational states requiring larger intensities than the one in the previous section [62, 65, 161]. We thus increased the laser intensity in our calculations to $I_0 = 10^{12}$ W/cm^2. Here, the temporal behavior of $\left\langle\cos^2\theta\right\rangle$, see Figure 7.5, for all molecules except 1,2-DIB is characterized by J-type revivals [65, 174] which appear at multiples of the rotational periods and fractions thereof. These beatings originate from interferences of highly excited rotational states with $\Delta K_a = 0$. The asymmetry splittings of these states prevent a complete rephasing of the wave packet and the peak alignment at

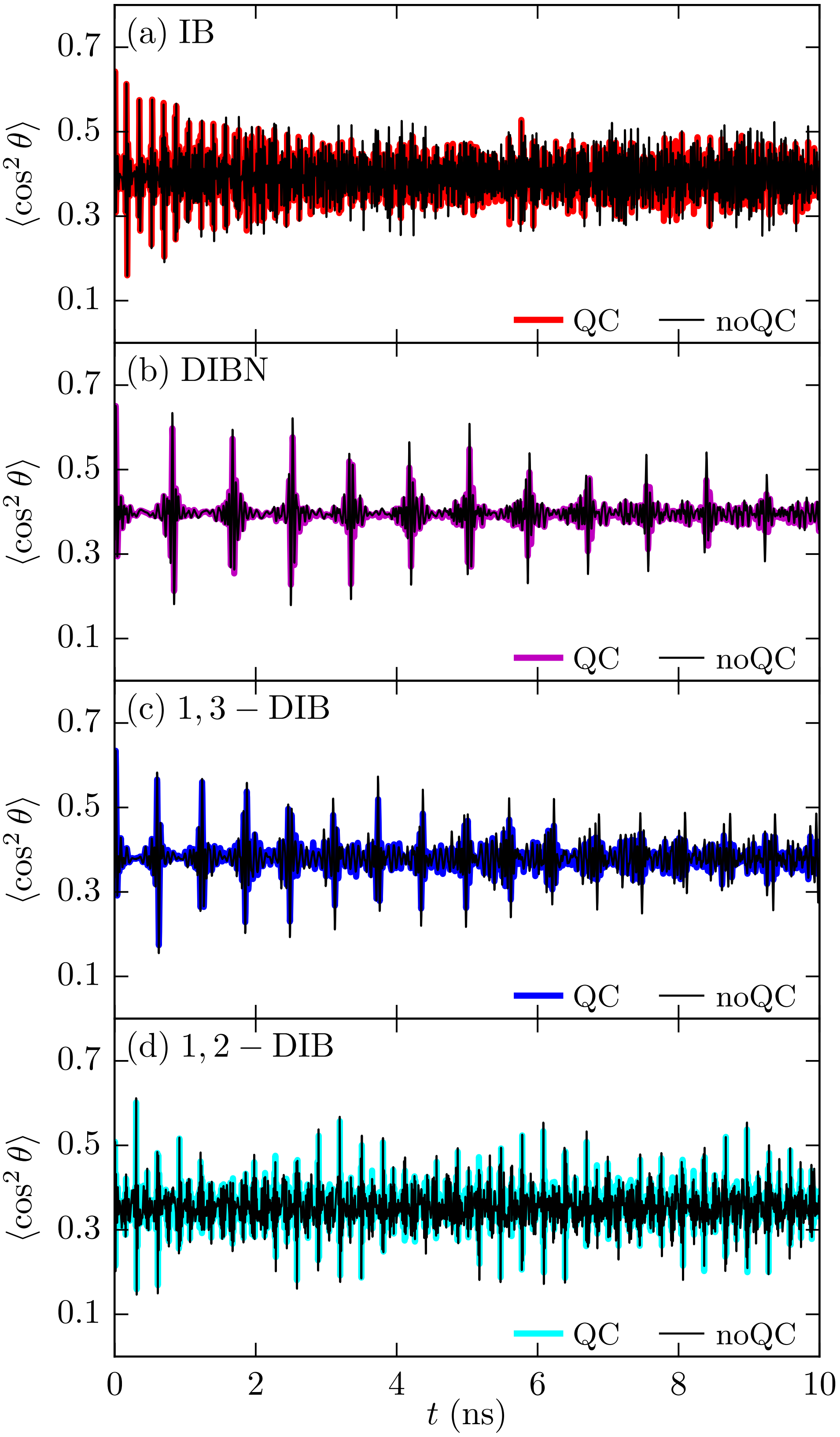

Figure 7.5.: Impulsive alignment induced by a Gaussian laser pulse with 1 ps and $I_0 = 10^{12}$ W/cm^2 for (a) IB, (b) DIBN, (c) 1,3-DIB and (d) 1,2-DIB including (QC) and neglecting the nuclear-quadrupole coupling (noQC).

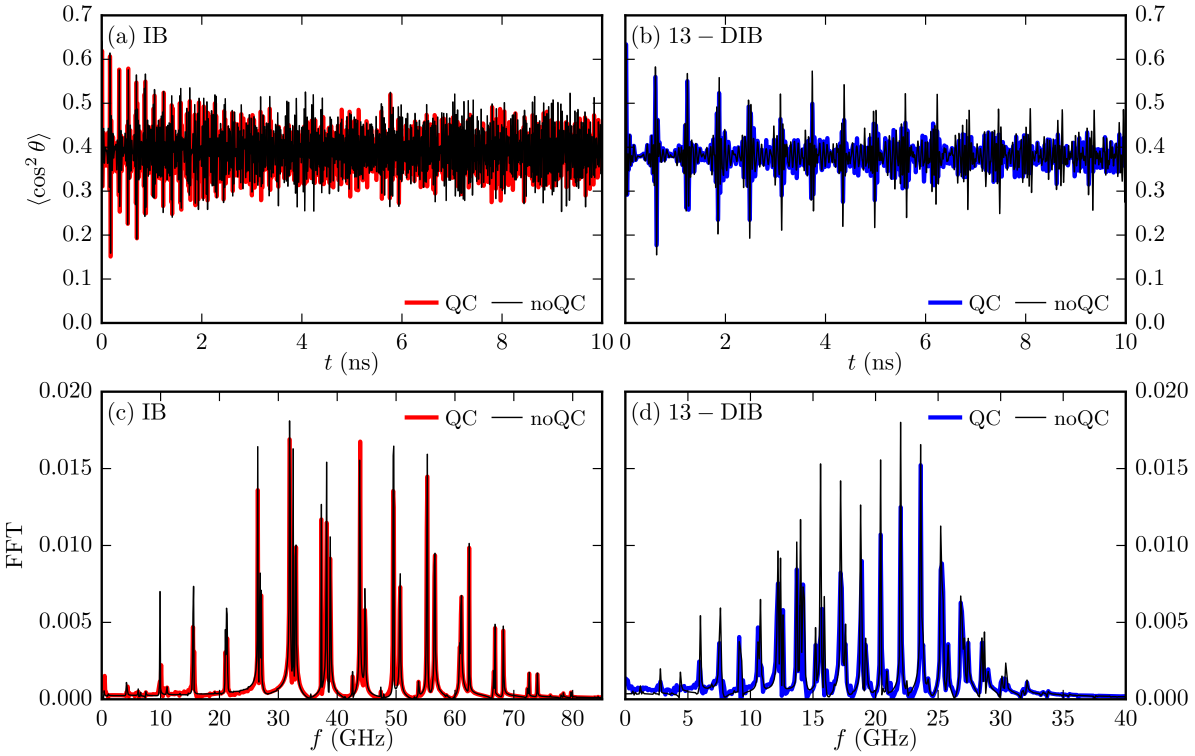

Figure 7.6.: Impulsive alignment for $I_0 = 10^{12}$ W/cm^2 with nuclear-quadrupole coupling (QC) for the initial states (a) $|5/2, 0_{00}, 1/2\rangle$ of IB and (b) $|0, 0_{00}, 0\rangle$ of 1,3-DIB and without coupling (noQC). (c),(d) Fast Fourier transform of $\langle\cos^2\theta\rangle$ with and without quadrupole coupling.

the revivals decreases over time [64]. For 1,2-DIB, we observe clear revival features of a different type spaced by 304 ps in Figure 7.5 (d). The post-pulse dynamics of this molecule is dominated by the dephasing and rephasing of rotational states with $\Delta J = \Delta K_a = 2$ and $J \approx K_a$. For large J, the energies of these states can be approximated by $E(J, K_a) \approx \overline{B}J(J+1) + (A - \overline{B})K_a^2$ with $\overline{B} = \frac{1}{2}(B + C)$. The relevant energy gaps are thus multiples of $4A$ yielding the period of $1/4A \approx 304$ ps in $\langle\cos^2\theta\rangle$.

For this stronger laser pulse, the nuclear-quadrupole interactions have a much weaker impact on the post-pulse alignment and generally lead to a loss of peak alignment over time instead of qualitatively altering the rotational dynamics [185]; see Figure 7.5. An exception of this destructive effect of the quadrupole coupling is found at certain alignment peaks of 1,2-DIB, e. g., $t = 5.17$ ns, where $\langle\cos^2\theta\rangle$ with coupling is slightly larger than without it. We attribute this "positive effect" of the quadrupole coupling to a modulation of the amplitude of $\langle\cos^2\theta\rangle$ due to some low-energy rotational states, similar to the change in the amplitude of $\langle\cos^2\theta\rangle$ for the smaller laser intensity [Figure 7.2 (c)]. The smaller impact of the quadrupole interactions for highly-excited rotational states is a result of increasingly uniform hyperfine splitting patterns [185]. The energy gaps between the levels with a significant coupling then resemble the pure rotational energy spacings.

As for $I_0 = 10^{11}$ W/cm^2, we computed the FFTs of the post-pulse alignment for IB and 1,3-DIB, shown in Figure 7.6 (c) and (d). Here, the broad wave packets of the molecules are reflected in the large number of frequency components in the respective FFTs. For both molecules, the fourier transforms with and without quadrupole interactions show

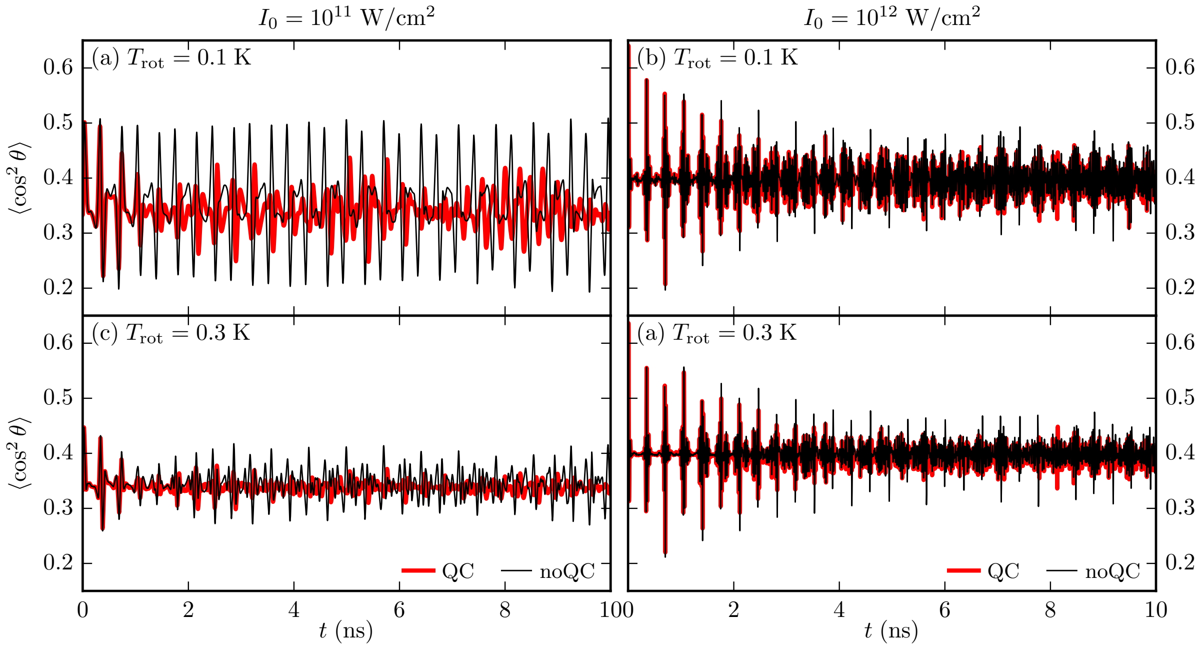

Figure 7.7.: Impulsive alignment of a thermal ensemble of IB molecules induced by laser pulses with $\tau_{\mathrm{FWHM}} = 1$ ps including and neglectin the quadrupole coupling (QC and noQC) for (a),(b) $\mathrm{T_{rot}} = 0.1$ K and (c),(d) $\mathrm{T_{rot}} = 0.3$ K The left panels show the results for $I_0 = 10^{11}$ W/cm^2 and the right panels for $I_0 = 10^{12}$ W/cm^2.

strong similarities, especially for large f corresponding to the energy gaps between highly-excited rotational states. Deviations occur mainly in the lower frequency regime and provoke the dephasing and thus the decrease of $\langle\cos^2\theta\rangle$ in Figure 7.6 (a) and (b) with respect to the result neglecting the coupling. As for the smaller laser intensity, this dephasing is more pronounced for 1,3-DIB due to the stronger mixing of neighboring rotational states and larger number of hyperfine states.

7.5. Influence of the temperature

In molecular beams of asymmetric top molecules, rotational temperatures of zero Kelvin are often not feasible. The effect of quadrupole interactions on thermal ensembles of molecules is thus of high interest. Here, we computed the thermal average of the post-pulse impulsive alignment of IB molecules for the two laser intensities used above and the rotational temperatures $\mathrm{T_{rot}} = 0.1$ K and $\mathrm{T_{rot}} = 0.3$ K. Such thermal ensembles are comparable [127] to state selected molecular ensembles [62, 70, 71, 177–180] and thus represent conditions that are experimentally within reach.

The thermal average of the post-pulse alignment is shown in Figure 7.7. Without quadrupole interactions, $\langle\cos^2\theta\rangle$ shows revival features with a decreased alignment compared to $\mathrm{T_{rot}} = 0$ K due to the influence of excited rotational states. As for $\mathrm{T_{rot}} = 0$ K, the influence of the quadrupole coupling is stronger for the low-energy rotational states in the weak field spin-rotational wave packets; see Figure 7.7 (a) and (c). For this laser intensity, an increase in the amplitude of $\langle\cos^2\theta\rangle$ as in Figure 7.2 (a) is,

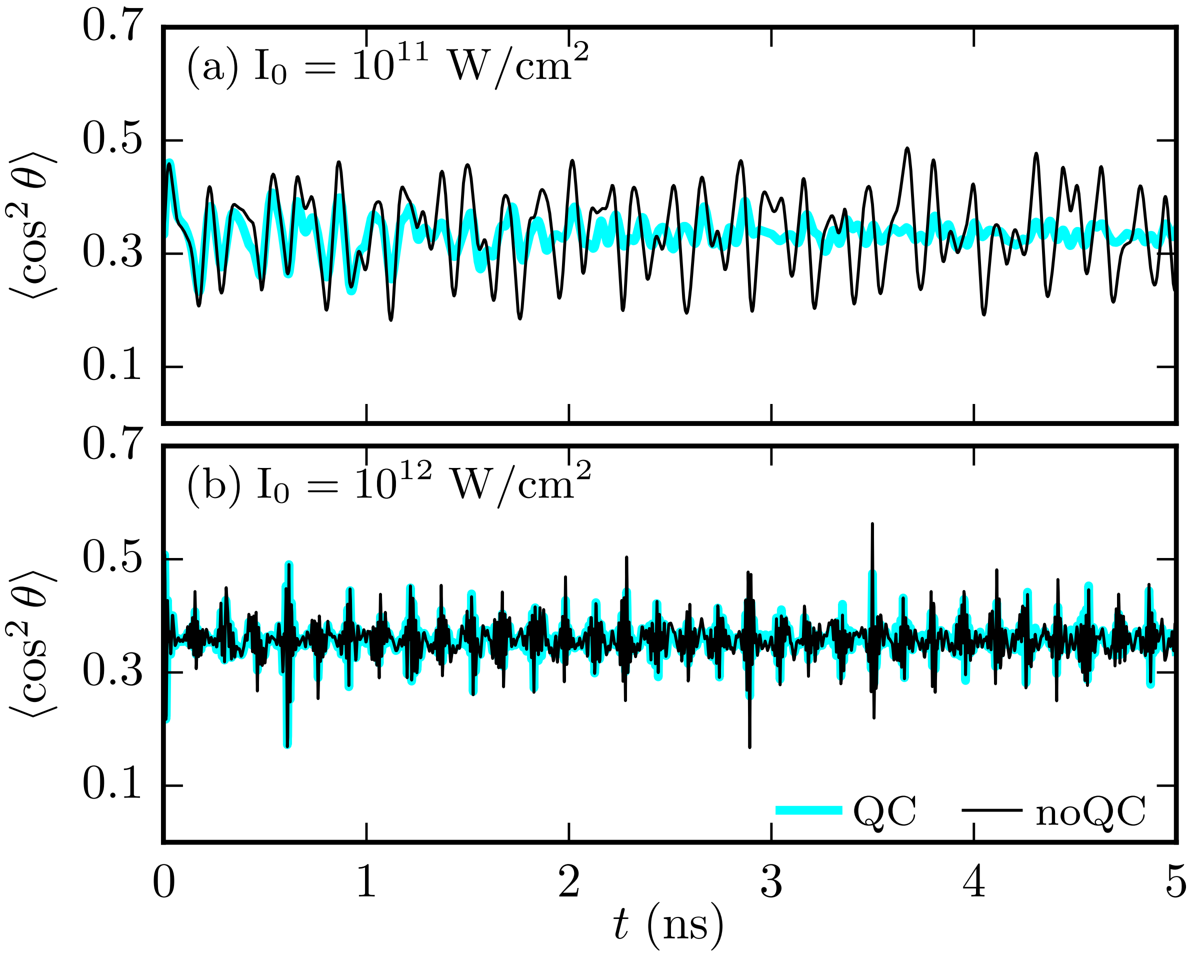

Figure 7.8.: Impulsive alignment averaged over the initial states $|2_{12}, M_J\rangle$ of 12-DIB induced by 1 ps laser pulses with (a) $I_0 = 10^{11}$ W/cm^2, (b) $I_0 = 10^{12}$ W/cm^2. The alignment is shown including (QC) and neglecting the nuclear quadrupole coupling (noQC).

however, not observed at higher temperature thermal ensembles. For $I_0 = 10^{12}$ W/cm^2, the quadrupole coupling essentially does not alter the alignment of the thermal ensembles during the first rotational period after the laser pulse [Figure 7.7 (b) and (d)], similar to $T_{\text{rot}} = 0$ K while for longer times, it cannot be neglected.

To account for the different molecular species, we additionally computed the alignment dynamics of the excited states $|2_{12}, M_J\rangle$ of 1,2-DIB; see Figure 7.8. To compare the results with and without quadrupole coupling, we computed the average rigid-rotor alignment over all possible M_J values of the initial state and the average result obtained from all hyperfine states belonging to $|2_{12}, M_J\rangle$. As for the rotational ground state, the alignment taking into account the quadrupole coupling deviates more strongly from the quadrupole coupling-free alignment when the weaker laser field is used. The influence of the coupling for the strong laser field [Figure 7.8 (b)] is, however, more pronounced than in Figure 7.2 (h). This is attributed to the strong mixing of the rotational levels $|2_{12}, M_J\rangle$ and $|2_{02}, M_J\rangle$ by the nuclear-quadrupole interactions. This mixing led to different rotational parts of the initial wave functions when the coupling is included than when it is neglected. As a result, we find significant populations of hyperfine states belonging to rotational levels that do not contribute to the rotational dynamics without quadrupole coupling. We thus conclude that the influence of nuclear-quadrupole interactions generally decreases with increasing laser intensity. These interactions cannot, however, be fully neglected even on a time scale where they do not affect the alignment for $T_{\mathrm{rot}} = 0$ K.

7.6. Summary and Conclusions

We presented a theoretical analysis of the post-pulse alignment of asymmetric top molecules showing strong nuclear-quadrupole interactions. Our work was focused on differences in the hyperfine energy level structures of the molecular species. We showed that the interplay of hyperfine energy shifts and rotational energy level spacings is a deciding factor for the extent to which the coupling affects the post-pulse alignment. For all molecules analyzed in the present work as well as previous studies [175, 185], we observed that the influence of the quadrupole coupling diminishes when the field-dressed dynamics is dominated by excited rotational states. Due to the variety of molecules considered, we conclude that this observation is a general one and creating wave packets of highly-excited rotational states is advantageous to minimize the dephasing due to nuclear-quadrupole coupling.

While nuclear-quadrupole interactions pose difficulties in achieving strong field-free alignment, their effect on the rotational dynamics might be exploited to probe nuclear or electronic excitations which alter the nuclear spins and quadrupole momenta as well as electric field gradients. The sensitivity of the alignment to the hyperfine energy level structures of low-energy rotational states may thus be viewed as an opportunity rather than a disadvantage.

7.7. Supplementary material

Molecular parameters

The rotational constants, asymmetry parameters $\kappa = (2B - A - C)/(A - C)$ and elements of the polarizability and EFG tensors of the iodine nuclei in the principle axes of inertia frame are listed in Table 7.1. Except for IB, the rotational constants were computed from the equilibrium geometry obtained using density functional theory (DFT) with the B3LYP functional and the def2-QZVPP basis set [163, 164]. The effective core potential def2-ECP [165] was uesd for the iodine atoms. The electric field gradient and polarizability tensors of DIBN, 1,3-DIB and 1,2-DIB were calculated at the DFT/B3LYP level of theory using the all-electron scalar relativistic Douglas-Kroll-Hess Hamiltonian [167] with the DKH-def2-TZVP basis set [168, 169]. All electronic structure calculations were carried out with the quantum-chemistry package ORCA [171, 172]. For IB, we used the experimental nuclear-quadrupole coupling constants [186] $\chi_{aa} = -1892.039$ MHz, $\chi_{bb} = 978.816$ MHz, $\chi_{cc} = 913.222$ MHz instead of a calculated electric field gradient and quadrupole moment.

	IB	DIBN	1,3-DIB	1,2-DIB
A (MHz)	5669.131 [186]	1608.324	1859.912	822.0850
B (MHz)	750.414293 [186]	155.402	210.776	522.1492
C (MHz)	662.636146 [186]	141.709	189.321	319.3276
κ	-0.965	-0.981	-0.974	-0.193
α_{aa} (Å^3)	21.5 [174]	34.506	28.847	22.072
α_{bb} (Å^3)	15.3 [174]	21.662	19.789	24.830
α_{cc} (Å^3)	10.2 [174]	12.123	11.292	11.103
α_{ab} (Å^3)	0	-1.209	0	0
$V_{aa}(1)$ (a.u.)	see text	12.327	7.34	-0.30
$V_{bb}(1)$ (a.u.)	see text	-6.6802	-1.73	5.88
$V_{cc}(1)$ (a.u.)	see text	-5.6472	-5.61	-5.57
$V_{ab}(1)$ (a.u.)	0	1.5092	-7.85	8.84
$V_{aa}(2)$ (a.u.)	-	12.155	7.34	-0.30
$V_{bb}(2)$ (a.u.)	-	-6.4317	-1.73	5.88
$V_{cc}(2)$ (a.u.)	-	-5.7230	-5.61	-5.57
$V_{ab}(2)$ (a.u.)	-	0.57071	7.85	-8.84

Table 7.1.: Rotational constants A, B, C, asymmetry parameter κ, elements of the polarizability tensors α_{ij} and electric field gradient tensors $V_{ij}(l)$ of the lth iodine nucleus in the coordinate system defined by the principle axes of inertia.

For 1,3-bromoiodobenzene, we computed the rotational constants $A = 2040.244$ MHz, $B = 281.807$ MHz and $C = 247.607$ MHz, EFG and polarizability tensors using the *ab initio* methods described above. The nonzero elements of the EFG tensor are $V_{aa}^{\mathrm{I}} = 8.3735$ a. u., $V_{ab}^{\mathrm{I}} = -7.1745$ a. u., $V_{bb}^{\mathrm{I}} = -2.7590$ a. u. and $V_{cc}^{\mathrm{I}} = -5.6146$ a. u. for the iodine nucleus and $V_{aa}^{\mathrm{Br}} = 4.1656$ a. u., $V_{ab}^{\mathrm{Br}} = 5.6800$ a. u., $V_{bb}^{\mathrm{Br}} = -0.4784$ a. u. and $V_{cc}^{\mathrm{Br}} = -3.6872$ a. u. for the bromine nucleus. For the polarizability tensor we obtained $\alpha_{aa} = 25.774$ Å^3, $\alpha_{ab} = -0.419$ Å^3, $\alpha_{bb} = 18.234$ Å^3 and $\alpha_{cc} = 10.192$ Å^3. The quadrupole moment of ^{79}Br is [173] $Q = 313$ mb. The molecule-fixed frame (x, y, z) is defined by the principle axes of inertia so that the z axis is parallel to the most polarizable axis or, in the case of DIBN, forms the smallest possible angle ($\approx 5°$) with it. The z axis is thus chosen parallel to the a axis for IB, DIBN, 1,3-DIB and 1,3-bromoiodobenzene and to the b axis for 1,2-DIB.

Matrix representation of the Hamiltonian

To obtain the eigenstates of H_{mol}, we first solved the time-independent Schrödinger equation for H_{rot} yielding the rigid-rotor energy levels and eigenstates $|J_{K_aK_c}, M_J\rangle$. Here, M_J is the eigenvalue of $\hat{J}_Z$ and $K_{a,c}$ are associated with the projections $\hat{J}_{a,c}$ and are good quantum numbers in the prolate and oblate symmetric top cases, respectively. The matrix representation of H_{mol} was then constructed in the coupled basis [111, 112] $|F, J_{K_aK_c}, I, M\rangle$, M being the eigenvalue of $\hat{F}_Z$. The field-free energies and eigenstates $\left|F, \tilde{J}_{\tilde{K}_a\tilde{K}_c}, n, M\right\rangle$ were computed by numerically solving the associated time-independent

Schrödinger equation. Here, $n = 1, 2, ...$ is an index labeling states with the same F and the approximate quantum numbers $\tilde{J}$, $\tilde{K}_a$ and $\tilde{K}_c$ were assigned according to the coupled basis state $|F, J_{K_aK_c}, I, M\rangle$ with the largest contribution to the given eigenstate. For IB, the nuclear spin quantum number $I = I_1$ remains a good quantum number. The matrix elements of the polarizability element α_{ZZ} are known analytically [111] in the basis $|F, J_{K_aK_c}, I, M\rangle$ and can be transformed easily into the field-free eigenbasis [175].

8 Conclusions and Outlook

8.1. Summary and Conclusions

The main objective of this thesis was to investigate the alignment and orientation of complex molecules in external electric fields. It extends previous work, which largely relied on the the rigid-rotor approximation or was limited to highly symmetric systems. In this work, the rotational dynamics of molecules having low rotational symmetry was analyzed and the influence of additional angular momenta, which are coupled to the rotations, was investigated.

In chapter 3, a time-dependent analysis of the rotational dynamics of a molecule without rotational symmetry, 6-chloropyridazine-3-carbonitrile, in tilted ac and dc electric fields was presented. The mixed-field orientation of this molecule had previously been measured and analyzed within the adiabatic picture [54], however, the experimentally observed behavior could not be reproduced. Using a time-dependent description, the orientation results in chapter 3 agree quantitatively with the experiment. It was shown that the high degree of nonadiabaticity in the field-dressed rotational dynamics causes the discrepancy between the experiment and adiabatic calculations. Furthermore an enhanced directional control of excited rotational states by applying strong dc fields was demonstrated.

Next, the influence of internal rotations on the mixed-field orientation of weakly-bound molecular aggregates was studied using the prototypical indole(H_2O) cluster as an example; see chapter 4. It was demonstrated that the torsion of the attached water molecule essentially leaves the overall rotational dynamics unaffected under typical experimental conditions. By exploring regimes of field-induced coupling, determined by the laser-field strength and the dependence of the polarizability on the torsional angle, it was shown that the rigid-rotor approximation can be applied for a wide range of field configurations, provided the energy spacings between ground and excited torsional states are considerably larger than the rotational energy gaps.

Chapters 5–7 focused on the effect of nuclear-quadrupole interactions on the laser alignment of linear and asymmetric top molecules. In chapter 5, the theoretical model to describe these interactions was presented and a strong influence of the quadrupole coupling on the impulsive alignment of the asymmetric top molecule CFClBrI was demonstrated. Next, the impact of this coupling for different laser-field strengths and pulse shapes (chapter 6) was systematically analyzed and it was analyzed how different properties of the molecules play a role in the field-dressed dynamics including hyperfine interactions (chapter 7). Alignment in the presence of laser fields, e. g., adiabatic alignment, is not affected by the quadrupole interactions, which are much weaker than the molecule's interaction with these fields. However, in the post-pulse rotational dynamics induced by short laser pulses or truncated ones, a dephasing of the wave packets was observed. Over time, this dephasing leads to a decrease of the alignment at the revivals. The magnitude of the hyperfine shifts in relation to rotational energy gaps was shown to be a deciding factor for the degree to which the alignment is modified by the quadrupole coupling. In all the systems considered here, the influence of the nuclear-quadrupole interactions is minimized when the rotational wave packets are dominated by highly-excited states. The analysis of the alignment dynamics for excited initial rotational states as well as for thermal ensembles of iodobenzene molecules showed that these observations can be extended to nonzero rotational temperatures. To avoid the detrimental effect of the quadrupole coupling, it is thus generally desirable to excite high-lying J-states in molecules with nuclei that have large quadrupole moments. In asymmetric top molecules, which show an additional dephasing of field-free rotational wave packets due to their complex energy level structures, a promising strategy to achieve strong field-free alignment is given by truncated laser pulses. If the alignment decreases more slowly than the laser field strength, this initial field-free alignment may be useful as it is not affected by quadrupole interactions during several picoseconds.

During my thesis work, I optimized a previously developed computer program to describe the rotational dynamics of rigid molecules for certain field configurations. Furthermore, I contributed to the development of the software package CMI-richmol which can be used to carry out a wide range of calculations such as the ones performed in this work. In section 2.6, the numerical methods are summarized and several example calculations are illustrated in Appendix A. More detailed descriptions of individual parts of CMI-richmol can be found in [115] as well as chapter 4 and chapter 5. Our computational approach is in principle capable of treating a wide variety of scenarios beyond the ones considered in this work. However, the increasing computational cost for large basis sets may require optimization of the computational code including careful symmetry considerations.

8.2. Outlook

In many biological systems, the molecules of interest display one or several of the effects considered in this thesis, i. e., they are generally floppy and may show significant nuclear-spin interactions. Studying molecules with both internal rotors and strong nuclear-quadrupole interactions would thus be a natural extension of the work presented here. Regarding internal motions in molecules, extending our approach to systems showing several large amplitude motions is of strong interest. Examples of such systems include larger molecule-solvent clusters or even indole(H_2O) if all internal motions of the water moiety are taken into account. In the limit of only one internal mode, it remains to be studied how field-free alignment is influenced, e. g., by the torsion of the water molecule in indole(H_2O), since the revival structures are sensitive even to small energy shifts.

In this thesis, only the effect of the nuclear-quadrupole coupling on the alignment of molecules has been considered. Thus, it remains to be studied how molecular orientation is influenced by this coupling. While nuclear-quadrupole interactions generally hinder field-free alignment techniques, the sensitivity of the revival structures to the hyperfine energy shifts of the molecules may be exploited in other ways. Since electronic or nuclear excitations affect the electric-field gradients and nuclear-quadrupole moments and spins, such excitations could in principle be probed by changes in the rotational dynamics of the molecules.

In recent years, novel techniques for the rotational control of molecules have gained interest, among them optical centrifuges [187, 188]. These tailored electric fields are strong nonresonant linearly polarized laser pulses where the polarization axis shows an accelerated rotation about the propagation axis. Subjecting molecules to these laser pulses allows one to align them along the polarization axes and force them to follow the accelerating rotation of the electric field. This way molecules can be prepared in highly excited rotational states, so-called super-rotor states [189, 190]. Using this technique, field-free three-dimensional alignment was recently achieved for the asymmetric top molecule SO_2 [191, 192]. Here, the rotational dynamics was constrained to the polarization plane of the optical centrifuge even after the field is switched off, effectively reducing it to the dynamics of a linear rotor. The molecules then exhibited periodic alignment revivals in field-free space. In another study, it was shown that the axis about which the molecule rotates can be controlled by modifying the envelope of the optical centrifuge [193]. Optimal application of optical centrifuges requires an accurate theoretical understanding to guide the choice of experimental parameters.

Appendices

A CMI-richmol calculation examples

Here, a short description of each part of the CMI-richmol package and the input scripts for several example calculations are presented. For more details, the reader is referred to the user-guide and documentation of the code.

A.1. Watie

The subpackage Watie is used to numerically solve the TISE for the rigid-rotor Hamiltonian (2.2) and to compute matrix elements of tensor operators in the field-free rigid-rotor basis. The parameters of the molecule, including rotational constants, elements of, e. g., electric-dipole moment or polarizability tensors, the molecular symmetry group and the molecular frame, are defined in the Python class `Molecule`. After setting the parameters of the molecule, the Python function `solve` (provided in the `solve` module) is used to construct the matrix representation of the Hamiltonian and to numerically solve the TISE by diagonalizing the resulting matrix. The energy levels are stored in a file `<molelcule name>_energies_j<jmin>_j<jmax>.rchm` which can be read by RichMol and HyPy, see section A.3 and section A.4. If properties like electric-dipole moment or polarizability are defined, the matrix elements of these tensors are computed in the basis of rotational eigenstates (see Equation 2.12 and Equation 2.14) obtained in the previous step. The results are saved in files `<molelcule name>_matelem_<tensor name>_j1<j1>_j2<j2>.rchm`, in the format used by RichMol, see section A.4. Calculations are carried out using the script `watie`:

```
watie <input file name>
```

A.1.1. Iodobenzene

In this example, the rigid-rotor energy levels of the molecule iodobenzene are calculated up to a maximum angular momentum quantum number $J = 25$. The matrix elements of the electric-dipole moment, polarizability and quadrupole coupling tensor as well as the operator $P_2^0(\cos\theta) = \frac{1}{2}(3\cos^2\theta - 1)$ are also computed.

Input

```
# initialize molecule
IB = Molecule()

# set rotational constants
```

```
IB.ABC = (5669.131*MHz, 750.414293*MHz, 662.636146*MHz)

# set dipole moment
mu_a=1.625*DEBYE_TO_AU
IB.dipole = ["x", mu_a, "y", 0.000, "z", 0.00]

# set polarizability
a_bb=15.3/BOHR_TO_ANGSTROM**3.0
a_cc=10.2/BOHR_TO_ANGSTROM**3.0
a_aa=21.5/BOHR_TO_ANGSTROM**3.0
IB.polariz = [ "xx", a_aa, "yy", a_bb, "zz", a_cc]

# set quadrupole coupling tensor
# (=electric field gradient * quadrupole moment)
Chi_aa=-1892.039*MHz
Chi_bb=978.816*MHz
Chi_cc=913.222*MHz
IB.elfieldgrad = [ "xx", Chi_aa, "yy", Chi_bb, "zz", Chi_cc]

#set alignment observable
IB.observable = "P20"

# set molecular frame axes; here: z corresponds to the a-axis,
# x to the b-axis, and y to the c-axis
IB.frame = "xyz=bca,pas"

# set symmetry group (default is "D2")
#IB.sym = "C2v"

# calculate energy and matrix elements
solve(IB, jmax=25)
```

A.1.2. OCS

Here, the rigid-rotor energies and matrix elements of the electric-dipole moment, polarizability and the operators $P_2^0(\cos\theta) = \frac{1}{2}(3\cos^2\theta - 1)$ and $\cos\theta$ are computed for the OCS molecule.

Input

```
OCS = Molecule()

#set rotational constant
B0 = 6081.0*MHz
OCS.ABC = (B0, B0, 0.0)
```

```
#set dipole moment
OCS.dipole = ["x", 0.00, "y", 0.000, "z", 0.71*DEBYE_TO_AU]

#set polarizability
a_xx=0.0
a_yy=0.0
a_zz=4.04/BOHR_TO_ANGSTROM**3.0 #=polarizability anisotropy

OCS.polariz = [ "xx", a_xx, "yy", a_yy, "zz", a_zz]

OCS.frame = "xyz=abc,pas"

OCS.observable = "P20"

OCS.observable = "costheta"

solve(OCS, jmax=25)
```

A.2. libtrove

The Fortran program libtrove is used to calculate rovibrational energy levels and matrix elements taking into account one internal mode, e. g., internal rotation. A Python interface is provided to allow for a user-friendly usage. In the input file, the basis sets for the rotational and vibrational degrees of freedom are defined as well the expansion coefficients for the internal coordinates and one-dimensional electric-dipole moment and polarizability surfaces. These parameters are define in the Python class `Calculation`. After setting them, the function `run`, included in the `Calculation` class, is used to start the Fortran program which carries out the calculation of the energy levels and matrix elements. As for Watie, the results are stored in files which can directly be used by RichMol, see section A.4. The script `libtrove` is used to perform a calculation:

```
libtrove <input file name>
```

The following two examples are calculations of the rotation-torsional energy levels of indole(H_2O) as well as matrix elements to reproduce the mixed-field orientation results in chapter 4.

A.2.1. Indole-water

The parameters for indole(H_2O), which were used in chapter 4, are provided in libtrove. These include the expansion coefficients for the structural parameters, dipole moment and polarizability tensor. By default, a vibrational basis set consisting of sine and cosine functions is used; see chapter 4. The matrix elements of the dipole moment, polarizability and the operators $\cos\theta$, $\cos^2\theta$, $\cos^2\tau$ are automatically calculated. The maximum value of J is set to 25. Since the parameters for this molecule are provided in libtrove, only a simple input file is required.

Input

```
# initialize calculation
calc=Calculation(mol="indole_water")

# set maximum and minimum value of J
calc.jmax = 25
calc.jmin = 0

# run calculation of energies and matrix elements
calc.run()
```

A.2.2. Indole-water with modified polarizability

Here, the expansion coefficient for the polarizability are set manually. The torsional basis is also set manually (here using default parameters) and $J_{\text{max}} = 40$.

Input

```
# initialize calculation
calc=Calculation(name="indole_water_modified_pol",
    mol="indole_water")

# set vibrational basis as well as maximum
# and minimum value of J
calc.vibbas = {"vmax":80,"emax":400,"npoints":151,"type":"exp"
    ,"bounds":[0,2.0*np.pi]}

calc.jmax = 40
calc.jmin = 0

# set polarizability coefficients
alpha = [[9.88163856156046E+01, 0.00, 5.653242E+01,
    -9.156292, 0.00, 1.935136E+02],
    [0,0,0,0,0,0],
    [-2.35024E+01, 0.0, 4.902866E+01,
    -7.791074E+01,  0.0, 4.757616E+01]]

calc.polariz = alpha

# run calculation of energies and matrix elements
calc.run()
```

A.3. HyPy

With the subpackage HyPy, the hyperfine energy levels of molecules are computed taking into account nuclear quadrupole interactions. Matrix elements in the spin-rotational eigenbasis can be calculated as well. HyPy requires rigid-rotor or rovibrational energy levels produced, e. g., by Watie or TROVE [114]. Addtionally, if matrix elements of electric-dipole moment, polarizability or operators like $P_2^0(\cos\theta) = \frac{1}{2}(3\cos^2\theta - 1)$ are to be computed, the rigid-rotor matrix elements of these tensor need to be provided. There are separate Python classes for each of these operators based on a general Cartesian tensor class. Tensors are initialized with functions like, for instance, `init_polariz` for the polarizability. To perform a calculation, the function `solve`, provided in the Python module of the same name, is used. The output produced by HyPy consists of files in the same format as used in the ouput of Watie. Calculations are carried out with the script `hypy`:

```
hypy <input file name>
```

A.3.1. Iodobenzene

In this example, the energy levels and matrix elements of the polarizability tensor and $P_2^0(\cos\theta)$ are computed for the molecule iodobenzene. It requires the results from subsection A.1.1.

Input

```
# set input file names for rigid rotor energy
enr_fname = 'IB_energies_j0_j25.rchm'

# set input file template for electric field gradient
# matrix elements
tensor_ftempl_efg = 'IB_matelem_efg*'

# set input file template for polarizability matrix elements
tensor_ftempl_alpha = 'IB_matelem_alpha*'

# set input file template for cos^2theta matrix elements
tensor_ftempl_p20 = 'IB_matelem_p20*'

# set output filename for hyperfine energies
enr_outfile = 'IB_energies_f0.5_f20.5.rchm'

# set output file template for polarizability matrix elements
tensor_out_ftempl_alpha = 'IB_matelem_alpha_f#_f#.rchm'
```

```
# set output file template for polarizability matrix elements
tensor_out_ftempl_p20 = 'IB_matelem_p20_f#_f#.rchm'

# list of spins of relevant nuclei
Ilist = [2.5]

# quadrupole moment list; here set to 1.0 since
# the quadrupole coupling tensor matrix elements are used
# instead of electric field gradient
eQ_list = [1.0]

# initialize polarizability tensor
alpha = init_polariz(fmin=0.5, fmax=15.5, ilist=Ilist ,
    tensor_ftempl=tensor_ftempl_alpha)

# initialize alignment observable
p20 = init_LegP20(fmin=0.5, fmax=20.5, ilist=Ilist ,
    tensor_ftempl=tensor_ftempl_p20)

tensor_list=[{"tens":alpha ,"ftempl":tensor_out_ftempl_alpha},
    {"tens":p20,"ftempl":tensor_out_ftempl_p20}]

# calculate energies and matrix elements
solve(fmin=0.5, fmax=20.5, ilist=Ilist , eQ_list=eQ_list ,
    enr_fname=enr_fname , ftempl_efg=tensor_ftempl_efg ,
    enr_outfile=enr_outfile , tensor_list=tensor_list)
```

A.4. RichMol

RichMol is used to solve the TDSE for molecules in user-defined external electric field. It is writting in Fortran with a Python interface. The Fortran routines are used to numerically solve the TDSE. The Python modules include functions and classes that are utilized to set the parameters for a calculation. For instance, the basis set for the expansion of the wave function is defined using the class `States` and external electric fields are defined using the class `Fields`. The functions `tdse_run` and `tdse_analyse` are used start solving the TDSE and calculate of expectation values of tensor operators, respectively. The output produced by `tdse_run` consists of an HDF5 file, where the time-dependent coefficients of the wave function are stored. The script `richmol0` is used to start a calculation:

```
richmol0 <input file name>
```

A.4.1. Adiabatic alignment of OCS

In this example, the alignment of OCS is computed for a nonresonant linearly polarized laser pulse with a Gaussian envelop $I(t) = I_0 \exp\left(-4\ln 2t^2/\tau_{\mathrm{FWHM}}^2\right)$ where $\tau_{\mathrm{FWHM}} = 10$ ns and $I_0 = 2 \times 10^{11}$ W/cm^2. The time-dependent intensity is converted to the electric field strength according to

$$E(t) = \frac{1}{\sqrt{2}}\sqrt{\frac{2I(t)}{c\varepsilon_0}}. \tag{A.1}$$

Here, the factor $1/\sqrt{2}$ originates from the averaging over the oscillations of the laser field; see section 2.5. The input electric field thus has a Gaussian shape with a duration of $\sqrt{2}\tau_{\mathrm{FWHM}}$ and maximum field strength $E_0 = \sqrt{I_0/c\varepsilon_0}$. The rotational ground state is used as the initial state. The expectation value of the operator $P_2^0(\cos\theta)$ is computed after solving the TDSE. This example requires the results for the energy levels and matrix elements from the example in subsection A.1.2.

Input

```
# initialise calculation
tdse_init(t_start=-25000.0, t_end=0.0, dt=0.08, units="ps",
    solver="split_zhexpv", accur=1.0e-10, no_krylov=10)

fortran_tdse(flog="fortran.log")

# set field-free basis
ham0 = States("OCS_energies_j0_j25.rchm",
    {'emax':60000,'fmax':25,'fmin':0,'mmin':0,'mmax':0})

# add tensors
alpha = Tensor("OCS_matelem_alpha_j<j1>_j<j2>.rchm",
    rank=2, ind_sym="full", units="au", me_thresh=1.0e-12)

cos2 = Tensor("OCS_matelem_p20_j<j1>_j<j2>.rchm",
    rank=0, ind_sym="full", units="au", me_thresh=1.0e-12)

# set laser field
e_las = Field(form=["0","0","e0*np.exp(-4.0*np.log(2.0)*(t-t0)\
   **2/fwhm**2)*np.cos(omega*t)"],
    params={"e0":8.6802110E+06,"omega":1.0e-40,"fwhm":14142.1,"\
       t0":0.0},
    units="V/cm")

# set interaction Hamiltonian
ham = -0.5 * alpha * e_las
```

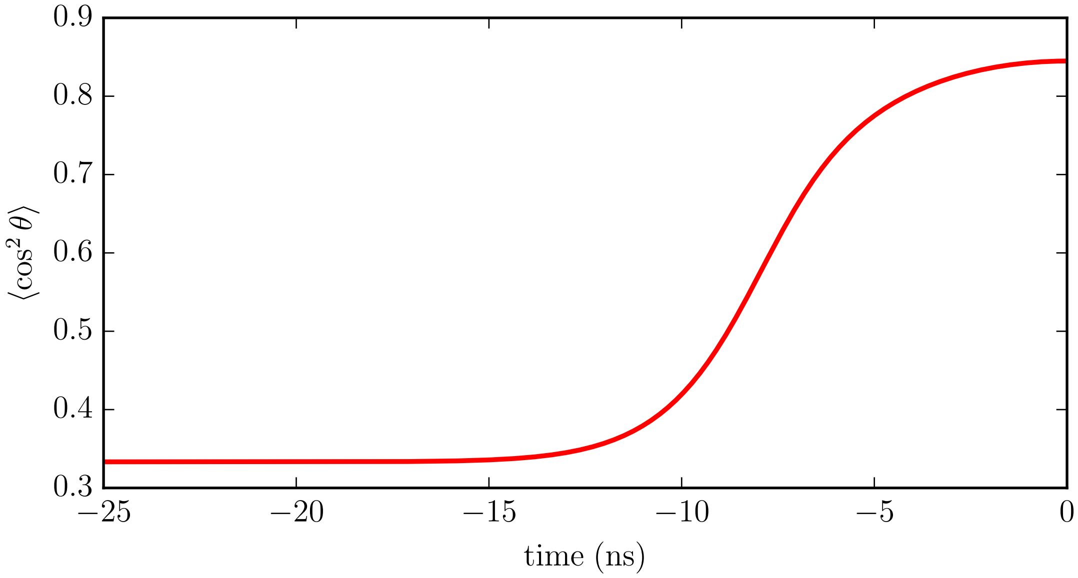

Figure A.1.: Adiabatic alignment for OCS, induced by a Gaussian laser pulse with $\tau_{\mathrm{FWHM}} = 10$ ns and $I_0 = 2\times10^{11}$ W/cm^2.

```
# set initial state
psi = Psi(ham0, ini_coefs=[[0,0,1,1,1.0+0.0j]])

# solve TDSE
tdse_run(ham0, ham, psi, print_coef="coef",
    print_coef_thr=1.0e-10, print_rate=200)

#calculate expectation value
expval1=[cos2,1,{"print_thr":0.0,"print_rate":200,"file":"\
   expval_"}]

tdse_analyse(ham0, psi, print_coef="coef",
    print_expval=[ expval1 ], print_rate=200)
```

Results

The results for $\langle\cos^2\theta\rangle$ are shown in Figure A.1. This expectation value was obtained from the result for $\langle P_2^0(\cos\theta)\rangle$ according to

$$\langle\cos^2\theta\rangle = \frac{2}{3}\langle P_2^0(\cos\theta)\rangle + \frac{1}{3}. \tag{A.2}$$

A.4.2. Impulsive alignment of iodobenzene

Here, the impulsive alignment of iodobenzene is computed for a Gaussian laser pulse with $\tau_{\mathrm{FWHM}} = 1$ ps and $I_0 = 10^{11}$ W/cm^2. The calculation consists of two steps. First, the TDSE is solved for time interval during which the field is present. Then, a field-free propagation of the resulting wave packet is carried out and the expectation value $\left\langle P_2^0(\cos\theta)\right\rangle$ is computed. The initial state of the first calculation is the rotational ground state. In the second step, the final wave function of the first step, obtained after switching off the laser field, is read and used as the initial state of the post-pulse propagation. This example requires the results from subsection A.1.1.

Input for laser field

```
# initialise calculation
tdse_init(t_start=-3.0, t_end=3.0, dt=0.002, units="ps",
    solver="split_zhexpv", accur=1.0e-10, no_krylov=10)

fortran_tdse(flog="fortran.log")

# set field-free basis
ham0 = States("IB_energies_j0_j25.rchm",
    {'emax':60000,'fmax':20,'fmin':0,'mmin':0,'mmax':0})

# add tensors
alpha = Tensor("IB_matelem_alpha_j<j1>_j<j2>.rchm"
     rank=2, ind_sym="full", units="au", me_thresh=1.0e-12)

cos2 = Tensor("IB_matelem_p20_j<j1>_j<j2>.rchm",
    rank=0, ind_sym="full", units="au", me_thresh=1.0e-10)

# Gaussian pulse, linearly polarized along Z-axis
# with maximum intensity 1e11 W/cm^2
# and FWHM=1ps (in intensity profile)
e_las = Field(form=["0","0","e0*np.exp(-4.0*np.log(2.0)*(t-t0)\
   **2/fwhm**2)*np.cos(omega*t)"],
    params={"e0":6.1378360E+06,"omega":1.0e-40,
    "fwhm":1.4142,"t0":0.0}, units="V/cm")

# set interaction Hamiltonian
ham = -0.5 * alpha * e_las

# set initial state
psi = Psi(ham0, ini_coefs=[[0,0,1,1,1.0+0.0j]])

# solve TDSE
tdse_run(ham0, ham, psi, print_coef="coef",
    print_coef_thr=1.0e-10, print_rate=20)

# Calculate expectation value
```

```
expval1=[cos2,1,{"print_thr":0.0,"print_rate":20,"file":"\
   expval_"}]

tdse_analyse(ham0, psi, print_coef="coef",
     print_expval=[ expval1 ], print_rate=20)
```

Input for post-pulse propagation

```
# initialise calculation
tdse_init(t_start=-3.0, t_end=3.0, dt=0.002, units="ps",
     solver="split_zhexpv", accur=1.0e-10, no_krylov=10)

fortran_tdse(flog="fortran.log")

# set field-free basis
ham0 = States("IB_energies_j0_j20.rchm",
     {'emax':60000,'fmax':20,'fmin':0,'mmin':0,'mmax':0})

# add tensor
cos2 = Tensor("IB_matelem_p20_j<j1>_j<j2>.rchm",
     rank=0, ind_sym="full", units="au", me_thresh=1.0e-10)

# initialise wave function
psi = Psi(ham0, ini_coefs=[[0,0,1,1,1.0+0.0j]])

# read wave function from last step of pulse propagation
fname_result="coef"

read_coefficients(3.0, ham0, psi, fout=fname_result)

# solve TDSE for field-free case
tdse_run_field_free(ham0, psi, print_coef="coef_ff",
     print_coef_thr=1.0e-10, print_rate=100)

# Calculate expectation value
expval1=[cos2,1,{"print_thr":0.0,"print_rate":100,"file":"\
   expval_"}]

tdse_analyse(ham0, psi, print_coef="coef_ff",
     print_expval=[ expval1 ], print_rate=100)
```

Results

The result for the expectation value $\langle \cos^2\theta \rangle$ is shown in Figure 7.2 (a).

A.4.3. Impulsive alignment of iodobenzene with nuclear-quadrupole interactions

This example is analogous to subsection A.4.2 but takes into account the nuclear quadrupole coupling. It thus requires the results of subsection A.3.1. The lowest-lying spin-rotational state with $F = 5/2$ and $M = 1/2$ is used as the initial state.

Input for laser field

```
# initialise calculation
tdse_init(t_start=-3.0, t_end=3.0, dt=0.002, units="ps",
    solver="split_zhexpv", accur=1.0e-10, no_krylov=10)

fortran_tdse(flog="fortran.log")

# set field-free basis
ham0 = States("IB_energies_f0.5_f20.5.rchm",
    {'emax':60000,'fmax':20.5,'fmin':0.0,'mmin':0.5,'mmax'\
       :0.5})

# add tensors
alpha = Tensor("IB_matelem_alpha_f<f1>_f<f2>.rchm",
    rank=2, ind_sym="full", units="au", me_thresh=1.0e-12)

cos2 = Tensor("IB_matelem_p20_f<f1>_f<f2>.rchm",
    rank=0, ind_sym="full", units="au", me_thresh=1.0e-10)

# Gaussian pulse, linearly polarized along Z-axis
# with maximum intensity 1e11 W/cm^2 and FWHM=1ps (in intensity\
    profile)
e_las = Field(form=["0","0","e0*np.exp(-4.0*np.log(2.0)*(t-t0)\
   **2/fwhm**2)*np.cos(omega*t)"],
    params={"e0":6.1378360E+06,"omega":1.0e-40,
    "fwhm":1.4142,"t0":0.0}, units="V/cm")

# set interaction Hamiltonian
ham = -0.5 * alpha * e_las

# set initial state
psi = Psi(ham0, ini_coefs=[[0.5,2.5,1,1,1.0+0.0j]])

# solve TDSE
tdse_run(ham0, ham, psi, print_coef="coef_qc",
    print_coef_thr=1.0e-10, print_rate=20)
```

```
# Calculate expectation value
expval1=[cos2,1,{"print_thr":0.0,"print_rate":20,"file":"\
   expval_qc_"}]

tdse_analyse(ham0, psi, print_coef="coef_qc",
     print_expval=[ expval1 ], print_rate=20)
```

Input for post-pulse propagation

```
# initialise calculation
tdse_init(t_start=-3.0, t_end=3.0, dt=0.002, units="ps",
     solver="split_zhexpv", accur=1.0e-10, no_krylov=10)

fortran_tdse(flog="fortran.log")

# set field-free basis
ham0 = States("IB_energies_f0.5_f20.5.rchm",
     {'emax':60000,'fmax':20.5,'fmin':0.0,'mmin':0.5,'mmax'\
         :0.5})

# add tensor
cos2 = Tensor("IB_matelem_p20_f<f1>_f<f2>.rchm",
     rank=0, ind_sym="full", units="au", me_thresh=1.0e-10)

# initialise wave function
psi = Psi(ham0, ini_coefs=[[0.5,2.5,1,1,1.0+0.0j]])

# read wave function from last step of pulse propagation
fname_result="coef_qc"

read_coefficients(3.0, ham0, psi, fout=fname_result)

# solve TDSE for field-free case
tdse_run_field_free(ham0, psi, print_coef="coef_qc_ff",
     print_coef_thr=1.0e-10, print_rate=100)

# Calculate expectation value
expval1=[cos2,1,{"print_thr":0.0,"print_rate":100,"file":"\
   expval_qc_"}]

tdse_analyse(ham0, psi, print_coef="coef_qc_ff",
     print_expval=[ expval1 ], print_rate=100)
```

Results

The result for $\langle \cos^2\theta \rangle$ from this calculation is shown in Figure 7.3 (a).

A.4.4. Mixed-field orientation of Indole(H_2O)

In this example, the mixed-field orientation of indole(H_2O) is computed. In the first step, the dc field is adiabatically switched on and in the second step, the laser field is applied together with the constant dc field. Here, the files produced by in the example in subsection A.2.1 are used. The same RichMol input can be used to compute the mixed-field orientation of indole(H_2O) with the modified polarizability if the maximum value of J is increased to 40 in the second step and the energy levels and matrix elements from subsection A.2.2 are used.

Input for adiabatic turn on of the dc field

```
# initialise calculation
tdse_init(t_start=0.0, t_end=20000.0, dt=0.02, units="ps",
    solver="split_zhexpv", accur=1.0e-10, no_krylov=10)

fortran_tdse(flog="fortran.log")

# set field-free basis
ham0 = States("energies_j0_j25.rchm",
    {'emax':60000,'fmax':15,'fmin':0,'mmin':0,'mmax':0})

# add tensors
alpha = Tensor("matelem_alpha_j<j1>_j<j2>.rchm",
    rank=2, ind_sym="full", units="au", me_thresh=1.0e-12)

mu = Tensor("matelem_mu_j<j1>_j<j2>.rchm",
    rank=1, ind_sym="full", units="au", me_thresh=1.0e-12)

cos2 = Tensor("matelem_3cos2_1_j<j1>_j<j2>.rchm",
    rank=0, ind_sym="full", units="au", me_thresh=1.0e-12)

cos = Tensor("matelem_cos_j<j1>_j<j2>.rchm",
    rank=0, ind_sym="full", units="au", me_thresh=1.0e-12)

cos2tau = Tensor("matelem_cos2tau_j<j1>_j<j2>.rchm",
    rank=0, ind_sym="full", units="au", me_thresh=1.0e-12)

# set static field
e_stat = Field(form=["0","0","e0*np.sin(omega*t)"],
```

```
    params={"e0":600.0,"omega":0.0000785398163397448},
    units="V/cm")

# set interaction Hamiltonian
ham = - 1.0 * mu * e_stat

# set initial state
psi = Psi(ham0, ini_coefs=[[0,0,1,1,1.0+0.0j]])

# solve TDSE
tdse_run(ham0, ham, psi, print_coef="coef_dc",
    print_coef_thr=1.0e-10, print_rate=200)

#calculate expectation values
expval1=[cos2,1,{"print_thr":0.0,"print_rate":200,
    "file":"expval_"}]

expval2=[cos,1,{"print_thr":0.0,"print_rate":200,
    "file":"expval_"}]

expval3=[cos2tau,1,{"print_thr":0.0,"print_rate":200,
    "file":"expval_"}]

tdse_analyse(ham0, psi, print_coef="coef_dc",
    print_expval=[ expval1, expval2, expval3 ], print_rate=200)
```

Input for ac and dc field

```
# initialise calculation
tdse_init(t_start=20000.0, t_end=21750.0, dt=0.02, units="ps",
    solver="split_zhexpv", accur=1.0e-10, no_krylov=10)

fortran_tdse(flog="fortran.log")

# set field-free basis
ham0 = States("energies_j0_j25.rchm",{'emax':60000,
    'fmax':25,'fmin':0,'mmin':0,'mmax':0})

# add tensors
alpha = Tensor("matelem_alpha_j<j1>_j<j2>.rchm",
    rank=2, ind_sym="full", units="au", me_thresh=1.0e-12)

mu = Tensor("matelem_mu_j<j1>_j<j2>.rchm",
    rank=1, ind_sym="full", units="au", me_thresh=1.0e-12)
```

```
cos2 = Tensor("matelem_3cos2_1_j<j1>_j<j2>.rchm",
    rank=0, ind_sym="full", units="au", me_thresh=1.0e-12)

cos = Tensor("matelem_cos_j<j1>_j<j2>.rchm",
    rank=0, ind_sym="full", units="au", me_thresh=1.0e-12)

cos2tau = Tensor("matelem_cos2tau_j<j1>_j<j2>.rchm",
    rank=0, ind_sym="full", units="au", me_thresh=1.0e-12)

# set laser field
e_las = Field(form=["0","0","e0*np.exp(-4.0*np.log(2.0)*(t-t0)\
   **2/fwhm**2)*np.cos(omega*t)"],
    params={"e0":1.9410E+07,"omega":1.0e-40,
    "fwhm":1000.0,"t0":21750.0}, units="V/cm")

#set static field
e_stat = Field(form=["0","0","e0"],params={"e0":600},
    units="V/cm")

# set interaction Hamiltonian
ham = -0.5 * alpha * e_las - 1.0 * mu * e_stat

# set initial state (read result from
# adiabatic turn on of dc field)
psi = Psi(ham0, ini_coefs=[[0,0,1,1,1.0+0.0j]])

read_coefficients(1.9996e+04, ham0, psi, fout="coef_dc")

# solve TDSE
tdse_run(ham0, ham, psi, print_coef="coef",
    print_coef_thr=1.0e-10, print_rate=100)

#calculate expectation values
expval1=[cos2,1,{"print_thr":0.0,"print_rate":100,
    "file":"expval_"}]

expval2=[cos,1,{"print_thr":0.0, "print_rate":100,
    "file":"expval_"}]

expval3=[cos2tau,1,{"print_thr":0.0, "print_rate":100,
    "file":"expval_"}]

tdse_analyse(ham0, psi, print_coef="coef",
    print_expval=[ expval1, expval2, expval3 ], print_rate=100)
```

Results

The results for $\langle \cos\theta \rangle$, $\left\langle \cos^2\theta \right\rangle$ and $\left\langle \cos^2\tau \right\rangle$ are depicted in Figure 4.3.

Bibliography

[1] O. Geßner, A. M. D. Lee, J. P. Shaffer, H. Reisler, S. V. Levchenko, A. I. Krylov, J. G. Underwood, H. Shi, A. L. L. East, D. M. Wardlaw, E. t. H. Chrysostom, C. C. Hayden, and A. Stolow, "Femtosecond multidimensional imaging of a molecular dissociation," Science **311**, 219–222 (2006).

[2] M. Meckel, D. Comtois, D. Zeidler, A. Staudte, D. Pavičić, H. C. Bandulet, H. Pépin, J. C. Kieffer, R. Dörner, D. M. Villeneuve, and P. B. Corkum, "Laser-induced electron tunneling and diffraction," Science **320**, 1478–1482 (2008).

[3] C. Z. Bisgaard, O. J. Clarkin, G. Wu, A. M. D. Lee, O. Geßner, C. C. Hayden, and A. Stolow, "Time-resolved molecular frame dynamics of fixed-in-space CS_2 molecules," Science **323**, 1464–1468 (2009).

[4] L. Holmegaard, J. L. Hansen, L. Kalhøj, S. L. Kragh, H. Stapelfeldt, F. Filsinger, J. Küpper, G. Meijer, D. Dimitrovski, M. Abu-samha, C. P. J. Martiny, and L. B. Madsen, "Photoelectron angular distributions from strong-field ionization of oriented molecules," Nat. Phys. **6**, 428 (2010), arXiv:1003.4634 [physics] .

[5] J. Hansen, H. Stapelfeldt, D. Dimitrovski, M. Abu-Samha, C. Martiny, and L. Madsen, "Time-resolved photoelectron angular distributions from strong-field ionization of rotating naphthalene molecules," Phys. Rev. Lett. **106**, 073001 (2011).

[6] F. Kelkensberg, A. Rouzée, W. Siu, G. Gademann, P. Johnsson, M. Lucchini, R. R. Lucchese, and M. J. J. Vrakking, "Xuv ionization of aligned molecules," Phys. Rev. A **84**, 051404 (2011).

[7] R. Boll, D. Anielski, C. Bostedt, J. D. Bozek, L. Christensen, R. Coffee, S. De, P. Decleva, S. W. Epp, B. Erk, L. Foucar, F. Krasniqi, J. Küpper, A. Rouzée, B. Rudek, A. Rudenko, S. Schorb, H. Stapelfeldt, M. Stener, S. Stern, S. Techert, S. Trippel, M. J. J. Vrakking, J. Ullrich, and D. Rolles, "Femtosecond photoelectron diffraction on laser-aligned molecules: Towards time-resolved imaging of molecular structure," Phys. Rev. A **88**, 061402(R) (2013).

[8] J. Itatani, J. Levesque, D. Zeidler, H. Niikura, H. Pépin, J. C. Kieffer, P. B. Corkum, and D. M. Villeneuve, "Tomographic imaging of molecular orbitals," Nature **432**, 867–871 (2004).

[9] C. Vozzi, M. Negro, F. Calegari, G. Sansone, M. Nisoli, S. De Silvestri, and S. Stagira, "Generalized molecular orbital tomography," Nat. Phys. **7**, 822–826 (2011).

[10] P. M. Kraus, D. Baykusheva, and H. J. Wörner, "Two-pulse field-free orientation reveals anisotropy of molecular shape resonance," Phys. Rev. Lett. **113**, 023001 (2014), arXiv:1311.3923 [physics] .

[11] C. J. Hensley, J. Yang, and M. Centurion, "Imaging of isolated molecules with ultrafast electron pulses," Phys. Rev. Lett. **109**, 133202 (2012).

[12] C. I. Blaga, J. Xu, A. D. DiChiara, E. Sistrunk, K. Zhang, P. Agostini, T. A.

Miller, L. F. DiMauro, and C. D. Lin, "Imaging ultrafast molecular dynamics with laser-induced electron diffraction," Nature **483**, 194–197 (2012).

[13] J. Yang, M. Guehr, T. Vecchione, M. S. Robinson, R. Li, N. Hartmann, X. Shen, R. Coffee, J. Corbett, A. Fry, K. Gaffney, T. Gorkhover, C. Hast, K. Jobe, I. Makasyuk, A. Reid, J. Robinson, S. Vetter, F. Wang, S. Weathersby, C. Yoneda, M. Centurion, and X. Wang, "Diffractive imaging of a rotational wavepacket in nitrogen molecules with femtosecond megaelectronvolt electron pulses," Nat. Commun. **7**, 11232 (2016).

[14] A. Barty, J. Küpper, and H. N. Chapman, "Molecular imaging using x-ray free-electron lasers," Annu. Rev. Phys. Chem. **64**, 415–435 (2013).

[15] S. Pabst, P. J. Ho, and R. Santra, "Computational studies of x-ray scattering from three-dimensionally-aligned asymmetric-top molecules," Phys. Rev. A **81**, 043425 (2010).

[16] M. M. Seibert, T. Ekeberg, F. R. N. C. Maia, M. Svenda, J. Andreasson, O. Jönsson, D. Odić, B. Iwan, A. Rocker, D. Westphal, M. Hantke, D. P. Deponte, A. Barty, J. Schulz, L. Gumprecht, N. Coppola, A. Aquila, M. Liang, T. A. White, A. Martin, C. Caleman, S. Stern, C. Abergel, V. Seltzer, J.-M. Claverie, C. Bostedt, J. D. Bozek, S. Boutet, A. A. Miahnahri, M. Messerschmidt, J. Krzywinski, G. Williams, K. O. Hodgson, M. J. Bogan, C. Y. Hampton, R. G. Sierra, D. Starodub, I. Andersson, S. Bajt, M. Barthelmess, J. C. H. Spence, P. Fromme, U. Weierstall, R. Kirian, M. Hunter, R. B. Doak, S. Marchesini, S. P. Hau-Riege, M. Frank, R. L. Shoeman, L. Lomb, S. W. Epp, R. Hartmann, D. Rolles, A. Rudenko, C. Schmidt, L. Foucar, N. Kimmel, P. Holl, B. Rudek, B. Erk, A. Hömke, C. Reich, D. Pietschner, G. Weidenspointner, L. Strüder, G. Hauser, H. Gorke, J. Ullrich, I. Schlichting, S. Herrmann, G. Schaller, F. Schopper, H. Soltau, K.-U. Kühnel, R. Andritschke, C.-D. Schröter, F. Krasniqi, M. Bott, S. Schorb, D. Rupp, M. Adolph, T. Gorkhover, H. Hirsemann, G. Potdevin, H. Graafsma, B. Nilsson, H. N. Chapman, and J. Hajdu, "Single mimivirus particles intercepted and imaged with an X-ray laser," Nature **470**, 78 (2011).

[17] J. Küpper, S. Stern, L. Holmegaard, F. Filsinger, A. Rouzée, A. Rudenko, P. Johnsson, A. V. Martin, M. Adolph, A. Aquila, S. Bajt, A. Barty, C. Bostedt, J. Bozek, C. Caleman, R. Coffee, N. Coppola, T. Delmas, S. Epp, B. Erk, L. Foucar, T. Gorkhover, L. Gumprecht, A. Hartmann, R. Hartmann, G. Hauser, P. Holl, A. Hömke, N. Kimmel, F. Krasniqi, K.-U. Kühnel, J. Maurer, M. Messerschmidt, R. Moshammer, C. Reich, B. Rudek, R. Santra, I. Schlichting, C. Schmidt, S. Schorb, J. Schulz, H. Soltau, J. C. H. Spence, D. Starodub, L. Strüder, J. Thøgersen, M. J. J. Vrakking, G. Weidenspointner, T. A. White, C. Wunderer, G. Meijer, J. Ullrich, H. Stapelfeldt, D. Rolles, and H. N. Chapman, "X-ray diffraction from isolated and strongly aligned gas-phase molecules with a free-electron laser," Phys. Rev. Lett. **112**, 083002 (2014), arXiv:1307.4577 [physics] .

[18] R. Neutze, R. Wouts, D. van der Spoel, E. Weckert, and J. Hajdu, "Potential for biomolecular imaging with femtosecond x-ray pulses," Nature **406**, 752–757 (2000).

[19] R. J. D. Miller, "Mapping atomic motions with ultrabright electrons: The chemists'

gedanken experiment enters the lab frame," Annu. Rev. Phys. Chem. **65**, 583–604 (2014).

[20] J. C. H. Spence and R. B. Doak, "Single molecule diffraction," Phys. Rev. Lett. **92**, 198102 (2004).

[21] P. R. Brooks and E. M. Jones, "Reactive scattering of K atoms from oriented CH_3I molecules," J. Chem. Phys. **45**, 3449 (1966).

[22] R. J. Beuhler, R. B. Bernstein, and K. H. Kramer, "Observation of reactive asymmetry of methyl iodide. Crossed beam study of reaction of rubidium with oriented methyl iodide molecules," J. Am. Chem. Soc. **88**, 5331 (1966).

[23] D. Parker, K. Chakravorty, and R. Bernstein, "Crossed beam reaction of oriented methyl iodide with rubidium: Steric factor and reactive asymmetry versus scattering angle," Chem. Phys. Lett. **86**, 113–117 (1982).

[24] S. Stolte, K. Chakravorty, R. Bernstein, and D. Parker, "Analysis of the steric dependence of the $CH_3I + Rb$ reaction using a legendre expansion technique," Chem. Phys. **71**, 353–361 (1982).

[25] F. Aoiz, B. Friedrich, V. Herrero, V. S. Rábanos, and J. Verdasco, "Effect of pendular orientation on the reactivity of h + dcl: a quasiclassical trajectory study," Chem. Phys. Lett. **289**, 132–140 (1998).

[26] R. N. Zare, "Laser Control of Chemical Reactions," Science **279**, 1875–1879 (1998).

[27] T. P. Rakitzis, A. J. van den Brom, and M. H. M. Janssen, "Directional dynamics in the photodissociation of oriented molecules," Science **303**, 1852–1854 (2004).

[28] P. R. Brooks, "Reactions of oriented molecules," Science **193**, 11 (1976).

[29] D. A. Baugh, D. Y. Kim, V. A. Cho, L. Pipes, J. Petteway, and C. D. Fuglesang, "Production of a pure, single ro-vibrational quantum-state molecular beam," Chem. Phys. Lett. **219**, 207–213 (1994).

[30] D. H. Parker and R. B. Bernstein, "Oriented molecule beams via the electrostatic hexapole - preparation, characterization, and reactive scattering," Annu. Rev. Phys. Chem. **40**, 561–595 (1989).

[31] H. J. Loesch and A. Remscheid, "Brute force in molecular reaction dynamics: A novel technique for measuring steric effects," J. Chem. Phys. **93**, 4779 (1990).

[32] B. Friedrich and D. R. Herschbach, "Spatial orientation of molecules in strong electric fields and evidence for pendular states," Nature **353**, 412–414 (1991).

[33] B. Friedrich and D. R. Herschbach, "On the possibility of orienting rotationally cooled polar molecules in an electric field," Z. Phys. D **18**, 153–161 (1991).

[34] B. Friedrich and D. Herschbach, "Polarization of molecules induced by intense nonresonant laser fields," J. Phys. Chem. **99**, 15686 (1995).

[35] B. Friedrich and D. Herschbach, "Alignment and trapping of molecules in intense laser fields," Phys. Rev. Lett. **74**, 4623–4626 (1995).

[36] B. Friedrich and D. Herschbach, "Polarizability interaction in molecules and double-well tunneling," Z. Phys. D **36**, 221–228 (1996).

[37] T. Seideman, "Rotational excitation and molecular alignment in intense laser fields," J. Chem. Phys. **103**, 7887 (1995).

[38] W. Kim and P. M. Felker, "Spectroscopy of pendular states in optical-field-aligned species," J. Chem. Phys. **104**, 1147–1150 (1996).

[39] H. Sakai, C. P. Safvan, J. J. Larsen, K. M. Hilligsøe, K. Hald, and H. Stapelfeldt, "Controlling the alignment of neutral molecules by a strong laser field," J. Chem. Phys. **110**, 10235–10238 (1999).

[40] J. J. Larsen, H. Sakai, C. P. Safvan, I. Wendt-Larsen, and H. Stapelfeldt, "Aligning molecules with intense nonresonant laser fields," J. Chem. Phys. **111**, 7774 (1999).

[41] J. J. Larsen, K. Hald, N. Bjerre, H. Stapelfeldt, and T. Seideman, "Three dimensional alignment of molecules using elliptically polarized laser fields," Phys. Rev. Lett. **85**, 2470–2473 (2000).

[42] J. Underwood, B. Sussman, and A. Stolow, "Field-free three dimensional molecular axis alignment," Phys. Rev. Lett. **94**, 143002 (2005).

[43] K. F. Lee, D. M. Villeneuve, P. B. Corkum, A. Stolow, and J. G. Underwood, "Field-free three-dimensional alignment of polyatomic molecules," Phys. Rev. Lett. **97**, 173001 (2006).

[44] S. S. Viftrup, V. Kumarappan, S. Trippel, H. Stapelfeldt, E. Hamilton, and T. Seideman, "Holding and spinning molecules in space," Phys. Rev. Lett. **99**, 143602 (2007).

[45] A. Rouzee, S. Guerin, O. Faucher, and B. Lavorel, "Field-free molecular alignment of asymmetric top molecules using elliptically polarized laser pulses," Phys. Rev. A **77**, 043412 (2008).

[46] S. S. Viftrup, V. Kumarappan, L. Holmegaard, C. Z. Bisgaard, H. Stapelfeldt, M. Artamonov, E. Hamilton, and T. Seideman, "Controlling the rotation of asymmetric top molecules by the combination of a long and a short laser pulse," Phys. Rev. A **79**, 023404 (2009).

[47] J. Ortigoso, M. Rodriguez, M. Gupta, and B. Friedrich, "Time evolution of pendular states created by the interaction of molecular polarizability with a pulsed nonresonant laser field," J. Chem. Phys. **110**, 3870–3875 (1999).

[48] H. Stapelfeldt and T. Seideman, "Colloquium: Aligning molecules with strong laser pulses," Rev. Mod. Phys. **75**, 543–557 (2003).

[49] B. Friedrich and D. Herschbach, "Enhanced orientation of polar molecules by combined electrostatic and nonresonant induced dipole forces," J. Chem. Phys. **111**, 6157 (1999).

[50] B. Friedrich and D. Herschbach, "Manipulating molecules via combined static and laser fields," J. Phys. Chem. A **103**, 10280–10288 (1999).

[51] M. Härtelt and B. Friedrich, "Directional states of symmetric-top molecules produced by combined static and radiative electric fields," J. Chem. Phys. **128**, 224313 (2008).

[52] H. Sakai, S. Minemoto, H. Nanjo, H. Tanji, and T. Suzuki, "Controlling the orientation of polar molecules with combined electrostatic and pulsed, nonresonant laser fields," Phys. Rev. Lett. **90**, 083001 (2003).

[53] H. Tanji, S. Minemoto, and H. Sakai, "Three-dimensional molecular orientation with combined electrostatic and elliptically polarized laser fields," Phys. Rev. A **72**, 063401 (2005).

[54] J. L. Hansen, J. J. Omiste, J. H. Nielsen, D. Pentlehner, J. Küpper, R. González-

Férez, and H. Stapelfeldt, “Mixed-field orientation of molecules without rotational symmetry,” J. Chem. Phys. **139**, 234313 (2013), arXiv:1308.1216 [physics] .

[55] S. Trippel, T. Mullins, N. L. M. Müller, J. S. Kienitz, R. González-Férez, and J. Küpper, “Two-state wave packet for strong field-free molecular orientation,” Phys. Rev. Lett. **114**, 103003 (2015), arXiv:1409.2836 [physics] .

[56] J. J. Omiste, M. Gaerttner, P. Schmelcher, R. González-Férez, L. Holmegaard, J. H. Nielsen, H. Stapelfeldt, and J. Küpper, “Theoretical description of adiabatic laser alignment and mixed-field orientation: the need for a non-adiabatic model,” Phys. Chem. Chem. Phys. **13**, 18815–18824 (2011), arXiv:1105.0534 [physics] .

[57] J. H. Nielsen, H. Stapelfeldt, J. Küpper, B. Friedrich, J. J. Omiste, and R. González-Férez, “Making the best of mixed-field orientation of polar molecules: A recipe for achieving adiabatic dynamics in an electrostatic field combined with laser pulses,” Phys. Rev. Lett. **108**, 193001 (2012), arXiv:1204.2685 [physics] .

[58] T. Seideman, “Revival structure of aligned rotational wave packets,” Phys. Rev. Lett. **83**, 4971–4974 (1999).

[59] F. Rosca-Pruna and M. J. J. Vrakking, “Experimental observation of revival structures in picosecond laser-induced alignment of I_2,” Phys. Rev. Lett. **87**, 153902 (2001).

[60] E. Hamilton, T. Seideman, T. Ejdrup, M. D. Poulsen, C. Z. Bisgaard, S. S. Viftrup, and H. Stapelfeldt, “Alignment of symmetric top molecules by short laser pulses,” Phys. Rev. A **72**, 043402 (2005).

[61] O. Ghafur, A. Rouzée, A. Gijsbertsen, W. K. Siu, S. Stolte, and M. J. J. Vrakking, “Impulsive orientation and alignment of quantum-state-selected NO molecules,” Nat. Phys. **5**, 289–293 (2009).

[62] E. T. Karamatskos, S. Raabe, T. Mullins, A. Trabattoni, P. Stammer, G. Goldsztejn, R. R. Johansen, K. Długołęcki, H. Stapelfeldt, M. J. J. Vrakking, S. Trippel, A. Rouzée, and J. Küpper, “Molecular movie of ultrafast coherent rotational dynamics of OCS,” Nat. Commun. **10**, 3364 (2019), arXiv:1807.01034 [physics] .

[63] E. Peronne, M. Poulsen, C. Bisgaard, H. Stapelfeldt, and T. Seideman, “Nonadiabatic alignment of asymmetric top molecules: Field-free alignment of iodobenzene,” Phys. Rev. Lett. **91**, 04300 (2003).

[64] A. Rouzee, S. Guerin, V. Boudon, B. Lavorel, and O. Faucher, “Field-free one-dimensional alignment of ethylene molecule,” Phys. Rev. A **73**, 033418–9 (2006).

[65] L. Holmegaard, S. S. Viftrup, V. Kumarappan, C. Z. Bisgaard, H. Stapelfeldt, E. Hamilton, and T. Seideman, “Control of rotational wave-packet dynamics in asymmetric top molecules,” Phys. Rev. A **75**, 051403 (2007).

[66] T. Seideman, “On the dynamics of rotationally broad, spatially aligned wave packets,” J. Chem. Phys. **115**, 5965 (2001).

[67] J. Underwood, M. Spanner, M. Ivanov, J. Mottershead, B. Sussman, and A. Stolow, “Switched wave packets: A route to nonperturbative quantum control,” Phys. Rev. Lett. **90**, 223001 (2003).

[68] A. Goban, S. Minemoto, and H. Sakai, “Laser-field-free molecular orientation,” Phys. Rev. Lett. **101**, 013001 (2008).

[69] A. Chatterley, E. T. Karamatskos, C. Schouder, L. Christiansen, A. V. Jörgensen, T. Mullins, J. Küpper, and H. Stapelfeldt, "Switched wave packets with spectrally truncated chirped pulses," J. Chem. Phys. **148**, 221105 (2018), arXiv:1803.03953 [physics] .

[70] F. Filsinger, G. Meijer, H. Stapelfeldt, H. Chapman, and J. Küpper, "State- and conformer-selected beams of aligned and oriented molecules for ultrafast diffraction studies," Phys. Chem. Chem. Phys. **13**, 2076–2087 (2011), arXiv:1009.0871 [physics] .

[71] Y.-P. Chang, D. A. Horke, S. Trippel, and J. Küpper, "Spatially-controlled complex molecules and their applications," Int. Rev. Phys. Chem. **34**, 557–590 (2015), arXiv:1505.05632 [physics] .

[72] L. Holmegaard, J. H. Nielsen, I. Nevo, H. Stapelfeldt, F. Filsinger, J. Küpper, and G. Meijer, "Laser-induced alignment and orientation of quantum-state-selected large molecules," Phys. Rev. Lett. **102**, 023001 (2009), arXiv:0810.2307 [physics] .

[73] D. R. Herschbach, "Calculation of energy levels for internal torsion and over-all rotation. III," J. Chem. Phys. **31**, 91–108 (1959).

[74] G. Berden, W. L. Meerts, M. Schmitt, and K. Kleinermanns, "High resolution UV spectroscopy of phenol and the hydrogen bonded phenol-water cluster," J. Chem. Phys. **104**, 972 (1996).

[75] M. Gerhards, M. Schmitt, and K. Kleinermanns, "The structure of phenol(h_2o) obtained by microwave spectroscopy," J. Chem. Phys. **104**, 967 (1996).

[76] S. Blanco, J. Lopez, J. Alonso, P. Ottaviani, and W. Caminati, "Pure rotational spectrum and model calculations of indole-water," J. Chem. Phys. **119**, 880–886 (2003).

[77] T. M. Korter, D. W. Pratt, and J. Küpper, "Indole-H_2O in the gas phase. Structures, barriers to internal motion, and $S_1 \leftarrow S_0$ transition moment orientation. Solvent reorganization in the electronically excited state," J. Phys. Chem. A **102**, 7211–7216 (1998).

[78] K. M. Yamada, G. Winnewisser, and P. Jensen, "Internal rotation tunnelling in HSOH," J. Mol. Struct. **695–696**, 323–337 (2004).

[79] R. I. Ovsyannikov, V. V. Melnikov, W. Thiel, P. Jensen, O. Baum, T. F. Giesen, and S. N. Yurchenko, "Theoretical rotation-torsion energies of HSOH," J. Chem. Phys. **129**, 154314 (2008).

[80] V. Aquilanti, M. Ragni, A. C. P. Bitencourt, G. S. Maciel, and F. V. Prudente, "Intramolecular dynamics of RS-SR' systems (R, R' = H, F, Cl, CH_3, C_2 H_5): Torsional potentials, energy levels, partition functions," J. Phys. Chem. A **113**, 3804–3813 (2009).

[81] L. H. Coudert, L. F. Pacios, and J. Ortigoso, "Rotation-induced breakdown of torsional quantum control," Phys. Rev. Lett. **107**, 113004 (2011).

[82] C. B. Madsen, L. B. Madsen, S. S. Viftrup, M. P. Johansson, T. B. Poulsen, L. Holmegaard, V. Kumarappan, K. Jørgensen, and H. Stapelfeldt, "Manipulating the torsion of molecules by strong laser pulses," Phys. Rev. Lett. **102**, 073007 (2009), arXiv:0809.2935 [physics] .

[83] S. Ramakrishna and T. Seideman, “Torsional control by intense pulses,” Phys. Rev. Lett. **99**, 103001 (2007).

[84] T. Grohmann, M. Leibscher, and T. Seideman, “Laser-controlled torsions: Four-dimensional theory and the validity of reduced dimensionality models,” Phys. Rev. Lett. **118**, 203201 (2017).

[85] L. Christensen, J. H. Nielsen, C. B. Brandt, C. B. Madsen, L. B. Madsen, C. S. Slater, A. Lauer, M. Brouard, M. P. Johansson, B. Shepperson, and H. Stapelfeldt, “Dynamic stark control of torsional motion by a pair of laser pulses,” Phys. Rev. Lett. **113**, 073005 (2014).

[86] R. Altkorn, R. N. Zare, and C. H. Greene, “Depolarization of optically prepared molecules by two randomly oriented spins,” Mol. Phys. **55**, 1–9 (1985).

[87] C. Yan and A. C. Kummel, “Effect of hyperfine depolarization upon creation and detection of alignment in free-jet expansions via selective photodissociation,” J. Chem. Phys. **98**, 6869–6882 (1993).

[88] T. A. Cool and N. Hemmi, “Hyperfine polarization quantum beats in cyanogen,” J. Chem. Phys. **103**, 3357–3366 (1995).

[89] J. Zhang, C. W. Riehn, M. Dulligan, and C. Wittig, “An experimental study of HF photodissociation: Spin-orbit branching ratio and infrared alignment,” J. Chem. Phys. **104**, 7027–7035 (1996).

[90] E. R. Wouters, L. D. Siebbeles, K. L. Reid, B. Buijsse, and W. J. van der Zande, “Observation of fine structure and hyperfine structure depolarization in the photofragment anisotropy in triplet H_2,” Chem. Phys. **218**, 309–323 (1997).

[91] D. Sofikitis, L. Rubio-Lago, M. R. Martin, D. J. Ankeny Brown, N. C.-M. Bartlett, A. J. Alexander, R. N. Zare, and T. P. Rakitzis, “Optical control of ground-state atomic orbital alignment: $\mathrm{Cl}({}^2P_{3/2})$ atoms from $\mathrm{HCl}(\nu = 2, j = 1)$ photodissociation,” J. Chem. Phys. **127**, 144307 (2007).

[92] N. C.-M. Bartlett, D. J. Miller, R. N. Zare, A. J. Alexander, D. Sofikitis, and T. P. Rakitzis, “Time-dependent depolarization of aligned hd molecules,” Phys. Chem. Chem. Phys. **11**, 142–147 (2009).

[93] N. C.-M. Bartlett, J. Jankunas, R. N. Zare, and J. A. Harrison, “Time-dependent depolarization of aligned D_2 caused by hyperfine coupling,” Phys. Chem. Chem. Phys. **12**, 15689–15694 (2010).

[94] K. Grygoryeva, J. Rakovský, O. Votava, and M. Fárník, “Imaging of rotational wave-function in photodissociation of rovibrationally excited HCl molecules,” J. Chem. Phys. **147**, 013901 (2017).

[95] E. F. Thomas, A. A. Søndergaard, B. Shepperson, N. E. Henriksen, and H. Stapelfeldt, “Hyperfine-structure-induced depolarization of impulsively aligned I_2 molecules,” Phys. Rev. Lett. **120**, 163202 (2018), arXiv:1804.04416 [physics] .

[96] M. F. Colombo, D. C. Rau, and V. A. Parsegian, “Protein Solvation in Allosteric regulation: A Water Effect on Hemoglobin,” Science **256**, 655–659 (1992).

[97] H. Lami and N. Glasser, “Indole solvatochromism revisited,” J. Chem. Phys. **84**, 597–604 (1986).

[98] A. L. Sobolewski and W. Domcke, “Photoinduced charge separation in indole–water clusters,” Chem. Phys. Lett. **329**, 130–137 (2000).

[99] A. L. Sobolewski and W. Domcke, “Photoejection of electrons from pyrrole into an aqueous environment: ab initio results on pyrrole-water clusters,” Chem. Phys. Lett. **321**, 479–484 (2000).

[100] I. Frank and K. Damianos, “Excited state dynamics in pyrrole-water clusters: First principles simulation,” Chem. Phys. **343**, 347–352 (2008).

[101] H. Lippert, V. Stert, L. Hesse, C. P. Schulz, I. V. Hertel, and W. Radloff, “Ultrafast photoinduced processes in indole–water clusters,” Chem. Phys. Lett. **376**, 40–48 (2003).

[102] S. Trippel, Y.-P. Chang, S. Stern, T. Mullins, L. Holmegaard, and J. Küpper, “Spatial separation of state- and size-selected neutral clusters,” Phys. Rev. A **86**, 033202 (2012), arXiv:1208.4935 [physics] .

[103] S. Trippel, J. Wiese, T. Mullins, and J. Küpper, “Communication: Strong laser alignment of solvent-solute aggregates in the gas-phase,” J. Chem. Phys. **148**, 101103 (2018), arXiv:1801.08789 [physics] .

[104] M. Johny, J. Onvlee, T. Kierspel, H. Bieker, S. Trippel, and J. Küpper, “Spatial separation of pyrrole and pyrrole-water clusters,” Chem. Phys. Lett. **721**, 149–152 (2019), arXiv:1901.05267 [physics] .

[105] R. N. Zare, *Angular Momentum* (John Wiley & Sons, New York, NY, USA, 1988).

[106] W. Gordy and R. L. Cook, *Microwave Molecular Spectra*, 3rd ed. (John Wiley & Sons, New York, NY, USA, 1984).

[107] P. R. Bunker and P. Jensen, *Molecular Symmetry and Spectroscopy*, 2nd ed. (NRC Research Press, Ottawa, Ontario, Canada, 1998).

[108] H. W. Kroto, *Molecular Rotation Spectra* (Dover Publications, Inc., Mineola, NY, USA, 2003).

[109] S. C. Wang, “On the asymmetrical top in quantum mechanics,” Phys. Rev. **34**, 243 (1929).

[110] A. Yachmenev and S. N. Yurchenko, “Automatic differentiation method for numerical construction of the rotational-vibrational Hamiltonian as a power series in the curvilinear internal coordinates using the Eckart frame,” J. Chem. Phys. **143**, 014105 (2015).

[111] R. L. Cook and F. C. de Lucia, “Application of the theory of irreducible tensor operators to molecular hyperfine structure,” Am. J. Phys. **39**, 1433–1454 (1971).

[112] A. Yachmenev and J. Küpper, “Communication: General variational approach to nuclear-quadrupole coupling in rovibrational spectra of polyatomic molecules,” J. Chem. Phys. **147**, 141101 (2017), arXiv:1709.08558 [physics] .

[113] S. N. Yurchenko, A. Yachmenev, and R. I. Ovsyannikov, “Symmetry adapted ro-vibrational basis functions for variational nuclear motion calculations: TROVE approach,” J. Chem. Theory Comput. **13**, 4368 (2017), arXiv:1708.07185 [physics] .

[114] S. N. Yurchenko, W. Thiel, and P. Jensen, “Theoretical ROVibrational energies (TROVE): A robust numerical approach to the calculation of rovibrational energies for polyatomic molecules,” J. Mol. Spectrosc. **245**, 126–140 (2007).

[115] A. Owens and A. Yachmenev, “RichMol: A general variational approach for rovibrational molecular dynamics in external electric fields,” J. Chem. Phys. **148**, 124102 (2018), arXiv:1802.07603 [physics] .

[116] M. Feit, J. Fleck, and A. Steiger, "Solution of the Schrödinger equation by a spectral method," J. Comput. Phys. **47**, 412–433 (1982).

[117] J. Omiste-Romero, *Interaction of rotationally cold molecules with external fields*, Dissertation, Universidad de Granada, Granada, Spain (2013).

[118] C. Leforestier, R. H. Bisseling, C. Cerjan, M. D. Feit, R. Friesner, A. Guldberg, A. Hammerich, G. Jolicard, W. Karrlein, H.-D. Meyer, N. Lipkin, O. Roncero, and R. Kosloff, "A comparison of different propagation schemes for the time dependent Schrödinger equation," J. Comput. Phys. **94**, 59–80 (1991).

[119] M. Beck, A. Jäckle, G. Worth, and H.-D. Meyer, "The multiconfiguration time-dependent-Hartree (MCTDH) method: a highly efficient algorithm for propagating wavepackets," Phys. Rep. **324**, 1–105 (2000).

[120] J. J. Omiste, R. González-Férez, and P. Schmelcher, "Rotational spectrum of asymmetric top molecules in combined static and laser fields," J. Chem. Phys. **135**, 064310 (2011), arXiv:1106.1586 [physics] .

[121] F. Filsinger, J. Küpper, G. Meijer, L. Holmegaard, J. H. Nielsen, I. Nevo, J. L. Hansen, and H. Stapelfeldt, "Quantum-state selection, alignment, and orientation of large molecules using static electric and laser fields," J. Chem. Phys. **131**, 064309 (2009), arXiv:0903.5413 [physics] .

[122] J. J. Omiste and R. González-Férez, "Nonadiabatic effects in long-pulse mixed-field orientation of a linear polar molecule," Phys. Rev. A **86**, 043437 (2012).

[123] J. J. Omiste and R. González-Férez, "Rotational dynamics of an asymmetric-top molecule in parallel electric and nonresonant laser fields," Phys. Rev. A **88**, 033416 (2013).

[124] J. J. Omiste and R. González-Férez, "Theoretical description of mixed-field orientation of asymmetric top molecules: a time-dependent study," Phys. Rev. A **94**, 063408 (2016), arXiv:1610.01284 [physics] .

[125] B. Deppe, G. Huber, C. Kränkel, and J. Küpper, "High-intracavity-power thin-disk laser for alignment of molecules," Opt. Exp. **23**, 28491 (2015), arXiv:1508.03489 [physics] .

[126] S. Putzke, F. Filsinger, H. Haak, J. Küpper, and G. Meijer, "Rotational-state-specific guiding of large molecules," Phys. Chem. Chem. Phys. **13**, 18962 (2011), arXiv:1103.5080 [physics] .

[127] L. V. Thesing, J. Küpper, and R. González-Férez, "Time-dependent analysis of the mixed-field orientation of molecules without rotational symmetry," J. Chem. Phys. **146**, 244304 (2017), arXiv:1705.03225 [physics] .

[128] T. S. Zwier, "The spectroscopy of solvation in hydrogen-bonded aromatic clusters," Annu. Rev. Phys. Chem. **47**, 205–241 (1996).

[129] P. S. Cremer, A. H. Flood, B. C. Gibb, and D. L. Mobley, "Collaborative routes to clarifying the murky waters of aqueous supramolecular chemistry," Nat. Chem. **10**, 8–16 (2018).

[130] J. C. H. Spence and H. N. Chapman, "The birth of a new field," Phil. Trans. R. Soc. B **369**, 20130309–20130309 (2014).

[131] J. Yang, M. Guehr, X. Shen, R. Li, T. Vecchione, R. Coffee, J. Corbett, A. Fry, N. Hartmann, C. Hast, K. Hegazy, K. Jobe, I. Makasyuk, J. Robinson, M. S.

Robinson, S. Vetter, S. Weathersby, C. Yoneda, X. Wang, and M. Centurion, "Diffractive imaging of coherent nuclear motion in isolated molecules," Phys. Rev. Lett. **117**, 153002 (2016).

[132] K. L. Reid, "Accessing the molecular frame through strong-field alignment of distributions of gas phase molecules," Phil. Trans. R. Soc. A **376**, 20170158–10 (2018).

[133] S. Trippel, M. Johny, T. Kierspel, J. Onvlee, H. Bieker, H. Ye, T. Mullins, L. Gumprecht, K. Długołęcki, and J. Küpper, "Knife edge skimming for improved separation of molecular species by the deflector," Rev. Sci. Instrum. **89**, 096110 (2018), arXiv:1802.04053 [physics] .

[134] J. R. Carney, F. C. Hagemeister, and T. S. Zwier, "Hydrogen-bonding topologies of indole-(water)$_\mathrm{n}$ clusters from resonant ion-dip infrared spectroscopy," J. Chem. Phys. **108**, 3379–3382 (1998).

[135] M. Mons, I. Dimicoli, B. Tardivel, F. Piuzzi, V. Brenner, and P. Millié, "Site dependence of the binding energy of water to indole: Microscopic approach to the side chain hydration of tryptophan," J. Phys. Chem. A **103**, 9958–9965 (1999).

[136] G. O. Sørensen, "A new approach to the hamiltonian of nonrigid molecules," in *Large Amplitude Motion in Molecules II* (Springer Verlag, 1979) pp. 97–175.

[137] E. Mátyus, G. Czakó, and A. G. Császár, "Toward black-box-type full- and reduced-dimensional variational (ro)vibrational computations," J. Chem. Phys. **130**, 134112 (2009).

[138] T. H. Dunning, "Gaussian basis sets for use in correlated molecular calculations. I. The atoms boron through neon and hydrogen," J. Chem. Phys. **90**, 1007 (1989).

[139] R. A. Kendall, T. H. Dunning, Jr., and R. J. Harrison, "Electron affinities of the first-row atoms revisited. Systematic basis sets and wave functions," J. Chem. Phys. **96**, 6796–6806 (1992).

[140] F. Weigend, "A fully direct RI-HF algorithm: Implementation, optimised auxiliary basis sets, demonstration of accuracy and efficiency," Phys. Chem. Chem. Phys. **4**, 4285–4291 (2002).

[141] C. Hättig, "Optimization of auxiliary basis sets for RI-MP2 and RI-CC2 calculations: Core–valence and quintuple-ζ basis sets for H to Ar and QZVPP basis sets for Li to Kr," Phys. Chem. Chem. Phys. **7**, 59–66 (2005).

[142] R. M. Parrish, L. A. Burns, D. G. A. Smith, A. C. Simmonett, A. E. DePrince, E. G. Hohenstein, U. Bozkaya, A. Y. Sokolov, R. Di Remigio, R. M. Richard, J. F. Gonthier, A. M. James, H. R. McAlexander, A. Kumar, M. Saitow, X. Wang, B. P. Pritchard, P. Verma, H. F. Schaefer, K. Patkowski, R. A. King, E. F. Valeev, F. A. Evangelista, J. M. Turney, T. D. Crawford, and C. D. Sherrill, "Psi4 1.1: An open-source electronic structure program emphasizing automation, advanced libraries, and interoperability," J. Chem. Theory Comput. **13**, 3185–3197 (2017).

[143] B. Shepperson, A. A. Søndergaard, L. Christiansen, J. Kaczmarczyk, R. E. Zillich, M. Lemeshko, and H. Stapelfeldt, "Laser-induced rotation of iodine molecules in helium nanodroplets: Revivals and breaking free," Phys. Rev. Lett. **118**, 203203 (2017), arXiv:1702.01977 [physics] .

[144] C. P. Koch, M. Lemeshko, and D. Sugny, "Quantum control of molecular rotation," Rev. Mod. Phys. **91**, 035005 (2019).

[145] T. Kanai, S. Minemoto, and H. Sakai, "Quantum interference during high-order harmonic generation from aligned molecules," Nature **435**, 470–474 (2005).

[146] S. J. Weber, M. Oppermann, and J. P. Marangos, "Role of rotational wave packets in strong field experiments," Phys. Rev. Lett. **111**, 263601 (2013).

[147] E. W. Kuipers, M. G. Tenner, A. Kleyn, and S. Stolte, "Observation of steric effects in gas-surface scattering," Nature **334**, 420–422 (1988).

[148] V. Aquilanti, M. Bartolomei, F. Pirani, D. Cappelletti, F. Vecchiocattivi, Y. Shimizu, and T. Kasai, "Orienting and aligning molecules for stereochemistry and photodynamics," Phys. Chem. Chem. Phys. **7**, 291–300 (2005).

[149] P. M. Felker, J. S. Baskin, and A. H. Zewail, "Rephasing of collisionless molecular rotational coherence in large molecules," J. Phys. Chem. **90**, 724–728 (1986).

[150] M. Spanner, S. Patchkovskii, E. Frumker, and P. Corkum, "Mechanisms of two-color laser-induced field-free molecular orientation," Phys. Rev. Lett. **109**, 113001 (2012), arXiv:1205.4383 [physics] .

[151] K. Lin, I. Tutunnikov, J. Qiang, J. Ma, Q. Song, Q. Ji, W. Zhang, H. Li, F. Sun, X. Gong, H. Li, P. Lu, H. Zeng, Y. Prior, I. S. Averbukh, and J. Wu, "All-optical field-free three-dimensional orientation of asymmetric-top molecules," Nat. Commun. **9**, 5134 (2018), arXiv:1803.07823 [physics] .

[152] F. Rosca-Pruna and M. J. J. Vrakking, "Revival structures in picosecond laser-induced alignemnt of I_2 molecules. II. Numerical modeling," J. Chem. Phys. **116**, 6579 (2002).

[153] T. Seideman and E. Hamilton, "Nonadiabatic alignment by intense pulses. concepts, theory, and directions," Adv. Atom. Mol. Opt. Phys. **52**, 289–329 (2005).

[154] L. V. Thesing, A. Yachmenev, R. González-Férez, and J. Küpper, "Laser-induced alignment of weakly bound molecular aggregates," Phys. Rev. A **98**, 053412 (2018), arXiv:1808.01206 [physics] .

[155] B. Erk, R. Boll, S. Trippel, D. Anielski, L. Foucar, B. Rudek, S. W. Epp, R. Coffee, S. Carron, S. Schorb, K. R. Ferguson, M. Swiggers, J. D. Bozek, M. Simon, T. Marchenko, J. Küpper, I. Schlichting, J. Ullrich, C. Bostedt, D. Rolles, and A. Rudenko, "Imaging charge transfer in iodomethane upon x-ray photoabsorption," Science **345**, 288–291 (2014).

[156] K. Nass, L. Foucar, T. R. M. Barends, E. Hartmann, S. Botha, R. L. Shoeman, R. B. Doak, R. Alonso-Mori, A. Aquila, S. Bajt, A. Barty, R. Bean, K. R. Beyerlein, M. Bublitz, N. Drachmann, J. Gregersen, H. O. Jönsson, W. Kabsch, S. Kassemeyer, J. E. Koglin, M. Krumrey, D. Mattle, M. Messerschmidt, P. Nissen, L. Reinhard, O. Sitsel, D. Sokaras, G. J. Williams, S. Hau-Riege, N. Timneanu, C. Caleman, H. N. Chapman, S. Boutet, and I. Schlichting, "Indications of radiation damage in ferredoxin microcrystals using high-intensity X-FEL beams," J. Synchrotron Rad. **22**, 225–238 (2015).

[157] I. Nevo, L. Holmegaard, J. H. Nielsen, J. L. Hansen, H. Stapelfeldt, F. Filsinger, G. Meijer, and J. Küpper, "Laser-induced 3D alignment and orientation of quan-

tum state-selected molecules," Phys. Chem. Chem. Phys. **11**, 9912–9918 (2009), arXiv:0906.2971 [physics] .

[158] T. Takanashi, K. Nakamura, E. Kukk, K. Motomura, H. Fukuzawa, K. Nagaya, S. ichi Wada, Y. Kumagai, D. Iablonskyi, Y. Ito, Y. Sakakibara, D. You, T. Nishiyama, K. Asa, Y. Sato, T. Umemoto, K. Kariyazono, K. Ochiai, M. Kanno, K. Yamazaki, K. Kooser, C. Nicolas, C. Miron, T. Asavei, L. Neagu, M. Schöffler, G. Kastirke, X.-J. Liu, A. Rudenko, S. Owada, T. Katayama, T. Togashi, K. Tono, M. Yabashi, H. Kono, and K. Ueda, "Ultrafast coulomb explosion of a diiodomethane molecule induced by an x-ray free-electron laser pulse," Phys. Chem. Chem. Phys. **19**, 19707–19721 (2017).

[159] K. L. Chubb, A. Yachmenev, J. Tennyson, and S. N. Yurchenko, "Treating linear molecule HCCH in calculations of rotation-vibration spectra," J. Chem. Phys. **149**, 014101 (2018).

[160] P. Coles, A. Owens, J. Küpper, and A. Yachmenev, "Hyperfine-resolved rotation-vibration line list of ammonia (NH_3)," Astrophys. J. **870**, 24 (2018), arXiv:1809.06915 [physics] .

[161] S. Trippel, T. Mullins, N. L. M. Müller, J. S. Kienitz, J. J. Omiste, H. Stapelfeldt, R. González-Férez, and J. Küpper, "Strongly driven quantum pendulum of the carbonyl sulfide molecule," Phys. Rev. A **89**, 051401(R) (2014), arXiv:1401.6897 [quant-ph] .

[162] M. Torrent-Sucarrat, J. M. Luis, and B. Kirtman, "Variational calculation of vibrational linear and nonlinear optical properties," J. Chem. Phys. **122**, 204108 (2005).

[163] F. Weigend, F. Furche, and R. Ahlrichs, "Gaussian basis sets of quadruple zeta valence quality for atoms H–Kr," J. Chem. Phys. **119**, 12753–12762 (2003).

[164] F. Weigend and R. Ahlrichs, "Balanced basis sets of split valence, triple zeta valence and quadruple zeta valence quality for H to Rn: Design and assessment of accuracy," Phys. Chem. Chem. Phys. **7**, 3297 (2005).

[165] K. A. Peterson, D. Figgen, E. Goll, H. Stoll, and M. Dolg, "Systematically convergent basis sets with relativistic pseudopotentials. II. Small-core pseudopotentials and correlation consistent basis sets for the post-d group 16–18 elements," J. Chem. Phys. **119**, 11113–11123 (2003).

[166] D. Hait and M. Head-Gordon, "How accurate are static polarizability predictions from density functional theory? An assessment over 132 species at equilibrium geometry," Phys. Chem. Chem. Phys. **20**, 19800–19810 (2018).

[167] F. Neese, A. Wolf, T. Fleig, M. Reiher, and B. A. Hess, "Calculation of electric-field gradients based on higher-order generalized Douglas–Kroll transformations," J. Chem. Phys. **122**, 204107 (2005).

[168] F. E. Jorge, A. C. Neto, G. G. Camiletti, and S. F. Machado, "Contracted gaussian basis sets for Douglas–Kroll–Hess calculations: Estimating scalar relativistic effects of some atomic and molecular properties," J. Chem. Phys. **130**, 064108 (2009).

[169] C. Campos and F. Jorge, "Triple zeta quality basis sets for atoms Rb through Xe: application in CCSD(T) atomic and molecular property calculations," Mol. Phys. **111**, 167–173 (2012).

[170] R. Bjornsson and M. Bühl, “Electric field gradients of transition metal complexes: Basis set uncontraction and scalar relativistic effects,” Chem. Phys. Lett. **559**, 112–116 (2013).

[171] F. Neese, “The ORCA program system,” Wiley Interdiscip. Rev. Comput. Mol. Sci. **2**, 73–78 (2011).

[172] F. Neese, “Software update: the ORCA program system, version 4.0,” Wiley Interdiscip. Rev. Comput. Mol. Sci. **8**, e1327 (2017).

[173] P. Pyykkö, “Year-2008 nuclear quadrupole moments,” Mol. Phys. **106**, 1965–1974 (2008).

[174] M. D. Poulsen, E. Peronne, H. Stapelfeldt, C. Z. Bisgaard, S. Viftrup, E. Hamilton, and T. Seideman, “Nonadiabatic alignment of asymmetric top molecules: Rotational revivals,” J. Chem. Phys. **121**, 783–791 (2004).

[175] A. Yachmenev, L. V. Thesing, and J. Küpper, “Laser-induced dynamics of molecules with strong nuclear quadrupole coupling,” J. Chem. Phys. **151**, 244118 (2019), arXiv:1910.13275 [physics] .

[176] M. Kroll, “Hyperfine structure in the visible molecular-iodine absorption spectrum,” Phys. Rev. Lett. **23**, 631–633 (1969).

[177] N. R. Hutzler, H.-I. Lu, and J. M. Doyle, “The buffer gas beam: An intense, cold, and slow source for atoms and molecules,” Chem. Rev. **112**, 4803–4827 (2012), arXiv:1111.2841 [physics] .

[178] S. Y. T. van de Meerakker, H. L. Bethlem, N. Vanhaecke, and G. Meijer, “Manipulation and control of molecular beams,” Chem. Rev. **112**, 4828–4878 (2012).

[179] J. H. Nielsen, P. Simesen, C. Z. Bisgaard, H. Stapelfeldt, F. Filsinger, B. Friedrich, G. Meijer, and J. Küpper, “Stark-selected beam of ground-state OCS molecules characterized by revivals of impulsive alignment,” Phys. Chem. Chem. Phys. **13**, 18971–18975 (2011), arXiv:1105.2413 [physics] .

[180] D. A. Horke, Y.-P. Chang, K. Długołęcki, and J. Küpper, “Separating para and ortho water,” Angew. Chem. Int. Ed. **53**, 11965–11968 (2014), arXiv:1407.2056 [physics] .

[181] J. Ulmanis, J. Deiglmayr, M. Repp, R. Wester, and M. Weidemüller, “Ultracold molecules formed by photoassociation: Heteronuclear dimers, inelastic collisions, and interactions with ultrashort laser pulses,” Chem. Rev. **112**, 4890–4927 (2012).

[182] G. Quéméner and P. S. Julienne, “Ultracold molecules under control!” Chem. Rev. **112**, 4949–5011 (2012).

[183] A. Yokozeki and J. S. Muenter, “Laser fluorescence state selected and detected molecular beam magnetic resonance in I_2,” J. Chem. Phys. **72**, 3796–3804 (1980).

[184] G. Maroulis, C. Makris, U. Hohm, and D. Goebel, “Electrooptical properties and molecular polarization of iodine, I_2,” J. Phys. Chem. A **101**, 953–956 (1997).

[185] L. V. Thesing, A. Yachmenev, R. González-Férez, and J. Küpper, “The effect of nuclear-quadrupole coupling in the laser induced alignment of molecules,” J. Phys. Chem. A (2020), accepted, arXiv:1911.12270 [physics] .

[186] J. L. Neill, S. T. Shipman, L. Alvarez-Valtierra, A. Lesarri, Z. Kisiel, and B. H. Pate, “Rotational spectroscopy of iodobenzene and iodobenzene–neon with a direct

digital 2–8ghz chirped-pulse fourier transform microwave spectrometer," J. Mol. Spectrosc. **269**, 21 – 29 (2011).

[187] J. Karczmarek, J. Wright, P. Corkum, and M. Ivanov, "Optical centrifuge for molecules," Phys. Rev. Lett. **82**, 3420–3423 (1999).

[188] D. M. Villeneuve, S. A. Aseyev, P. Dietrich, M. Spanner, M. Y. Ivanov, and P. B. Corkum, "Forced molecular rotation in an optical centrifuge," Phys. Rev. Lett. **85**, 542 – 545 (2000).

[189] L. Yuan, S. W. Teitelbaum, A. Robinson, and A. S. Mullin, "Dynamics of molecules in extreme rotational states," Proc. Natl. Acad. Sci. U. S. A. **108**, 6872–6877 (2011).

[190] A. Korobenko, A. A. Milner, and V. Milner, "Direct observation, study, and control of molecular superrotors," Phys. Rev. Lett. **112**, 113004 (2014).

[191] A. Korobenko and V. Milner, "Adiabatic field-free alignment of asymmetric top molecules with an optical centrifuge," Phys. Rev. Lett. **116**, 183001 (2016).

[192] J. J. Omiste, "Theoretical study of asymmetric super-rotors: Alignment and orientation," Phys. Rev. A **97**, 023407 (2018).

[193] A. Owens, A. Yachmenev, and J. Küpper, "Coherent control of the rotation axis of molecular superrotors," J. Phys. Chem. Lett. **9**, 4206–4209 (2018), arXiv:1807.04016 [physics] .

Acknowledgements

I want to thank all the people who supported me in one way or another during my PhD project.

First of all, I want to express my deep gratitude towards my supervisor Jochen Küpper and my Co-supervisor Rosario González-Férez for giving me the opportunity to work at the Center for Free-Electron Laser Science in Hamburg and at the University of Granada. This very international environment made my time as a PhD student a truly inspiring experience. I learned a lot from both of them and I am thankful for their support, helpful advise and guidance throughout my research project.

I am very thankful to Jochen Küpper for the opportunity to work in the Controlled Molecule Imaging group at Center for Free-Electron Laser Science (CFEL), an amazing and diverse group of scientists. Jochen's critical analysis of my work always encouraged me to seek a deeper understanding in all my projects.

I am also grateful to Rosario González-Férez, for her amazing support and everything she taught me as well as the opportunity to work at the University of Granada for a large amount of the time.

I want to thank all past and present members of the Controlled Molecule Imaging group for making the last 4.5 years such a fun experience. In particular, I would like to thank Andrey Yachmenev, the CMI theory team leader, for our many scientific (and nonscientific) discussions and for always pushing me to learn new things. I am grateful to Evangelos Karamatskos for helpful discussions about alignment dynamics of molecules. Thank you to both Andrey and Evangelos for the comments on my thesis. Furthermore, I would like to thank Sebastian Trippel for our work together and Barbora Vagovič for her great support.

I would like to thank Steve Aplin, Adrian Pagel, Vitaliy Dodonov and Frank Schluenzen for their help in IT related topics including the hardware and software I needed and using the Maxwell cluster in Hamburg, where I performed most of the calculations presented in this thesis.

I would like to acknowledge financial support from DESY, the Center of Ultrafast Imaging and PIER, which allowed me to attend a number of interesting international conferences.

I want to thank my friends and family, especially my parents Karin and Ulrich Thesing for their support (financial and otherwise) throughout my whole education and for being great role models both as scientists and as people. They encouraged my interest in science from an early age. I also want to thank my siblings Eike and Gesa Thesing as well as my grandparents Inge Beckmann and Robert Thesing for their support.

Finally, I want to thank my boyfriend Pablo Martinez for supporting me in many ways throughout my PhD project. To him and his parents, I am grateful for making me feel at home in Granada and their help with all the administrative challenges related to living there.

Acronyms

CFEL	Center for Free-Electron Laser Science
LCLS	LINAC Coherent Light Source
MFF	molecule-fixed frame
MPA	most polarizable axis
OCS	carbonyl sulfide
TDSE	time-dependent Schrödinger equation
TISE	time-independent Schrödinger equation

List of Figures

List of Tables

List of publications

Publications related to this thesis

2020 *Non-adiabatic alignment of linear and asymmetric top molecules*
S. Trippel, T. Mullins, N. L. M. Müller, J. S. Kienitz, **L. V. Thesing**, R. González-Férez and J. Küpper
in preparation (2020)

2020 *Nuclear-quadrupole effects in the laser induced alignment of different molecular species*
L. V. Thesing, Andrey Yachmenev, R. González-Férez and J. Küpper
in preparation (2020)

2020 *The effect of nuclear-quadrupole coupling in the laser induced alignment of molecules*
L. V. Thesing, A. Yachmenev, R. González-Férez and J. Küpper,
J. Phys. Chem. A, accepted (2020), arXiv:1911.12270 [physics]

2019 *Laser-induced dynamics of molecules with strong nuclear quadrupole coupling*
A. Yachmenev, **L. V. Thesing** and J. Küpper
J. Chem. Phys. **151**, 244118 (2019), arXiv:1910.13275 [physics]

2018 *Laser-induced alignment of weakly bound molecular aggregates*
L. V. Thesing, A. Yachmenev, R. González-Férez and J. Küpper
Phys. Rev. A **98**, 053412 (2018), arXiv:1808.01206 [physics]

2017 *Time-dependent analysis of the mixed-field orientation of molecules without rotational symmetry*
L. V. Thesing, J. Küpper and R. González-Férez
J. Chem. Phys. **146**, 244304 (2017), arXiv:1705.03225 [physics.chem-ph]